UNIVERSITY OF CALIFORNIA
RIVERSIDE

Simple and Bounds-Preserving Discretizations of the Cahn-Hilliard-Navier-Stokes Equations

A Dissertation submitted in partial satisfaction
of the requirements for the degree of

Doctor of Philosophy

in

Computer Science

by

Jason Goulding

June 2024

Dissertation Committee:

Professor Tamar Shinar, Co-Chairperson
Professor Craig Schroeder, Co-Chairperson
Professor Christian Shelton
Professor Jiasi Chen

The Dissertation of Jason Goulding is approved:

Committee Co-Chairperson

Committee Co-Chairperson

University of California, Riverside

Acknowledgments

I am very grateful to my advisors, Professors Tamar Shinar and Craig Schroeder, who have patiently helped and guided me throughout my time as a graduate student.

I would like to acknowledge and thank Mehrnaz Ayazi for her help as a co-author with "Simplified conservative discretization of the Cahn-Hilliard-Navier-Stokes equations" (Chapter 2). I would like to acknowledge and thank Tamar Shinar and Craig Schroeder for their work as co-authors both on "Simplified conservative discretization of the Cahn-Hilliard-Navier-Stokes equations" (Chapter 2) and "Conservative, bounded, and nonlinear discretization of the Cahn-Hilliard-Navier-Stokes equations" (Chapter 3).

I would also like to thank Professor Christian Shelton and Professor Jiasi Chen for serving on my Dissertation Committee.

Finally, I would like to thank Professor Victor Zordan, for inspiring me to enter the Ph.D. program at UCR and being my first advisor.

ABSTRACT OF THE DISSERTATION

Simple and Bounds-Preserving Discretizations of the Cahn-Hilliard-Navier-Stokes Equations

by

Jason Goulding

Doctor of Philosophy, Graduate Program in Computer Science
University of California, Riverside, June 2024
Professor Tamar Shinar, Co-Chairperson
Professor Craig Schroeder, Co-Chairperson

When multiple fluids in a single system interact, they can mix and separate according to their physical properties. We can describe a two-fluid system of this kind using the phase-field model. This model uses a scalar field to represent the volume concentration or concentration difference of one of the fluids. By varying this field we can describe phase mixtures, and the interface between phases is represented by the field smoothly transitioning between extreme values. The Cahn-Hilliard equation is a fourth-order partial differential equation that can be used to describe the change in this phase-field through separation. This model acts to minimize an energy potential function with minima where the mixture is fully separated. We couple the Cahn-Hilliard equation to the classic Navier-Stokes equations to include fluid flow. We develop two novel discretization methods for this system.

The first method is a simplified time integration scheme based on splitting the fourth-order equation into a pair of second-order Helmholtz equations that can be solved as a pair of linear systems. We propose a method of coupling this discretization to an incom-

pressible Navier-Stokes equation that maintains consistency between mass and momentum. We also propose a novel surface tension force discretization that limits surface forces to the interface region. This surface tension can be controlled with a parameter that allows for transitioning between a sharp interface formulation and a smooth continuum surface force. A drawback of this scheme is that it relies on a mass redistribution post-processing step to maintain the phase variable in the physical bounds.

The second method is developed to intrinsically maintain the phase variable inside a physically consistent range instead of requiring a post-processing step. We formulate a piecewise energy potential function with energy barriers at both extremes. We combine this with a nonlinear second-order solve that is implicit in the energy potential. We show how to formulate this nonlinear equation as an optimization problem to be solved with a damped Newton's method. We compare both methods to previous work using a variety of experiments, and demonstrate that they are second-order accurate.

Contents

List of Figures **ix**

List of Tables **xii**

1 Introduction **1**
1.1 Cahn-Hilliard . . . 2
1.2 Solving the equation . . . 4
1.3 Maintaining phase-field bounds . . . 6
1.4 Cahn-Hilliard-Navier-Stokes equations . . . 6

2 Simplified conservative discretization of the Cahn-Hilliard-Navier-Stokes equations **9**
2.1 Introduction . . . 10
2.2 Governing equations . . . 14
2.2.1 Cahn-Hilliard Equation . . . 14
2.2.2 Navier-Stokes equations . . . 15
2.3 Discretizations . . . 15
2.3.1 Cahn-Hilliard equation . . . 16
2.3.2 Navier-Stokes equations . . . 20
2.3.3 Spatial Discretization . . . 28
2.3.4 Discretization summary . . . 32
2.4 Numerical examples . . . 36
2.4.1 Manufactured solution . . . 36
2.4.2 Binary separation of phases . . . 39
2.4.3 Stationary circle . . . 39
2.4.4 Horizontal shear . . . 41
2.4.5 Translating circle . . . 46
2.4.6 Rising air bubble . . . 47
2.4.7 Comparisons of surface tension . . . 52
2.4.8 Rayleigh-Taylor instability . . . 58
2.4.9 Dam break . . . 60
2.5 Conclusion . . . 63

2.6 Acknowledgements 66

3 Conservative, bounded, and nonlinear discretization of the Cahn-Hilliard-Navier-Stokes equations 67

3.1 Introduction 68
3.2 Governing equations 72
3.2.1 Cahn-Hilliard equation 72
3.2.2 Navier-Stokes equations 73
3.3 Discretizations 74
3.3.1 Cahn-Hilliard equation 74
3.3.2 Navier-Stokes equations 90
3.3.3 Discretization summary 93
3.4 Numerical examples 97
3.4.1 Manufactured solution 97
3.4.2 Binary separation of phases 102
3.4.3 Stationary circle 103
3.4.4 Horizontal shear 106
3.4.5 Translating circle 110
3.4.6 Rising air bubble 112
3.4.7 Rayleigh-Taylor instability 116
3.4.8 Dam break 118
3.5 Conclusion 122
3.6 Acknowledgements 125

4 Conclusions 126

List of Figures

1.1 A plot of $F(\gamma) = \frac{1}{\eta^2}\gamma^2(1-\gamma)^2$ used in Chapter 2. 3
1.2 A plot of $F'(\gamma) = \frac{1}{\eta^2}(4\gamma^3 - 6\gamma^2 + 2\gamma)$ used in Chapter 2. 4

2.1 $g(\gamma)$ vs γ for different values of a 24
2.2 Example path $\gamma_0 \to \gamma_N$. The triangles represent the pressure jumps along this path. 25
2.3 The MAC grid stores velocties on faces (represented by triangles), and γ and pressure on cell centers (circles). 28
2.4 The components of the momentum flux for updating the x component of momentum in 2D are shown in 2.4a. The momentum at the red triangle will be updated with the fluxes at the surrounding blue and orange dots. The u and $\mathbf{m}^x$ values at these dots are interpolated from neighboring values as illustrated in 2.4b and 2.4c, respectively. 29
2.5 Binary fluid separation over time 39
2.6 L_2 and L_∞ errors of velocity in the stationary circle test. 41
2.7 Horizontal Shear (Case 3). 42
2.8 Results of the horizontal shear test for Cases 1-4. 43
2.9 Artifacts in horizontal shear Case 1, and the effects of different parameters and methods on those artifacts. 45
2.10 Initial and final ($t = 1$) state of the drop with $\sigma = 10^{-12}$. The solid black line is the initial state and the dotted red line is the final state. 48
2.11 Initial and final ($t = 1$) state of the drop with $\sigma = 1$. The solid black line is the initial state and the dotted red line is the final state. 49
2.12 Rising bubble test results with $X_\eta = 0, X_M = 1$. 52
2.13 Rising bubble test results of test described in table 2.8 with $N = 256$. . . . 53
2.14 Comparisons of the angle between surface tension force and surface normal (radians) for different surface tension formulations. 55
2.15 Comparisons of the magnitude of surface tension force for different surface tension formulations. 56
2.16 Change in pressure in the x axis at $y = 0.5$ of Section 2.4.7. 57

2.17 Rayleigh-Taylor test at times $t = 0, 1, 1.25, 1.5, 1.75, 2, 2.25, 2.5$ and density ratio of 3. 59
2.18 Rayleigh-Taylor test results with $\rho_0 = 3$, from $t = 2.25$ to $t = 8$ in 0.25 increments. 60
2.19 Rayleigh-Taylor simulation with density ratio of 30, 1000 and 3000 at times $t = 0, 0.25, 0.5, 0.75, 1, 1.25, 1.5, 1.75$. 61
2.20 Location of the maximum and minimum x of the interface in the Rayleigh-Taylor test with density ratio of 3. 62
2.21 Fluid height and front over time in the dam break test. 63
2.22 The evolution of the dam break test with water and air from $T = 0$ to $T = 5$ in 0.5 increments. 64
2.23 The evolution of the dam break test with water and air from $T = 5$ to $T = 9.5$ in 0.5 increments. 65

3.1 The MAC grid stores γ and pressure on cell centers (circles). Velocties are stored by component on faces (represented by triangles), (Reproduced from [33].) 74
3.2 Plots of $F(C)$ (left) and $F'(C)$ (right) corresponding to $q = 0.5$ and $r = 0.1$. 81
3.3 Plot of $F(C)$ for different values of r: 0.1 (—), 0.05 (—), 0.02 (—), 0.01 (—), and 0.001 (—). The potential function converges pointwise in the limit $r \to 0$ over the range $0 < C < 1$. 81
3.4 Plot of $g'(C)$ for different values of q: 0.99 (—), 0.9 (—), 0.5 (—), 0.001 (—). The function g' converges to piecewise-linear in the limit $q \to 0$ and develops an infinite slope at $C = \frac{1}{2}$ in the limit $q \to 1$. When $q > 1$, (3.26), when viewed as a function $C(\gamma)$, is not monotonic. In this case, g' would become multivalued. Useful values of q are thus restricted to $0 < q < 1$ to ensure that (3.26) has a unique and continuous solution. 84
3.5 Plots of $g(C)$ (left) and $g''(C)$ (right) corresponding to $q = 0.5$ and $r = 0.1$. 85
3.6 Snapshots of phase separation over time. 103
3.7 The magnitude of the spurious velocity for the five stationary circle cases at different resolutions. 105
3.8 The magnitude of the spurious velocity for the five stationary circle cases with fixed interface width. 106
3.9 Example of Horizontal Shear (Case 3). 108
3.10 Conservation results for the four horizontal shear cases. 109
3.11 The initial state of the translating circle (Cases 1–4) is represented by the solid black line. The final ($t = 1$) state is represented by the dashed red line. The blue dashed arrows represent the velocity streamlines at $t = 1$. 112
3.12 The initial state of the translating circle (Cases 5–8) is represented by the solid black line. The final ($t = 1$) state is represented by the dashed red line. The blue dashed arrows represent the velocity streamlines at $t = 1$. 113
3.13 Results for rising air bubble case 1. 116
3.14 Comparing results for all rising bubble test cases with $N = 256$. 117
3.15 Visual comparison of Rayleigh-Taylor simulations using different methods at $t = 0, 1, 1.25, 1.5, 1.75, 2, 2.25, 2.5$. 119

3.16 Continued snapshots of a Rayleigh-Taylor simulation using our method with $\rho_0 = 3$, from $t = 2.25$ to $t = 8$ in 0.25 increments. 120
3.17 Snapshots of Rayleigh-Taylor simulations with different density ratios at $t = 0, 0.25, 0.5, 0.75, 1, 1.25, 1.5, 1.75$. 121
3.18 Tracking the maximum and minimum y of the phase interface in the Rayleigh-Taylor simulation with $\rho_1/\rho_0 = 3$. 122
3.19 Tracking the height and front of fluid phase 1 in the dam break scenario. . . 122
3.20 Snapshots of the dam break scenario from $T = 0$ to $T = 4.5$. 123
3.21 Snapshots of the dam break scenario from $T = 5$ to $T = 9.5$. 124

List of Tables

2.1 Analysis of our Cahn-Hilliard solver at $t = 1$ demonstrates second order convergence. 37
2.2 Analysis of our Cahn-Hilliard-Navier-Stokes solver at $t = 1$ demonstrates second order convergence. 38
2.3 Material settings for different cases of the stationary circle test. 41
2.4 Material settings for different cases of the horizontal shear. 43
2.5 Material settings for different cases of the translating circle test (surface tension, density). 46
2.6 Error results for the advection test without surface tension. 47
2.7 Error results for the advection test with surface tension. 47
2.8 L_2 error and order compared to $N = 256$ on all the cases for rising air bubble test. 51
2.9 Material settings for different cases for the surface tension and pressure comparison test. 54

3.1 At larger N, our Cahn-Hilliard scheme shows second order convergence at $t = 1$. 98
3.2 The coupled Cahn-Hilliard-Navier-Stokes scheme shows second order convergence at $t = 1$. 99
3.3 L_2 and L_∞ errors in γ for varying values of q. 100
3.4 Analysis of manufactured solution error dependence on values of r. 102
3.5 Material parameters for the five tested stationary circle cases. 105
3.6 Material parameters for the four tested horizontal shear cases. 107
3.7 Material parameters for the eight translating circle cases. 110
3.8 Velocity error for the four translating circle cases without surface tension (1–4). 111
3.9 Velocity error for the four translating circle cases with surface tension (5–8). 111
3.10 Rising air bubble test convergence results, using a comparison of simulations with $N = 16$ through $N = 128$ to corresponding simulations with $N = 256$. 115

Chapter 1

Introduction

When multiple fluids in a single system interact, they can mix and separate according to their physical properties. Simulating these interactions is an area of study related to computer graphics. Many real physical phenomena involve multiple fluids interacting, such as air bubbles in water, oceanic oil spills, or fluid mixtures that separate over time. We can call these systems involving the flow of multiple fluids multiphase flows. Each fluid material is a single phase of the entire fluid flow system, and we will treat the bulk (combined) fluid evolution and fluid phase concentration evolution separately. We can describe a system of two fluid phases with a phase-field model. This type of model uses a scalar field to represent the concentration difference or volume fraction of one of the two phases. By varying this field, we can describe varying levels of phase mixtures, from purely separate phases to complete mixtures. In this work, we will use the phase variable $\gamma \in [0, 1]$ as the volume fraction of phase 1. When $\gamma = 1$ we have a region that is entirely fluid phase 1, and $\gamma = 0$ will indicate an area that is entirely phase 0. The interface between the two phases

can be inferred by finding a region where the phase field smoothly transitions from $\gamma \approx 1$ to $\gamma \approx 0$.

1.1 Cahn-Hilliard

John W. Cahn and John E. Hilliard [13] introduced a fourth-order partial differential equation as one model to describe the separation of phases, now known as the Cahn-Hilliard equation

$$\frac{\partial \gamma}{\partial t} = \nabla \cdot \left(M \nabla \lambda (F'(\gamma) - \nabla^2 \gamma) \right) + S_\gamma. \tag{1.1}$$

A mixture of fluids can separate due to chemical forces caused by the fluid properties. In Equation (1.1), the expression $\lambda(F'(\gamma) - \nabla^2\gamma)$, which can be denoted ξ, is often called the chemical potential. Choice of the potential function $F(\gamma)$, mobility parameter M, and interface parameter λ controls how the phases are driven to separate. Mobility M represents how strongly the chemical forces act on the fluid. $\lambda = \frac{3}{2\sqrt{2}}\sigma\eta$ is a constant that depends on the properties of the two phases and is calculated from the interface width η and the coefficient of surface tension σ for the fluid phases. The potential function $F(\gamma)$ defines the rest configuration of the phases and the energy landscape of the mixture. This function will be a double-well function where the minima are the locations where the phase-field variable is considered unmixed. Figure 1.1 shows a typical double-well function with minima at 1 and 0, but other variants exist and are used in this work. The derivative $F'(\gamma)$ (Figure 1.2) is used in the Cahn-Hilliard equation to act as a force driving the fluids to separate. This force is 0 at the minima of $F(\gamma)$, providing stable equilibrium points. There is also an

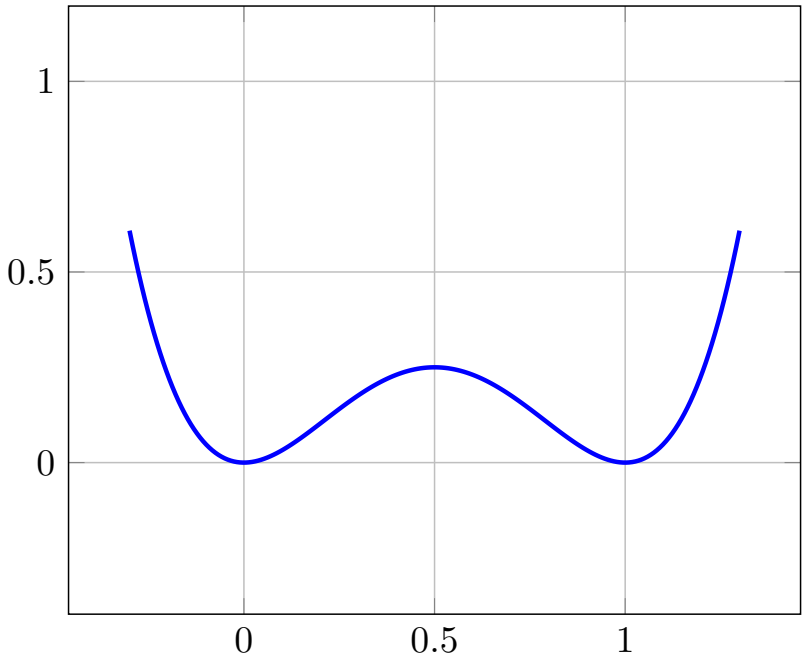

Figure 1.1: A plot of $F(\gamma) = \frac{1}{\eta^2}\gamma^2(1-\gamma)^2$ used in Chapter 2.

unstable equilibrium point at the center of $F(\gamma)$ where the force function $F'(\gamma) = 0$ but the potential energy is nonzero and $F''(\gamma)$ is negative. This point is where the phases are perfectly mixed, but even a small perturbation will cause the phases to no longer be in equilibrium and begin to separate. Finally, S_γ is a source term that can represent any external source of phase concentration.

If the bulk fluid has nonzero velocity $\mathbf{u}$, then we represent the effects of that flow on the phase concentration by adding an advection term to the equation:

$$\frac{\partial \gamma}{\partial t} + \nabla \cdot (\mathbf{u}\gamma) = \nabla \cdot \left(M \nabla \lambda (F'(\gamma) - \nabla^2 \gamma)\right) + S_\gamma. \tag{1.2}$$

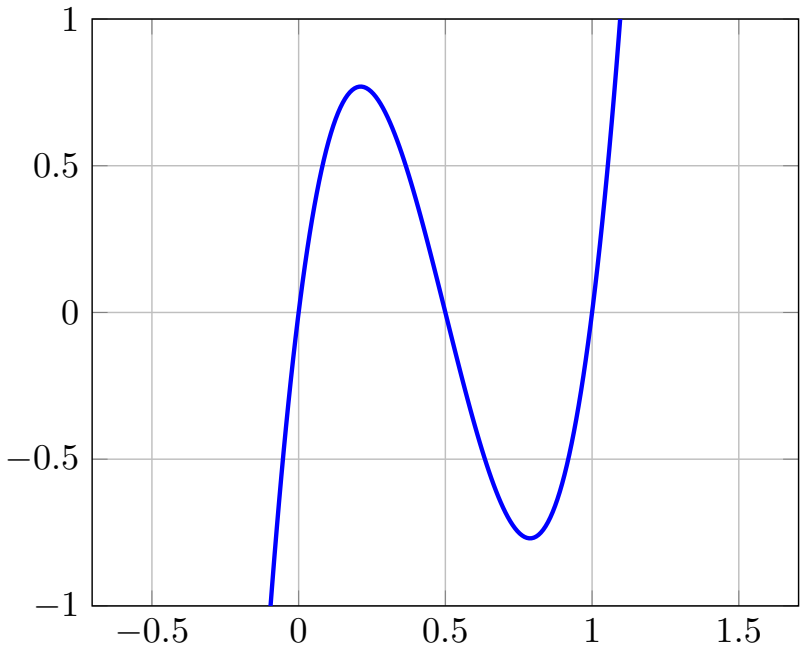

Figure 1.2: A plot of $F'(\gamma) = \frac{1}{\eta^2}(4\gamma^3 - 6\gamma^2 + 2\gamma)$ used in Chapter 2.

1.2 Solving the equation

The Cahn-Hilliard equation has a fourth-order spatial derivative, which can be difficult to solve, and there are different strategies that can be used to find the solution. In past work, this equation has been solved using Fourier transforms [43], which can turn the partial differential equation into a solvable ordinary differential equation. The method that we use in this work involves splitting the fourth-order equation into a pair of second order equations. This approach has been done before for Cahn-Hilliard [84, 73, 24, 47]. An example of splitting a general fourth order equation is shown here:

$$f + a^2\nabla^2\nabla^2 f = g. \tag{1.3}$$

This example equation is spatially fourth-order, and we will use a method that is similar to completing the square to split it into two second-order equations. We begin by adding the difference of Laplacians $2a\nabla^2(f - \hat{f})$, where $\hat{f}$ is an explicit approximation of f. This difference is nearly 0 if $\hat{f}$ is a good approximation, but it will in general introduce a small amount of error into our split:

$$f - 2a\nabla^2 f + a^2\nabla^2\nabla^2 f = g - 2a\nabla^2\hat{f}. \tag{1.4}$$

With these added Laplacians, we can now factor the left-hand side of the equation into a pair of second-order operators on f:

$$(1 - a\nabla^2)(1 - a\nabla^2)f = g - 2a\nabla^2\hat{f}. \tag{1.5}$$

By defining terms $f^* = (1 - a\nabla^2)f$ and $x = g - 2a\nabla^2\hat{f}$, the split becomes more apparent as

$$(1 - a\nabla^2)f^* = x \qquad \text{or} \qquad f^* - a\nabla^2 f^* = x \tag{1.6}$$

$$(1 - a\nabla^2)f = f^* \qquad \text{or} \qquad f - a\nabla^2 f = f^*. \tag{1.7}$$

These split equations are now a pair of second-order Helmholtz equations that we formulate as systems of linear equations and successively solve. In this work we will present two novel discretizations following this general example.

1.3 Maintaining phase-field bounds

While the Cahn-Hilliard equation does drive the system toward phase-field solutions for γ that are within the physically meaningful range $[0, 1]$, numerical methods can often fail to perfectly maintain γ in this range. This leads to numerical difficulties and physically invalid solutions. Even a small deviation from this range can results in negative effective fluid densities, especially when simulating mixtures with large phase density ratios. The first scheme in this dissertation (Chapter 2) uses a global post-processing scheme from [46] to address this issue. The second scheme (Chapter 3) instead uses a novel splitting and discretization of the Cahn-Hilliard equation that inherently maintains $\gamma \in [0, 1]$ and does not require a post-processing step.

1.4 Cahn-Hilliard-Navier-Stokes equations

To include the flow and dynamics of the bulk fluid with the individual phase evolution, we couple the Cahn-Hilliard equation to the Navier-Stokes equations. The Navier-Stokes equations are a set of equations for describing the flow of incompressible fluid in a conservative manner:

$$\frac{\partial \rho}{\partial t} + \nabla \cdot \mathbf{m} = S_m \tag{1.8}$$

$$\nabla \cdot \mathbf{u} = 0 \tag{1.9}$$

$$\frac{\partial(\rho \mathbf{u})}{\partial t} + \nabla \cdot (\mathbf{m} \otimes \mathbf{u}) = -\nabla p + \nabla \cdot (\mu(\nabla \mathbf{u} + (\nabla \mathbf{u})^T)) + \rho g + \sigma \kappa \nabla(h(\gamma)) + S_{\mathbf{u}}. \tag{1.10}$$

Equation (1.8) describes the conservation of mass. The density flux term $\mathbf{m}$ is defined from the evolution of the phase-field, and it is the first way that the Cahn-Hilliard equation will be coupled to the Navier-Stokes equations. It is important that $\mathbf{m}$ is defined in a way that is consistent with the evolution of the phase-field in order to ensure that momentum is conserved in the bulk fluid flow [47]. The second term that couples the equations is the surface tension term, an example of which can be found in Equation (1.10) as $\sigma\kappa\nabla(h(\gamma))$. Because the interface between fluid phases is determined by γ, the interface curvature and resulting surface force should also be determined using the same term. The surface tension influences the bulk flow which in turn affects the phase concentration evolution. The effective density ρ and viscosity μ also depend on the phase concentration and act as further coupling of the equations.

Chapter 2 introduces a simplified and conservative discretization of the coupled Cahn-Hilliard-Navier-Stokes equations. It also introduces a novel surface tension force discretization using the phase-field variable γ. This introduced surface tension force has finite influence around the interface and has a parameter that allows it to transition from a smoothed continuum surface force model to a fully sharp interface model. This method is compared to previous work with a variety of examples, and we demonstrate second-order accuracy.

Chapter 3 introduces a novel splitting and discretization for the Cahn-Hilliard equation which preserves the bounds $\gamma \in [0, 1]$. This method uses a second-order Helmholtz equation and a second-order nonlinear equation with implicit energy barriers. The energy barriers are introduced in a piecewise formulation for the potential function F at 0 and

1, and the corresponding derivative F' is solved implicitly in the nonlinear equation. The Helmholtz equation is solved as usual, and the nonlinear portion is solved by formulating it as the minimization of an objective function for use in an optimization-based solution method. We demonstrate second-order accuracy of this method, and compare it to the method in Chapter 2 as well as to previous work.

Chapter 2

Simplified conservative discretization of the Cahn-Hilliard-Navier-Stokes equations

In this chapter we construct a novel discretization of the Cahn-Hilliard equation coupled with the Navier-Stokes equations. The Cahn-Hilliard equation models the separation of a binary mixture. We construct a very simple time integration scheme for simulating the Cahn-Hilliard equation, which is based on splitting the fourth-order equation into two second-order Helmholtz equations. We combine the Cahn-Hilliard equation with the Navier-Stokes equations to simulate phase separation in a two-phase fluid flow in two dimensions. The scheme conserves mass and momentum and exhibits consistency between mass and

momentum, allowing it to be used with large density ratios. We introduce a novel discretization of the surface tension force from the phase-field variable that has finite support around the transition region. The model has a parameter that allows it to transition from a smoothed continuum surface force to a fully sharp interface formulation. We show that our method achieves second-order accuracy, and we compare our method to previous work in a variety of experiments.

2.1 Introduction

Phase-field models have been widely used to study many problems involving multiphase incompressible flows, including two-phase flows in a microtube [42], viscoelastic flows [84, 85], multiphase flows with soluble surfactants [64, 76, 87], phase separation and coarsening [88, 4], jet pinch-off [83, 55], multicomponent systems with three or more phases [56, 53, 81], tumor growth [80], microfluidics [71], and other physical phenomena. In these methods, the phase field represents the concentration of one of the components of the mixture, and fluid interfaces are represented by a smooth transition region between bulk regions of the different phases. One popular choice for the governing equation for the evolution of the phase field is the Cahn-Hilliard equation, which acts to minimize the free energy of the system, leading the mixture to segregate into separate regions [13, 25].

Many methods have been developed for the numerical simulation of the Cahn-Hilliard equation, including Fourier spectral methods [88, 43, 58], finite difference methods [32, 60, 38, 15, 47], and finite element methods [26, 10, 8, 29, 79, 41]. For example, Zhu et al. [88] examines properties of coarsening using a Fourier spectral solver, and He et al.

[43] developed a Fourier spectral solve which allows for large time steps. Schemes supporting adaptive time step sizes were presented in Li et al. [61] and the second-order accurate Guillén-González and Tierra [37]. Guillén-González and Tierra [36] presented two linear schemes derived through special treatment of the double-well potential function. Lee et al. [58] gives an overview of the mathematical derivation of the Cahn-Hilliard equation, discusses several methods for its numerical solution, and provides a Matlab implementation for a pseudospectral method.

A model of immiscible two-phase flows coupling the Cahn-Hilliard equation to the incompressible Navier-Stokes equations for the case of matching densities was described in Hohenberg and Halperin [44]; a derivation from first principles was given in Gurtin et al. [39]. Badalassi et al. [5] devised numerical simulations of this coupled system. For varying densities, some studies have used the Boussinesq approximation where the momentum equation is solved using a background density and the variable density appears only in additional buoyancy terms [49, 63, 4]. The more general case of the Cahn-Hilliard-Navier-Stokes (CHNS) equations with different densities and viscosities presents additional challenges, and Shen and Yang [74] devised a model which admits an energy law and developed an associated projection-type [17] numerical scheme. Shen and Yang [72] developed an unconditionally energy-stable numerical scheme which reduces the problem to the solution of a sequence of decoupled elliptic solves. Phase-field models of two-phase incompressible flow with large density ratios were simulated in Kim [52] and Ding et al. [21], which involved the solution of time-dependent variable coefficient linear systems. Dong and Shen [24] devised a scheme for large density and viscosity differences with improved efficiency through the use of constant

coefficient matrices. Yue et al. [84] coupled the Cahn-Hilliard equation to non-Newtonian flows. Guo et al. [38] devised a quasi-incompressible scheme with mass conservative and energy stability for the CHNS equations. Kim [55] provides a review of phase-field models and numerical methods for their approximation.

Consistency of mass and momentum transport was first addressed on the discrete level for two-phase interfacial flows in volume-tracking methods [12, 68] and the level set method [69]. For the coupled Cahn-Hilliard-Navier-Stokes equations, Huang et al. [47] formulated a set of consistency conditions in the continuous setting and furthermore devised a second-order accurate finite difference scheme with numerical consistency of mass and momentum flux. Huang et al. [46] similarly addressed consistency of mass and momentum transport in the Allen-Cahn equation and also devised a conservative redistribution scheme to maintain the physical bounds of the concentration.

In this chapter, we construct a novel conservative, second order accurate finite difference scheme for the simulation of the Cahn-Hilliard-Navier-Stokes equations for two phase flows with large density and viscosity differences. Following Huang et al. [47], we enforce discrete consistency of the mass and momentum fluxes. In contrast to Huang et al. [47], which used collocated grids for pressure, concentration, and velocity, our method uses a staggered MAC grid [40] to conveniently solve the pressure Poisson equation. We construct a very simple time integration scheme for simulating the Cahn-Hilliard equation, which is based on splitting the fourth-order equation into two second-order Helmholtz equations. Our splitting results in the solution of two Helmholtz equations with identical coefficient matrices. In our splitting, we use a stabilizing term introduced in Shen and Yang [72, 74].

The Cahn-Hilliard equation is coupled to the Navier-Stokes equations in part through the surface tension force, which depends on the gradient of the concentration phase field and the geometric curvature of the interface. Kim [52, 55] and Acar [2] discuss several models of surface tension for phase-field multiphase flows. The numerical simulation of surface tension can be challenging due to stability and accuracy issues including the formation of spurious currents about the interface. One common treatment of surface tension is the Continuum Surface Force (CSF) approach introduced in Brackbill et al. [11], where typically a discrete approximation to a smoothed delta function is used to spread the surface tension force over a small number of grid cells about the interface. Kim [54] used a continuum surface force combinations for more than two fluid phases. Another set of approaches treats the interface in a sharp manner, capturing the pressure jumps across the interface that balance the surface tension force [51]. Francois et al. [30] enforced exact force balance at the interface for both CSF and sharp interface schemes, eliminating one of the sources of spurious currents at the interface. In this chapter, we propose a novel discretization of surface tension that gives exact force balance at the interface and unifies the CSF and sharp interfaces schemes. A similar relationship between the CSF approach and the sharp interface approach was noted by Lalanne et al. [57] for level set methods. Our method is based on taking the gradient of a smoothed Heaviside approximation, similar to CSF approaches. Notably, the degree of smoothing is controlled by a parameter and the sharp interface method is directly recovered as the smoothing is decreased.

2.2 Governing equations

2.2.1 Cahn-Hilliard Equation

The Cahn-Hilliard equation, initially proposed by Cahn and Hilliard [13] and widely utilized to describe the phase separation process in a mixture of two fluids, is expressed as follows:

$$\frac{\partial \gamma}{\partial t} + \nabla \cdot (\mathbf{u}\gamma) = \nabla \cdot (M \nabla \xi) + S_\gamma \tag{2.1}$$

$$\xi = \lambda(F'(\gamma) - \nabla^2 \gamma) \tag{2.2}$$

$$F(\gamma) = \frac{1}{\eta^2}\gamma^2(1-\gamma)^2 \tag{2.3}$$

$$\lambda = \frac{3}{2\sqrt{2}}\sigma\eta. \tag{2.4}$$

The phase-field function $\gamma \in [0, 1]$ is the volume fraction of fluid phase 1 (with density ρ_1 and viscosity μ_1). $1 - \gamma$ is the volume fraction of fluid phase 0 (with density ρ_0 and viscosity μ_0). $\mathbf{u}$ is the velocity, M is the mobility, ξ is the chemical potential, S_γ is the source term for γ, λ is the mixing energy density, F is the double well potential function, F' is the derivative of F with respect to γ, η characterizes the thickness of the transition region between the two phases, and σ is the surface tension coefficient. The effective density and viscosity at a certain location is given by

$$\rho = \rho_0 + (\rho_1 - \rho_0)\,\gamma \tag{2.5}$$

$$\mu = \mu_0 + (\mu_1 - \mu_0)\,\gamma. \tag{2.6}$$

2.2.2 Navier-Stokes equations

The incompressible Navier-Stokes equations are given by

$$\frac{\partial \rho}{\partial t} + \nabla \cdot \mathbf{m} = S_m \tag{2.7}$$

$$\nabla \cdot \mathbf{u} = 0 \tag{2.8}$$

$$\frac{\partial(\rho \mathbf{u})}{\partial t} + \nabla \cdot (\mathbf{m} \otimes \mathbf{u}) = -\nabla p + \nabla \cdot (\mu(\nabla \mathbf{u} + (\nabla \mathbf{u})^T)) + \rho g + \sigma \kappa \nabla(g(\gamma)) + S_{\mathbf{u}}. \tag{2.9}$$

σ, ρ, and $\mathbf{u}$ are as defined in Section 2.2.1, $\mathbf{m}$ is the mass flux, S_m represents an external source of mass, $\sigma\kappa\nabla(g(\gamma))$ is the surface tension force, κ is the estimated interface curvature, $g(\gamma)$ is a regularized Heaviside function (see Section 2.3.2), p is the pressure, $\mathbf{g}$ is gravity, and S_u is the source term for momentum. Similar to [47], the mass flux $\mathbf{m}$ can be inferred from the γ evolution equation (2.1) and equations (2.7) and (2.5). Defining $S_m = (\rho_1 - \rho_0) S_\gamma$, it can be shown that a consistent definition of $\mathbf{m}$ is $\mathbf{m} = \rho\mathbf{u} - (\rho_1 - \rho_0) M \nabla \xi$. This is discussed in detail in Section 2.3.2.

2.3 Discretizations

In this section we describe the temporal and spatial discretizations of the Cahn-Hilliard and Navier-Stokes equations.

2.3.1 Cahn-Hilliard equation

Cahn-Hilliard equation temporal discretization

We begin by combining (2.1) and (2.2) as the base Cahn-Hilliard equation to discretize.

$$\frac{\partial \gamma}{\partial t} + \nabla \cdot (\mathbf{u}\gamma) = M\lambda\nabla^2(F'(\gamma) - \nabla^2\gamma) + S_\gamma \tag{2.10}$$

We discretize the time derivative as $\frac{\alpha\hat{\gamma}^{n+1} - \alpha\gamma^{BD}}{\Delta t}$. To achieve second-order accuracy, we use a backwards-difference scheme with $\alpha = \frac{3}{2}$ and $\gamma^{BD} = \frac{4}{3}\gamma^n - \frac{1}{3}\gamma^{n-1}$. For the first time step we use a first-order single-step scheme with $\alpha = 1$ and $\gamma^{BD} = \gamma^n$. Explicit quantities for $\mathbf{u}$ and γ are discretized using an Adams-Bashforth scheme, where $\gamma^{AB} = \gamma^n$, $\mathbf{u}^{AB} = \mathbf{u}^n$ in the first order case and $\gamma^{AB} = 2\gamma^n - \gamma^{n-1}$, $\mathbf{u}^{AB} = 2\mathbf{u}^n - \mathbf{u}^{n-1}$ in the second order case. Since in practice α and Δt always occur together, we let $\Delta t = \alpha\widehat{\Delta t}$. $\hat{\gamma}^{n+1}$ represents an estimate of the final γ obtained by solving this discretized equation; it will be later updated to the final γ^{n+1} bounded to the range $[0, 1]$ using the method described in Section 2.3.1.

Following Shen and Yang [74], we introduce a term $2\tau\left(\hat{\gamma}^{n+1} - \gamma^{AB}\right)$ to help with splitting the equation. The choice of τ is discussed below. Since both $\hat{\gamma}^{n+1}$ and γ^{AB} are estimates of γ^{n+1}, this term vanishes rapidly under refinement.

$$\frac{\hat{\gamma}^{n+1} - \gamma^{BD}}{\widehat{\Delta t}} + \nabla \cdot \left(\mathbf{u}^{AB}\gamma^{AB}\right) = M\lambda\nabla^2\left(F'\left(\gamma^{AB}\right) - \nabla^2\hat{\gamma}^{n+1} + 2\tau\left(\hat{\gamma}^{n+1} - \gamma^{AB}\right)\right) + S_\gamma^{n+1} \tag{2.11}$$

Next we split out the advection term as an update from γ^{BD} to γ^*:

$$\frac{\gamma^* - \gamma^{BD}}{\widehat{\Delta t}} + \nabla \cdot \left(\mathbf{u}^{AB}\gamma^{AB}\right) = 0 \tag{2.12}$$

$$\frac{\hat{\gamma}^{n+1} - \gamma^*}{\widehat{\Delta t}} = M\lambda\nabla^2\left(F'\left(\gamma^{AB}\right) - \nabla^2\hat{\gamma}^{n+1} + 2\tau\left(\hat{\gamma}^{n+1} - \gamma^{AB}\right)\right) + S_\gamma^{n+1}. \tag{2.13}$$

We group all explicit terms under the Laplacian into a new term A:

$$A = \frac{1}{\tau}F'\left(\gamma^{AB}\right) - 2\gamma^{AB} \tag{2.14}$$

$$\frac{\hat{\gamma}^{n+1} - \gamma^*}{\widehat{\Delta t}} = M\lambda\nabla^2\left(\tau A - \nabla^2\hat{\gamma}^{n+1} + 2\tau\hat{\gamma}^{n+1}\right) + S_\gamma^{n+1} \tag{2.15}$$

Grouping together $\hat{\gamma}^{n+1}$ with $\nabla^2\hat{\gamma}^{n+1}$ on both sides of the equation:

$$\frac{\left(\hat{\gamma}^{n+1} - \tau M\lambda\widehat{\Delta t}\nabla^2\hat{\gamma}^{n+1} + A\right) - \gamma^*}{\widehat{\Delta t}} = \tau M\lambda\nabla^2\left(\hat{\gamma}^{n+1} - \frac{1}{\tau}\nabla^2\hat{\gamma}^{n+1} + A\right) + \frac{A}{\widehat{\Delta t}} + S_\gamma^{n+1}. \tag{2.16}$$

For the two parenthesized expressions to match, we need $\tau^2 M\lambda\widehat{\Delta t} = 1$. We achieve this by letting

$$s = \sqrt{\frac{M\lambda}{\widehat{\Delta t}}} \qquad \tau = \frac{1}{M\lambda}s \tag{2.17}$$

and define

$$\gamma' = \hat{\gamma}^{n+1} - s\widehat{\Delta t}\nabla^2\hat{\gamma}^{n+1} + A. \tag{2.18}$$

With these definitions, equation (2.16) becomes

$$\frac{\gamma' - \gamma^*}{\widehat{\Delta t}} = s\nabla^2\gamma' + \frac{1}{\widehat{\Delta t}}A + S_\gamma^{n+1}. \tag{2.19}$$

Observe that (2.18) and (2.19) are implicit Helmholtz equations for $\hat{\gamma}^{n+1}$ and γ', respectively.

Cahn-Hilliard bounds-respecting redistribution scheme

When solving the Cahn-Hilliard equation, numerical errors or sufficiently large time steps can result in γ outside the range $[0, 1]$. Given a large density ratio between the fluids, this can result in negative densities from (2.5). In order to prevent this, we use a redistribution scheme for γ as detailed in Huang et al. [46] adapted for the range $[0, 1]$.

First $\hat{\gamma}^{n+1}$ is clamped to the feasible range at each index i, j:

$$\gamma_{i,j}^{b*} = \begin{cases} 1, & \text{if } \hat{\gamma}_{i,j}^{n+1} \geq 1 \\ 0, & \text{if } \hat{\gamma}_{i,j}^{n+1} \leq 0 \\ \hat{\gamma}_{i,j}^{n+1}, & \text{otherwise.} \end{cases} \tag{2.20}$$

The total difference between γ^{b*} and $\hat{\gamma}^{n+1}$ is then redistributed among all indices using a weight function:

$$W_b(\gamma) = 4\gamma - 4\gamma^2 \tag{2.21}$$

$$\gamma_{i,j}^{n+1} = \gamma_{i,j}^{b*} + \frac{W_b\left(\gamma_{i,j}^{b*}\right)}{\sum_{r,s} W_b\left(\gamma_{r,s}^{b*}\right)} \sum_{r,s} \left(\hat{\gamma}_{r,s}^{n+1} - \gamma_{r,s}^{b*}\right). \tag{2.22}$$

The indices r, s are over the entire computational domain, and a uniform grid is assumed. Since this update is globally conservative, we can express the change in the final quantity γ^{n+1} as the divergence of an unknown weighted gradient term $W_b\left(\gamma^{n+1}\right)\nabla Q$ with no-flux boundary conditions. This results in a Poisson equation for Q:

$$\frac{\gamma^{n+1}-\hat{\gamma}^{n+1}}{\widehat{\Delta t}} = \nabla\cdot\left(W_b\left(\gamma^{n+1}\right)\nabla Q\right), \tag{2.23}$$

$$\mathbf{n}\cdot\nabla Q = 0 \tag{2.24}$$

which we solve and use to compute the density flux $\mathbf{m}$ (See Section 2.3.2).

Cahn-Hilliard boundary conditions

In this chapter, we consider two types of boundary conditions for γ: periodic and Neumann ($\mathbf{n}\cdot\nabla\hat{\gamma}^{n+1}=0$). Since the Cahn-Hilliard equation is fourth order, we require another boundary condition; Noting (2.13)

$$\frac{\hat{\gamma}^{n+1}-\gamma^{*}}{\widehat{\Delta t}} = M\lambda\nabla^2\left(F'(\gamma^{AB}) - \nabla^2\hat{\gamma}^{n+1} + \frac{2s}{M\lambda}\left(\hat{\gamma}^{n+1}-\gamma^{AB}\right)\right) + S_{\gamma}^{n+1} \tag{2.25}$$

we define ξ^* to be a discrete version of the chemical potential from (2.2) as

$$\xi^* = \lambda\left(F'\left(\gamma^{AB}\right) - \nabla^2\hat{\gamma}^{n+1} + \frac{2s}{M\lambda}\left(\hat{\gamma}^{n+1}-\gamma^{AB}\right)\right) \tag{2.26}$$

$$= \lambda\left(\tau A - \nabla^2\hat{\gamma}^{n+1} + 2\tau\hat{\gamma}^{n+1}\right) \tag{2.27}$$

$$= \tau\lambda\left(\hat{\gamma}^{n+1} - \frac{1}{\tau}\nabla^2\hat{\gamma}^{n+1} + A + \hat{\gamma}^{n+1}\right) \tag{2.28}$$

$$= \frac{s}{M}\left(\gamma' + \hat{\gamma}^{n+1}\right). \tag{2.29}$$

Following [47] we use the boundary condition $\mathbf{n} \cdot \nabla \xi^* = 0$, which leads to $\mathbf{n} \cdot \nabla \gamma' = 0$. This gives us the necessary boundary conditions for both of our Helmholtz systems.

2.3.2 Navier-Stokes equations

Navier-Stokes temporal discretization

As in Section 2.3.1, we discretize the time derivative as $\frac{\alpha \rho^{n+1} \mathbf{u}^{n+1} - \alpha (\rho \mathbf{u})^{BD}}{\Delta t}$. For the first time step, $\alpha = 1$ and $(\rho \mathbf{u})^{BD} = \rho^n \mathbf{u}^n$. To achieve second-order accuracy, we thereafter use a backwards-difference scheme with $\alpha = \frac{3}{2}$ and $(\rho \mathbf{u})^{BD} = \frac{4}{3} \rho^n \mathbf{u}^n - \frac{1}{3} \rho^{n-1} \mathbf{u}^{n-1}$. Explicit quantities for $\mathbf{u}$ are discretized using Adams-Bashforth, where $\mathbf{u}^{AB} = \mathbf{u}^n$ in the first time step and $\mathbf{u}^{AB} = 2\mathbf{u}^n - \mathbf{u}^{n-1}$ afterwards. As before, we use $\Delta t = \alpha \widehat{\Delta t}$ to simplify the equations.

In addition to these terms, $\mathbf{u}^v$ is an intermediate estimate of $\mathbf{u}^{n+1}$ using an approximation for pressure, which is computed in an intermediate implicit solve, and $\mathbf{m}$ is the total density flux detailed in Section 2.3.2. With these, (2.9) is discretized as

$$\begin{aligned} \frac{\rho^{n+1} \mathbf{u}^{n+1} - (\rho \mathbf{u})^{BD}}{\widehat{\Delta t}} + \nabla \cdot \left(\mathbf{m} \otimes \mathbf{u}^{AB} \right) = & -\nabla p^{n+1} + \rho^{n+1} g + \sigma \kappa \nabla (g(\gamma)) \\ & + \nabla \cdot \left(\mu^{n+1} \left(\nabla \mathbf{u}^v + \left(\nabla \mathbf{u}^{AB} \right)^T \right) \right) + S_{\mathbf{u}}^{n+1}. \end{aligned} \tag{2.30}$$

The intermediate $\mathbf{u}^*$ is introduced to represent the result of the momentum advection and also the evolution of density through the Cahn-Hilliard equation. When the Cahn-Hilliard equation causes mass to move around, the momentum carried by that mass must move with it. Otherwise mass and momentum may become inconsistent. Following [47] this is accomplished through the mass flux term $\mathbf{m}$, which we derive in Section 2.3.2.

$$\frac{\rho^{n+1}\mathbf{u}^* - (\rho\mathbf{u})^{BD}}{\widehat{\Delta t}} + \nabla \cdot \left(\mathbf{m} \otimes \mathbf{u}^{AB}\right) = 0 \tag{2.31}$$

$$\begin{aligned}\frac{\rho^{n+1}\mathbf{u}^{n+1} - \rho^{n+1}\mathbf{u}^*}{\widehat{\Delta t}} = &-\nabla p^{n+1} + \rho^{n+1} g + \sigma\kappa\nabla(g\left(\gamma^{n+1}\right)) \\ &+ \nabla \cdot \left(\mu^{n+1}\left(\nabla\mathbf{u}^v + \left(\nabla\mathbf{u}^{AB}\right)^T\right)\right) + S_{\mathbf{u}}^{n+1}.\end{aligned} \tag{2.32}$$

After updating momentum according to equation (2.31), we divide the result through by ρ^{n+1} and formulate equation (2.32) as updates to velocity, beginning with explicit forces and pressure. We split pressure here into predicted and correction parts as $p^{n+1} = p^n + p'$.

$$\begin{aligned}\frac{\mathbf{u}^{**} - \mathbf{u}^*}{\widehat{\Delta t}} = &-\frac{1}{\rho^{n+1}}\nabla p^n + g + \frac{1}{\rho^{n+1}}\sigma\kappa\nabla(g\left(\gamma^{n+1}\right)) + \frac{1}{\rho^{n+1}}\nabla \cdot \left(\mu^{n+1}\left(\nabla\mathbf{u}^{AB}\right)^T\right) \\ &+ \frac{1}{\rho^{n+1}} S_{\mathbf{u}}^{n+1}\end{aligned} \tag{2.33}$$

$$\frac{\mathbf{u}^{n+1} - \mathbf{u}^{**}}{\widehat{\Delta t}} = -\frac{1}{\rho^{n+1}}\nabla p' + \frac{1}{\rho^{n+1}}\nabla \cdot \left(\mu^{n+1}\nabla\mathbf{u}^v\right) \tag{2.34}$$

Finally, we compute the effects of viscosity implicitly and then project the velocity to be divergence free:

$$\frac{\mathbf{u}^v - \mathbf{u}^{**}}{\widehat{\Delta t}} = \frac{1}{\rho^{n+1}}\nabla \cdot \left(\mu^{n+1}\nabla\mathbf{u}^v\right) \tag{2.35}$$

$$\nabla \cdot \left(\frac{1}{\rho^{n+1}}\nabla p'\right) = \frac{\nabla \cdot \mathbf{u}^v}{\widehat{\Delta t}} \tag{2.36}$$

$$\frac{\mathbf{u}^{n+1} - \mathbf{u}^v}{\widehat{\Delta t}} = -\frac{1}{\rho^{n+1}}\nabla p'. \tag{2.37}$$

Momentum flux

Since we are solving the Cahn-Hilliard equation, we do not directly evolve density. Instead, $\gamma^n \to \gamma^{n+1}$ is evolved according to the Cahn-Hilliard equation, and then (2.5) is used to compute ρ^{n+1}. The discrete γ evolution in Section 2.3.1 implies a density evolution of the form

$$\frac{\rho^{n+1} - \rho^{BD}}{\widehat{\Delta t}} + \nabla \cdot \mathbf{m} = S_m^{n+1}, \tag{2.38}$$

where $\mathbf{m}$ includes advection and Cahn-Hilliard separation, and S_m takes the effects of the forcing term S_γ. Using (2.5), we express $\mathbf{m}$ in terms of γ:

$$\begin{aligned}
\nabla \cdot \mathbf{m} &= -\frac{\rho^{n+1} - \rho^{BD}}{\widehat{\Delta t}} + S_m^{n+1} && (2.39)\\
&= -\left(\rho_1 - \rho_0\right) \frac{\gamma^{n+1} - \gamma^{BD}}{\widehat{\Delta t}} + S_m^{n+1} && (2.40)\\
&= -\left(\rho_1 - \rho_0\right) \left(\frac{\gamma^{n+1} - \hat{\gamma}^{n+1}}{\widehat{\Delta t}} + \frac{\hat{\gamma}^{n+1} - \gamma'}{\widehat{\Delta t}} + \frac{\gamma' - \gamma^*}{\widehat{\Delta t}} + \frac{\gamma^* - \gamma^{BD}}{\widehat{\Delta t}} \right) + S_m^{n+1}. && (2.41)
\end{aligned}$$

Using the update rules (2.12), (2.19), (2.18), and (2.23), defining $S_m^{n+1} = \left(\rho_1 - \rho_0\right) S_\gamma^{n+1}$, and canceling terms, this becomes

$$\nabla \cdot \mathbf{m} = \left(\rho_1 - \rho_0\right) \left(\nabla \cdot \left(\mathbf{u}^{AB} \gamma^{AB} \right) - \nabla \cdot \left(s \nabla \gamma' + s \nabla \hat{\gamma}^{n+1} + W_b \left(\gamma^{n+1} \right) \nabla Q \right) \right) \tag{2.42}$$

Note that this definition of $\mathbf{m}$ is only well-defined up to a divergence-free shift. To determine what shift is necessary, we consider the case of $\rho_0 = \rho_1$, in which case Cahn-Hilliard has no affect on the density evolution and the mass flux is purely comprised of advection. This

suggests the shift $\nabla \cdot \left(\rho_0 \mathbf{u}^{AB}\right)$ so that

$$\nabla \cdot \mathbf{m} = \nabla \cdot \left(\rho_0 \mathbf{u}^{AB}\right) + (\rho_1 - \rho_0)\left(\nabla \cdot \left(\mathbf{u}^{AB}\gamma^{AB}\right) - \nabla \cdot \left(s\nabla\gamma' + s\nabla\hat{\gamma}^{n+1} + W_b\left(\gamma^{n+1}\right)\nabla Q\right)\right), \tag{2.43}$$

which is consistent with the shift in [47]. Observe that ρ_0 is a constant and $\mathbf{u}^{AB}$ is discretely divergence free, so adding this term does not affect the value of $\nabla \cdot \mathbf{m}$. This leads to a definition of

$$\mathbf{m} = \rho_0 \mathbf{u}^{AB} + (\rho_1 - \rho_0)\left(\mathbf{u}^{AB}\gamma^{AB} - s\nabla\gamma' - s\nabla\hat{\gamma}^{n+1} - W_b\left(\gamma^{n+1}\right)\nabla Q\right). \tag{2.44}$$

To ensure consistency with the discretization of the Cahn-Hilliard equation, $\mathbf{u}^{AB}\gamma^{AB}$ is replaced by the flux computed by the WENO advection described in Section 2.3.3.

Surface tension discretization

For surface tension, we use a Continuum Surface Force [11, 30] formulation:

$$\sigma\kappa\nabla(g(\gamma)), \tag{2.45}$$

where κ is the estimated interface curvature:

$$\kappa = -\nabla \cdot \left(\frac{\nabla\gamma}{||\nabla\gamma||}\right). \tag{2.46}$$

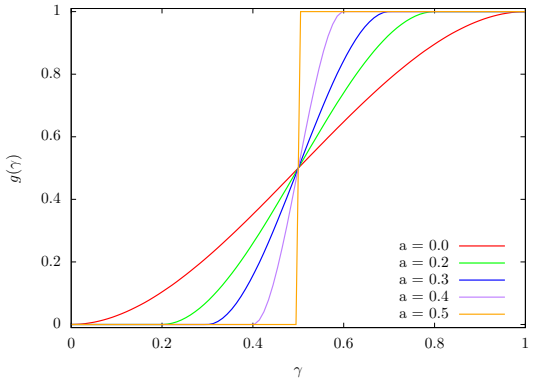

Figure 2.1: $g(\gamma)$ vs γ for different values of a

We formulate $g(\gamma)$ to ensure that the surface tension force is exactly 0 a finite distance away from the interface. We choose a piecewise cubic approximation of a Heaviside function whose transition occurs between a and $1-a$ for some value $a \in [0, 0.5]$. Since $g(\gamma)$ approximates a Heaviside function, $\nabla g(\gamma)$ approximates a delta function times the normal. This is similar to the method used in [57], but it differs in that they use a level set function to track the interface rather than the phase-field approach used here and in the choice of Heaviside approximation.

As depicted in Figure 2.1, we define $g(\gamma)$ as

$$g(\gamma) = \begin{cases} 1, & \text{if } \gamma \geq 1-a \\ 0, & \text{if } \gamma < a \\ \frac{(-\gamma+a)^2(2\gamma+4a-3)}{(2a-1)^3}, & \text{otherwise.} \end{cases} \tag{2.47}$$

In practice, we've found $a = 0.2$ works well, and at $a = 0.5$ we recover a sharp interface force, as used in [51].

We can see that this surface tension formulation is consistent with the standard one by considering a path that crosses the band near the interface where the force is nonzero. Given any path C (see Figure 2.2), with discretization $i = 0, ..., N$, that crosses the fluid interface, the total force per unit area is:

$$\int_C \sigma\kappa\nabla(g(\gamma)) \cdot dl \approx \sigma \left(\sum_{i=1}^{N} \kappa_i \left(g(\gamma_i) - g(\gamma_{i-1}) \right) \right). \tag{2.48}$$

Assume that $g(\gamma_N) = 1$ and $g(\gamma_0) = 0$, so that the curve crosses completely from one phase to the other. Let κ_I denote the curvature at the interface. If we assume the path is localized and approximate the curvature as constant, so that $\kappa_i = \kappa_I$, (2.48) reduces to:

$$\sigma \left(\sum_{i=1}^{N} \kappa_i \left(g(\gamma_i) - g(\gamma_{i-1}) \right) \right) = \sigma\kappa_I \left(g(\gamma_N) - g(\gamma_0) \right) = \sigma\kappa_I, \tag{2.49}$$

which is the ideal pressure jump caused by surface tension. In reality, the curvature will not be constant, but when the interface width is small and the curvature is sufficiently smooth,

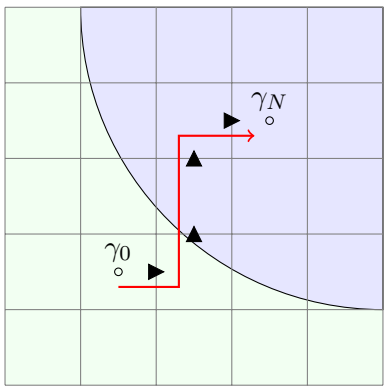

Figure 2.2: Example path $\gamma_0 \to \gamma_N$. The triangles represent the pressure jumps along this path.

we can write $\kappa_i = \kappa_I + O(\Delta x)$, so that the approximate pressure jump is

$$\sigma \left(\sum_{i=1}^{N} \kappa_i \left(g(\gamma_i) - g(\gamma_{i-1}) \right) \right) = \sigma \kappa_I + O(\Delta x). \tag{2.50}$$

This suggests that smearing the pressure jump over a transition region using $g(\gamma)$ can give a consistent discretization of the surface tension force. We next show this explicitly for our discretization of the pressure Poisson equation (2.36).

For the pressure projection equation, we solve $\nabla \cdot (\beta \nabla p') = \nabla \cdot \mathbf{u}^v$ with $\beta = \frac{\widehat{\Delta t}}{\rho^{n+1}}$. The standard five-point discretization of this equation in two dimensions is given by

$$\begin{aligned} &\frac{\beta_{i+\frac{1}{2},j}\left(p'_{i+1,j} - p'_{i,j}\right) - \beta_{i-\frac{1}{2},j}\left(p'_{i,j} - p'_{i-1,j}\right)}{\Delta x^2} + \\ &\frac{\beta_{i,j+\frac{1}{2}}\left(p'_{i,j+1} - p'_{i,j}\right) - \beta_{i,j-\frac{1}{2}}\left(p'_{i,j} - p'_{i,j-1}\right)}{\Delta y^2} = \left(\nabla \cdot \mathbf{u}^v\right)_{i,j}. \end{aligned} \tag{2.51}$$

Following [51], an interface can be treated in a sharp manner by incorporating the pressure jump J across the interface into the equation. Incorporating a jump term (which may be 0) across every difference in the stencil, the discretization becomes

$$\begin{aligned} &\frac{\beta_{i+\frac{1}{2},j}\left(p'_{i+1,j} - \left(p'_{i,j} + J_{i+\frac{1}{2},j}\right)\right) - \beta_{i-\frac{1}{2},j}\left(p'_{i,j} - \left(p'_{i-1,j} + J_{i-\frac{1}{2},j}\right)\right)}{\Delta x^2} + \\ &\frac{\beta_{i,j+\frac{1}{2}}\left(p'_{i,j+1} - \left(p'_{i,j} + J_{i,j+\frac{1}{2}}\right)\right) - \beta_{i,j-\frac{1}{2}}\left(p'_{i,j} - \left(p'_{i,j-1} + J_{i,j-\frac{1}{2}}\right)\right)}{\Delta y^2} = \left(\nabla \cdot \mathbf{u}^v\right)_{i,j}. \end{aligned} \tag{2.52}$$

Moving all terms with jumps to the right hand side, we get

$$\frac{\beta_{i+\frac{1}{2},j}\left(p'_{i+1,j}-p'_{i,j}\right)-\beta_{i-\frac{1}{2},j}\left(p'_{i,j}-p'_{i-1,j}\right)}{\Delta x^2}+\frac{\beta_{i,j+\frac{1}{2}}\left(p'_{i,j+1}-p'_{i,j}\right)-\beta_{i,j-\frac{1}{2}}\left(p'_{i,j}-p'_{i,j-1}\right)}{\Delta y^2}$$
$$=\left(\nabla\cdot\mathbf{u}^v\right)_{i,j}+\frac{\beta_{i+\frac{1}{2},j}J_{i+\frac{1}{2},j}-\beta_{i-\frac{1}{2},j}J_{i-\frac{1}{2},j}}{\Delta x^2}+\frac{\beta_{i,j+\frac{1}{2}}J_{i,j+\frac{1}{2}}-\beta_{i,j-\frac{1}{2}}J_{i,j-\frac{1}{2}}}{\Delta y^2}. \tag{2.53}$$

With the central difference discretization of divergence

$$\left(\nabla\cdot\mathbf{u}^v\right)_{i,j}=\frac{u^v_{i+\frac{1}{2},j}-u^v_{i-\frac{1}{2},j}}{\Delta x}+\frac{v^v_{i,j+\frac{1}{2}}-v^v_{i,j-\frac{1}{2}}}{\Delta y}, \tag{2.54}$$

and with $\hat{\mathbf{J}}=\left(\frac{J_x}{\Delta x},\frac{J_y}{\Delta y}\right)$, Equation (2.53) becomes

$$\begin{aligned}&\frac{\beta_{i+\frac{1}{2},j}\left(p'_{i+1,j}-p'_{i,j}\right)-\beta_{i-\frac{1}{2},j}\left(p'_{i,j}-p'_{i-1,j}\right)}{\Delta x^2}+\\&\frac{\beta_{i,j+\frac{1}{2}}\left(p'_{i,j+1}-p'_{i,j}\right)-\beta_{i,j-\frac{1}{2}}\left(p'_{i,j}-p'_{i,j-1}\right)}{\Delta y^2}=\left(\nabla\cdot\left(\mathbf{u}^v+\beta\hat{\mathbf{J}}\right)\right)_{i,j}.\end{aligned} \tag{2.55}$$

We define the pressure jump at $\left(i+\frac{1}{2},j\right)$ to be

$$J_{i+\frac{1}{2},j}=\sigma\kappa_{i+\frac{1}{2},j}\left(g\left(\gamma_{i+1,j}\right)-g\left(\gamma_{i,j}\right)\right). \tag{2.56}$$

The discretization of the x component of the surface tension force (2.45) is then

$$\sigma\kappa_{i+\frac{1}{2},j}\left(\frac{\partial g}{\partial x}\left(\gamma\right)\right)_{i+\frac{1}{2},j}\approx\sigma\kappa_{i+\frac{1}{2},j}\frac{g\left(\gamma_{i+1,j}\right)-g\left(\gamma_{i,j}\right)}{\Delta x}=\frac{1}{\Delta x}J_{i+\frac{1}{2},j}, \tag{2.57}$$

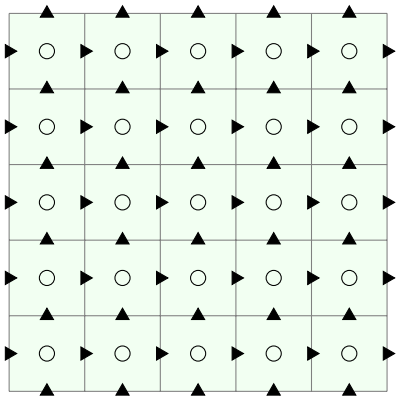

Figure 2.3: The MAC grid stores velocties on faces (represented by triangles), and γ and pressure on cell centers (circles).

which is similar to [30]. Therefore

$$\beta\hat{\mathbf{J}} = \frac{\widehat{\Delta t}}{\rho^{n+1}}\sigma\kappa\nabla g\left(\gamma\right), \tag{2.58}$$

which shows that solving the Poisson equation with the above defined pressure jumps is equivalent to applying surface tension with other explicit forces:

$$\nabla\cdot\left(\frac{\widehat{\Delta t}}{\rho^{n+1}}\nabla p'\right) = \nabla\cdot\left(\mathbf{u}^{v} + \frac{\widehat{\Delta t}}{\rho^{n+1}}\sigma\kappa\nabla g\left(\gamma\right)\right). \tag{2.59}$$

Therefore we apply surface tension as in (2.59), and we can recover the sharp formulation of [51] by choosing $a = 0.5$ in the definition of $g\left(\gamma\right)$.

2.3.3 Spatial Discretization

We use a uniform MAC grid (Figure 2.3) with γ and pressure stored at cell centers. Velocities are split by components and stored on cell faces. Unless otherwise specified, all divergences are central differences from faces to cells and all gradients are central differences

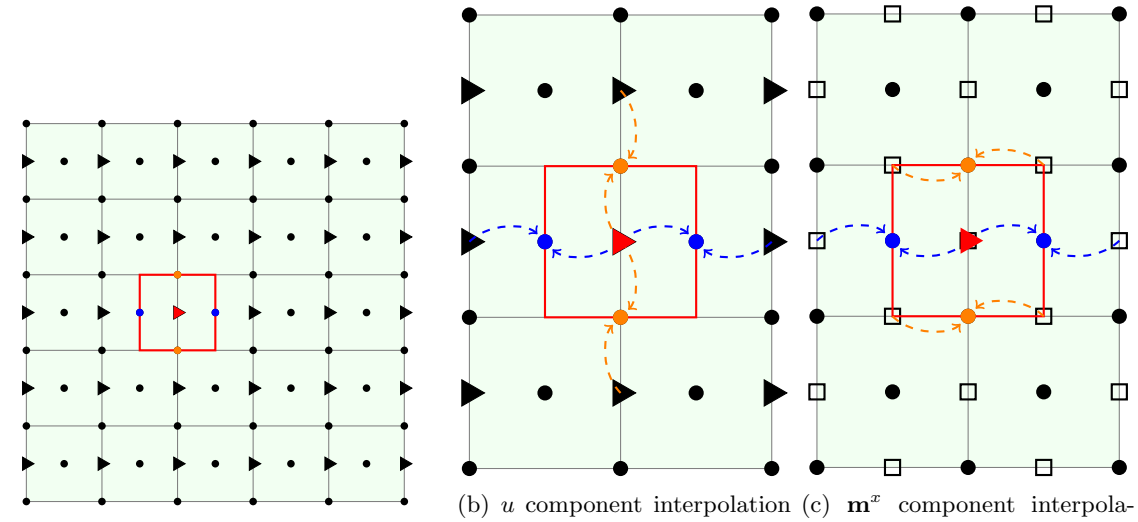

(a) Flux locations around u component.

(b) u component interpolation for flux.

(c) $\mathbf{m}^x$ component interpolation for flux.

Figure 2.4: The components of the momentum flux for updating the x component of momentum in 2D are shown in 2.4a. The momentum at the red triangle will be updated with the fluxes at the surrounding blue and orange dots. The u and $\mathbf{m}^x$ values at these dots are interpolated from neighboring values as illustrated in 2.4b and 2.4c, respectively.

from cells to faces. All Poisson equations are discretized using the standard five-point central difference stencil, with standard treatment of axis-aligned boundary conditions.

Advective flux for γ

When computing the divergence operator for γ advection in (2.12), we use a flux-based 5th order WENO advection scheme [50] with local Lax-Friedrichs [78]. The WENO flux $\mathcal{F}^W$ is stored for later use in the momentum flux $\mathbf{m}$.

Divergence operator (momentum advection)

The divergence operator for momentum advection is discretized as a central difference from dual-cell faces to MAC grid faces, as shown in Figure 2.4. The components of the divergence $\nabla \cdot (\mathbf{m} \otimes \mathbf{u})$ are needed at MAC faces to update the components of our

velocities. Correspondingly we discretize $\nabla \cdot (\mathbf{m}^x u)$ and $\nabla \cdot (\mathbf{m}^y v)$ at MAC x-faces and y-faces respectively. For example, $\mathbf{m}^x$ is interpolated to faces of a uniform dual grid centered on the x-faces:

$$\mathbf{m}^x_{i,j} = \frac{\mathbf{m}_{i+1/2,j} + \mathbf{m}_{i-1/2,j}}{2} \tag{2.60}$$

$$\mathbf{m}^x_{i+1/2,j+1/2} = \frac{\mathbf{m}_{i+1,j+1/2} + \mathbf{m}_{i,j+1/2}}{2}. \tag{2.61}$$

We also interpolate u to the same dual grid faces

$$u_{i,j} = \frac{u_{i+1/2,j} + u_{i-1/2,j}}{2} \tag{2.62}$$

$$u_{i+1/2,j+1/2} = \frac{u_{i+1/2,j+1} + u_{i+1/2,j}}{2}. \tag{2.63}$$

The final component divergence is discretized as

$$\begin{aligned}(\nabla \cdot (\mathbf{m}^x u))_{i+1/2,j} = &\frac{\mathbf{m}^x_{i+1,j} u_{i+1,j} - \mathbf{m}^x_{i,j} u_{i,j}}{\Delta x} \\ &+ \frac{\mathbf{m}^x_{i+1/2,j+1/2} u_{i+1/2,j+1/2} - \mathbf{m}^x_{i+1/2,j-1/2} u_{i+1/2,j-1/2}}{\Delta y}.\end{aligned} \tag{2.64}$$

The $\mathbf{m}^y$ term is discretized analogously.

Divergence gradient transpose

In (2.33), we discretize the $\nabla \cdot \left(\mu \left(\nabla \mathbf{u}\right)^T\right)$ term following [47], which we show here:

$$\begin{aligned}\left(\nabla \cdot \left(\mu \left(\nabla \mathbf{u}\right)^T\right)\right)_{i,j} &= \frac{1}{\Delta x}\left(\mu_{i+1/2,j}\frac{u_{i+1,j}-u_{i,j}}{\Delta x} - \mu_{i-1/2,j}\frac{u_{i,j}-u_{i-1,j}}{\Delta x}\right) \\ &+ \frac{1}{\Delta y}\left(\mu_{i,j+1/2}\frac{v_{i+1/2,j+1/2}-v_{i-1/2,j+1/2}}{\Delta x} - \mu_{i,j-1/2}\frac{v_{i+1/2,j-1/2}-v_{i-1/2,j-1/2}}{\Delta x}\right) \\ &+ \frac{1}{\Delta y}\left(\mu_{i,j+1/2}\frac{v_{i,j+1}-v_{i,j}}{\Delta y} - \mu_{i,j-1/2}\frac{v_{i,j}-v_{i,j-1}}{\Delta y}\right) \\ &+ \frac{1}{\Delta x}\left(\mu_{i+1/2,j}\frac{u_{i+1/2,j+1/2}-u_{i+1/2,j-1/2}}{\Delta y} - \mu_{i-1/2,j}\frac{u_{i-1/2,j+1/2}-u_{i-1/2,j-1/2}}{\Delta y}\right).\end{aligned} \tag{2.65}$$

This discretization is used to ensure discrete consistency when μ is constant, such that

$$\nabla \cdot \left(\mu \left(\nabla \mathbf{u}\right)^T\right) = \mu \nabla \left(\nabla \cdot \mathbf{u}\right) = 0 \tag{2.66}$$

is satisfied and momentum is conserved [47].

Interface curvature

The Balanced-Force algorithm [30] requires that the surface tension force is discretized at the same spatial location as the pressure gradient. When calculating the estimated interface curvature κ,

$$\kappa = -\nabla \cdot \left(\frac{\nabla \gamma}{||\nabla \gamma||}\right), \tag{2.67}$$

we smooth the curvature estimate by computing the divergence on cells and interpolating to faces. We calculate $\nabla\gamma$ as individual components $\nabla\gamma^x, \nabla\gamma^y$ on faces,

$$\nabla\gamma^x_{i+1/2,j} = \frac{\gamma_{i+1,j} - \gamma_{i,j}}{\Delta x}, \tag{2.68}$$

which we interpolate to cell centers as vectors in order to normalize:

$$\widetilde{\nabla\gamma}_{i,j} = \left(\frac{\nabla\gamma^x_{i+1/2,j} + \nabla\gamma^x_{i-1/2,j}}{2}, \frac{\nabla\gamma^y_{i,j+1/2} + \nabla\gamma^y_{i,j-1/2}}{2} \right). \tag{2.69}$$

The normalized gradients are interpolated back to faces as full vectors:

$$\widehat{\nabla\gamma}_{i+1/2,j} = \frac{1}{2}\left(\frac{\widetilde{\nabla\gamma}_{i+1,j}}{||\widetilde{\nabla\gamma}_{i+1,j}||} + \frac{\widetilde{\nabla\gamma}_{i,j}}{||\widetilde{\nabla\gamma}_{i,j}||} \right). \tag{2.70}$$

From these gradient vectors on faces, we calculate the divergence at cell centers

$$\nabla \cdot \left(\widehat{\nabla\gamma}\right)_{i,j} = \frac{1}{\Delta x}\left(\widehat{\nabla\gamma}^x_{i+1/2,j} - \widehat{\nabla\gamma}^x_{i-1/2,j}\right) + \frac{1}{\Delta y}\left(\widehat{\nabla\gamma}^y_{i,j+1/2} - \widehat{\nabla\gamma}^y_{i,j-1/2}\right), \tag{2.71}$$

and interpolate to faces:

$$\kappa_{i+1/2,j} = -\frac{\nabla \cdot \left(\widehat{\nabla\gamma}\right)_{i+1,j} + \nabla \cdot \left(\widehat{\nabla\gamma}\right)_{i,j}}{2}. \tag{2.72}$$

2.3.4 Discretization summary

We finish our treatment of discretization with a summary of the full algorithm. First, the Adams-Bashforth and backwards-difference quantities γ^{BD} and γ^{AB} on cell cen-

ters and $(\rho\mathbf{u})^{BD}$ and $\mathbf{u}^{AB}$ on cell faces are computed from the known initial quantities and previous time step quantities. The initial time step is computed with first order time discretizations:

$$\gamma^{BD} = \gamma^n \qquad \gamma^{AB} = \gamma^n \qquad (\rho\mathbf{u})^{BD} = \rho^n\mathbf{u}^n \qquad \mathbf{u}^{AB} = \mathbf{u}^n \qquad \widehat{\Delta t} = \Delta t, \tag{2.73}$$

and successive time steps with second order:

$$\begin{aligned} &\gamma^{BD} = \frac{4}{3}\gamma^n - \frac{1}{3}\gamma^{n-1} \qquad \gamma^{AB} = 2\gamma^n - \gamma^{n-1} \qquad (\rho\mathbf{u})^{BD} = \frac{4}{3}\rho^n\mathbf{u}^n - \frac{1}{3}\rho^{n-1}\mathbf{u}^{n-1} \\ &\mathbf{u}^{AB} = 2\mathbf{u}^n - \mathbf{u}^{n-1} \qquad \widehat{\Delta t} = \frac{2}{3}\Delta t. \end{aligned} \tag{2.74}$$

Cahn-Hilliard discretization

Unlike [47], we observed better results using a WENO advection scheme (Section 2.3.3) to compute γ^* from γ^{BD}. The flux $\mathcal{F}^W$ from this operation is stored for later use in $\mathbf{m}$. These terms are related by:

$$\gamma^*_{i,j} = \gamma^{BD}_{i,j} - \widehat{\Delta t}\left(\frac{\mathcal{F}^W_{i+1/2,j} - \mathcal{F}^W_{i-1/2,j}}{\Delta x} + \frac{\mathcal{F}^W_{i,j+1/2} - \mathcal{F}^W_{i,j-1/2}}{\Delta y}\right). \tag{2.75}$$

Next we compute $\hat{\gamma}^{n+1}$ from γ^* by solving two Helmholtz equations:

$$\lambda = \frac{3}{2\sqrt{2}}\sigma\eta \qquad s = \sqrt{\frac{M\lambda}{\widehat{\Delta t}}} \qquad A = \frac{M\lambda}{s}F'\left(\gamma^{AB}\right) - 2\gamma^{AB} \tag{2.76}$$

$$\gamma' - s\widehat{\Delta t}\nabla^2\gamma' = \gamma^* + A + \widehat{\Delta t}S^{n+1}_\gamma \tag{2.77}$$

$$\hat{\gamma}^{n+1} - s\widehat{\Delta t}\nabla^2\hat{\gamma}^{n+1} = \gamma' - A. \tag{2.78}$$

We obtain the final γ^{n+1} through the redistribution scheme described in Section 2.3.1. The flux corresponding to the redistribution is found with a Poisson solve:

$$\gamma_{i,j}^{b*} = \begin{cases} 1, & \text{if } \hat{\gamma}_{i,j}^{n+1} \geq 1 \\ 0, & \text{if } \hat{\gamma}_{i,j}^{n+1} \leq 0 \\ \hat{\gamma}_{i,j}^{n+1}, & \text{otherwise.} \end{cases} \tag{2.79}$$

$$W_b(\gamma) = 4\gamma - 4\gamma^2 \tag{2.80}$$

$$\gamma_{i,j}^{n+1} = \gamma_{i,j}^{b*} + \frac{W_b\left(\gamma_{i,j}^{b*}\right)}{\sum\limits_{r,s} W_b\left(\gamma_{r,s}^{b*}\right)} \sum_{r,s} \left(\hat{\gamma}_{r,s}^{n+1} - \gamma_{r,s}^{b*}\right) \tag{2.81}$$

$$\widehat{\Delta t} \nabla \cdot \left(W_b\left(\gamma^{n+1}\right) \nabla Q\right) = \gamma^{n+1} - \hat{\gamma}^{n+1}. \tag{2.82}$$

To avoid rows of all zeros in our Poisson matrix, we follow [46] in replacing $W_b\left(\gamma^{n+1}\right)$ with $\max\left(W_b\left(\gamma^{n+1}\right), 10^{-6}\right)$ in (2.82). Using the above, we can compute the discrete mass flux, which should satisfy (2.38) to round-off error:

$$\mathbf{m} = \rho_0 \mathbf{u}^{AB} + (\rho_1 - \rho_0)\left(\mathcal{F}^W - s\nabla\gamma' - s\nabla\hat{\gamma}^{n+1} - W_b\left(\gamma^{n+1}\right)\nabla Q\right). \tag{2.83}$$

The density and viscosity are computed on faces using γ^{n+1} that has been linearly interpolated to faces:

$$\rho^{n+1} = \rho_0 + (\rho_1 - \rho_0)\,\gamma^{n+1} \tag{2.84}$$

$$\mu^{n+1} = \mu_0 + (\mu_1 - \mu_0)\,\gamma^{n+1}. \tag{2.85}$$

Navier-Stokes discretization

We first update the momentum to be consistent with the movement of mass that occurred due to the Cahn-Hilliard equation by:

$$\rho^{n+1}\mathbf{u}^* = (\rho\mathbf{u})^{BD} - \widehat{\Delta t}\nabla\cdot\left(\mathbf{m}\otimes\mathbf{u}^{AB}\right), \tag{2.86}$$

after which ρ^{n+1} is divided off to obtain $\mathbf{u}^*$. Next we apply explicit forces:

$$\begin{aligned}\mathbf{u}^{**} = \mathbf{u}^* + \widehat{\Delta t}\mathbf{g} + \frac{\widehat{\Delta t}}{\rho^{n+1}}\left(\sigma\kappa\nabla\left(g\left(\gamma^{n+1}\right)\right)\right) + \frac{\widehat{\Delta t}}{\rho^{n+1}}\nabla\cdot\left(\mu^{n+1}\left(\nabla\mathbf{u}^{AB}\right)^T\right) - \frac{\widehat{\Delta t}}{\rho^{n+1}}\nabla p^n \\ + \widehat{\Delta t}S_{\mathbf{u}}^{n+1}\end{aligned} \tag{2.87}$$

where

$$\kappa = -\nabla\cdot\left(\frac{\nabla\gamma}{||\nabla\gamma||}\right) \tag{2.88}$$

$$g(\gamma) = \begin{cases} 1, & \text{if } \gamma \geq 1-a \\ 0, & \text{if } \gamma < a \\ \frac{(-\gamma+a)^2(2\gamma+4a-3)}{(2a-1)^3}, & \text{otherwise} \end{cases} \tag{2.89}$$

We use $a = 0.2$ unless otherwise stated. We solve the viscosity equation for each component of $\mathbf{u}^v$ by solving a Helmholtz equation:

$$\mathbf{u}^v - \frac{\widehat{\Delta t}}{\rho^{n+1}}\nabla\cdot\left(\mu^{n+1}\nabla\mathbf{u}^v\right) = \mathbf{u}^{**}. \tag{2.90}$$

The pressure correction is obtained by solving the Poisson equation:

$$\nabla \cdot \left(\frac{\widehat{\Delta t}}{\rho^{n+1}} \nabla p' \right) = \nabla \cdot \mathbf{u}^v \tag{2.91}$$

$$p^{n+1} = p^n + p', \tag{2.92}$$

and the pressure correction is applied to obtain the final velocity:

$$\mathbf{u}^{n+1} = \mathbf{u}^v - \frac{\widehat{\Delta t}}{\rho^{n+1}} \nabla p'. \tag{2.93}$$

2.4 Numerical examples

All the units in the following tests are SI units.

2.4.1 Manufactured solution

In this test, we evaluate the accuracy of our discrete solvers using a manufactured solution for γ and $\mathbf{u}$. We choose the source terms to enforce the manufactured solution as

$$S_\gamma = \frac{\partial \gamma}{\partial t} + \nabla \cdot (\mathbf{u}\gamma) - \nabla \cdot (M \nabla \xi) \tag{2.94}$$

$$S_{\mathbf{u}} = \frac{\partial \rho \mathbf{u}}{\partial t} + \nabla \cdot (\mathbf{m} \otimes \mathbf{u}) + \nabla p - \rho g - \sigma \kappa \nabla g(\gamma) - \nabla \cdot \left(\mu \left(\nabla \mathbf{u} + (\nabla \mathbf{u})^T \right) \right). \tag{2.95}$$

We compute the error and its order at the end of the simulation to measure the accuracy of our method. We first assess the accuracy of the Cahn-Hilliard solver alone. We then incorporate the Navier-Stokes solve and evaluate the accuracy of the full method. Our parameters are chosen following [47]. In this section, we use a square domain $[-\pi, \pi]^2$. We

Table 2.1: Analysis of our Cahn-Hilliard solver at $t = 1$ demonstrates second order convergence.

	γ			
N	L_2		L_∞	
8	1.79e-05		2.96e-05	
16	4.40e-06	2.03	7.73e-06	1.93
32	1.23e-06	1.84	2.04e-06	1.92
64	3.03e-07	2.02	5.32e-07	1.94
128	7.65e-08	1.99	1.39e-07	1.93
256	1.98e-08	1.95	3.71e-08	1.91

set the density of the fluid phases to be $\rho_0 = 1$ and $\rho_1 = 3$, with viscosities $\mu_0 = 0.01$ and $\mu_1 = 0.02$. We use a time step of $\Delta t = 0.08/N$ and cell size $\Delta x = 2\pi/N$. We select the Cahn-Hilliard parameters M, σ, and η such that $M = 0.001$, $\lambda = 0.001$, and $\eta = 0.1$.

Cahn-Hilliard solver

We assess the convergence of our Cahn-Hilliard discretization using the manufactured solution

$$\gamma(x, y, t) = \frac{1}{2}\left(\cos(x)\cos(y) + 1\right)\sin(t). \tag{2.96}$$

To focus solely on the accuracy of the Cahn-Hilliard discretization, we exclude the Navier-Stokes update and set $u = v = 0$. We set the initial and boundary conditions using the manufactured solution. We measure the error in our simulation at $t = 1$. We determine the L_2 and L_∞ convergence by refining N from 8 to 256 with a constant $\frac{\Delta t}{\Delta x}$. The results are listed in Table 2.1 and show that our Cahn-Hilliard discretization is second order accurate.

Table 2.2: Analysis of our Cahn-Hilliard-Navier-Stokes solver at $t = 1$ demonstrates second order convergence.

	γ				u				v				p			
N	L_2		L_∞		L_2		L_∞		L_2		L_∞		L_2		L_∞	
8	1.86e-02		3.24e-02		6.88e-02		1.69e-01		1.40e-02		3.60e-02		1.60e-02		4.38e-02	
16	3.33e-03	2.48	1.20e-02	1.44	1.42e-02	2.28	4.12e-02	2.04	3.17e-03	2.14	9.93e-03	1.86	3.45e-03	2.21	1.31e-02	1.74
32	5.74e-04	2.54	2.43e-03	2.30	3.40e-03	2.06	1.01e-02	2.04	7.43e-04	2.09	3.05e-03	1.70	7.92e-04	2.12	3.64e-03	1.85
64	1.10e-04	2.38	2.80e-04	3.12	8.53e-04	1.99	2.54e-03	1.98	1.83e-04	2.02	7.22e-04	2.08	1.89e-04	2.07	6.32e-04	2.52
128	2.75e-05	2.00	7.30e-05	1.94	2.16e-04	1.98	6.14e-04	2.05	4.60e-05	1.99	1.83e-04	1.98	4.85e-05	1.96	1.39e-04	2.19
256	6.85e-06	2.01	1.90e-05	1.94	5.62e-05	1.94	1.40e-04	2.13	1.25e-05	1.88	4.80e-05	1.93	1.35e-05	1.84	3.76e-05	1.89

Cahn-Hilliard-Navier-Stokes solver

We evaluate the convergence of our full method employing both the Cahn-Hilliard and Navier-Stokes solves. For this purpose, we utilize the following manufactured solutions for γ, $\mathbf{u}$, and p, which we have adapted from the corresponding solution in [47]:

$$\gamma(x, y, t) = \frac{1}{2}\left(\cos(x)\cos(y) + 1\right)\sin(t) \tag{2.97}$$

$$u(x, y, t) = \sin(x)\cos(y)\cos(t) \tag{2.98}$$

$$v(x, y, t) = -\cos(x)\sin(y)\cos(t) \tag{2.99}$$

$$p(x, y, t) = \cos(x)\cos(y)\sin(t) \tag{2.100}$$

Note that these continuous solutions maintain a divergence-free velocity field, $\nabla \cdot \mathbf{u} = 0$. Additionally, gravity is $g = (1, -2)$. We set the initial and boundary conditions using the manufactured solution. We measure the error for γ, $\mathbf{u}$, and p at $t = 1$. We determine the L_2 and L_∞ convergence by refining N from 8 to 256 with a constant $\frac{\Delta t}{\Delta x}$. As shown in Table 2.2, our method exhibits second-order accuracy in γ, $\mathbf{u}$, and p.

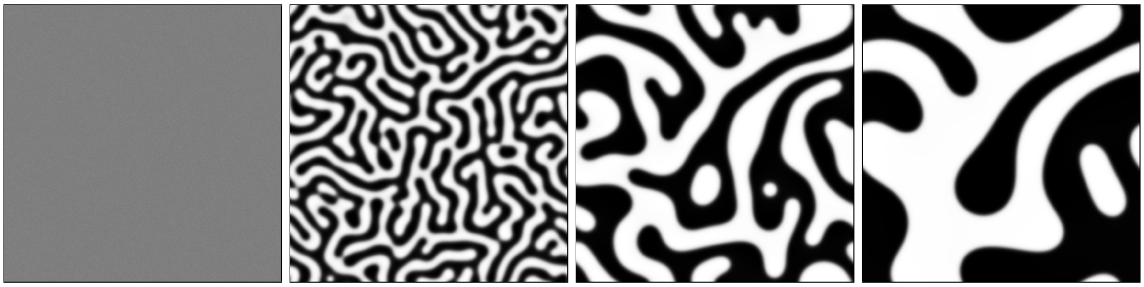

(a) $t = 0$ (b) $t = 0.1$ (c) $t = 1$ (d) $t = 5$

Figure 2.5: Binary fluid separation over time

2.4.2 Binary separation of phases

In this test, we demonstrate the evolution of the fluid phase separation over time with $\mathbf{u} = 0$ and $S_\gamma = 0$ using a random initial distribution for γ. We use the same setup as in [43]. In the following tests, we use a square domain $[0, 2\pi]^2$ that is periodic in all directions. γ is randomly distributed uniformly in the range $[0.475, 0.575]$. We use a time step of $\Delta t = 0.0001$ and cell size $\Delta x = 1/512$, and we run the test to $t = 5$. We select the Cahn-Hilliard parameters M, σ, and η such that $ML = \eta^2$, $\sigma = 1$, and $\eta^2 = 0.001$.

Figure 2.5 shows the increasing phase separation from $t = 0$ to $t = 5$. Our results are qualitatively similar to the results depicted in [43].

2.4.3 Stationary circle

We simulate a stationary drop with zero initial velocity and pressure using the same parameters as [47]. In an ideal system, the pressure and surface tension forces balance, and therefore the drop should maintain its shape and remain stationary. Discretely solving the system introduces spurious currents, leading to deformation. This test quantifies these currents and observes the impact of altering the resolution, density ratio, viscosity, and

surface tension. The test is carried out in a $[0,1]^2$ domain and time step of $\Delta t = 0.064/N$ and cell size $\Delta x = 1/N$. All walls are modeled with free-slip boundary conditions. The simulation runs until $t = 10$.

The initial configuration features a drop with initial radius of $r = 0.2$, centered at $(0.5, 0.5)$. The drop, designated as fluid 1, has a density of $\rho_1 = 1000$ and a viscosity that varies according to test case. The density and viscosity of the fluid surrounding the drop vary in each case. The specific values are detailed in Table 2.3 for density, viscosity and surface tension. Cases 2 and 4 investigate the effect of viscosity, while case 3 examines the impact of viscosity with a larger density ratio. Lastly, case 5 investigates the effects of surface tension.

We set $\eta = \eta_0(\Delta x/h_0)^{X^\eta} = \eta_0(Nh_0)^{-X^\eta}$ and $M = M_0(\eta/\eta_0)^{X^M} = \frac{M_0}{Nh_0}$ where $\eta_0 = h_0 = 1/32$, $M_0 = 10^{-5}$, $X^\eta = 2/3$ and $X^M = 3/2$. We refine N from 16 to 256 and compute the L_2 and L_∞ errors by comparing the magnitude of velocity $||\mathbf{u}||_2$ averaged to each cell center with zero.

The effect of changing the resolution in each case is illustrated in Figure 2.6. We observe that refinement increases the stability of the drop. The improvement in each case is between first and second order. Note that we choose a larger value for M than what was used in [47] since we observed their M to be insufficient to maintain a steady interface using our method.

Table 2.3: Material settings for different cases of the stationary circle test.

Case ID	ρ_0	ρ_1	μ_0	μ_1	σ
Case 1	1000	1000	0	0	1
Case 2	1000	1000	0.1	0.1	1
Case 3	1	1000	0.1	0.1	1
Case 4	1000	1000	0.0001	0.1	1
Case 5	1000	1000	0.1	0.1	10

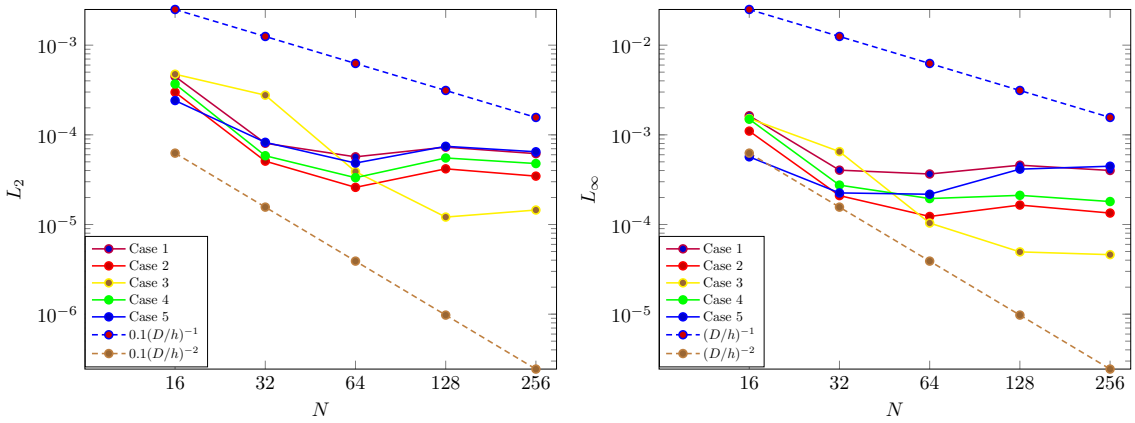

(a) L_2 error

(b) L_∞ error

Figure 2.6: L_2 and L_∞ errors of velocity in the stationary circle test.

2.4.4 Horizontal shear

The purpose of this test is to assess the conservation of mass, momentum, and kinetic energy within our method. We evaluate several scenarios with different densities and viscosities in the absence of external forces. We replicate the test outlined in [47]. The domain is $[0, 1]^2$, with periodic boundary conditions on all sides. The cell size is $\Delta x = 1/128$.

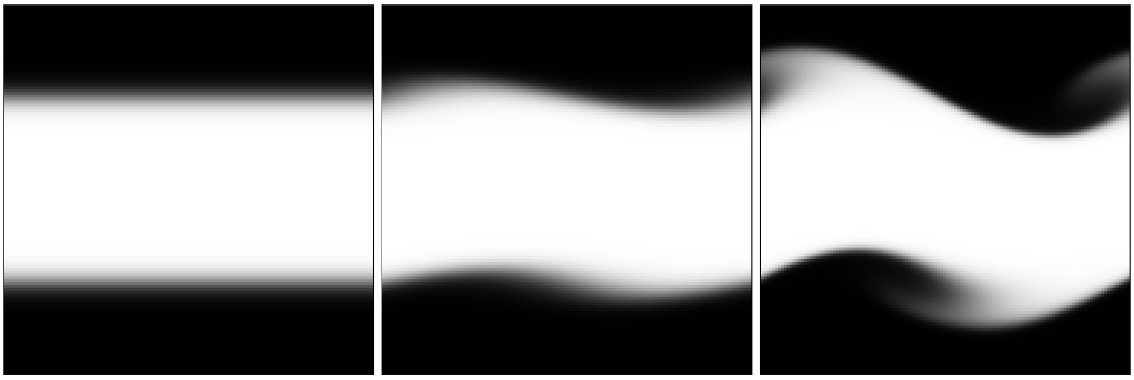

(a) $t = 0$ (b) $t = 0.5$ (c) $t = 1$

Figure 2.7: Horizontal Shear (Case 3).

The initial velocity and γ are given by

$$u(x, y, 0) = \begin{cases} \tanh\left(\frac{y-y_1}{\delta_1}\right), & \text{if } y \leq y_0 \\ \tanh\left(\frac{y_2-y}{\delta_1}\right), & \text{if } y > y_0 \end{cases} \tag{2.101}$$

$$v(x, y, 0) = \delta_2 \sin(kx) \tag{2.102}$$

$$\gamma(x, y, 0) = \begin{cases} \frac{1}{2}\left(1 + \tanh\left(\frac{y-y_1}{\delta_1}\right)\right), & \text{if } y \leq y_0 \\ \frac{1}{2}\left(1 + \tanh\left(\frac{y_2-y}{\delta_1}\right)\right), & \text{if } y > y_0 \end{cases} \tag{2.103}$$

with $y_0 = 0.5, y_1 = 0.25, y_2 = 0.75, \delta_1 = 1/30, \delta_2 = 0.5$ and $k = 2\pi$. As shown in Figure 2.7, fluid 1 is initialized in a band at the center of the domain with a velocity with positive x component, and fluid 0 is initialized elsewhere with a velocity with negative x component, leading to a strong velocity gradient at the interface. We test four different cases, as described in Table 2.4. In all cases, the surface tension is set to $\sigma = 10^{-12}$. We vary density

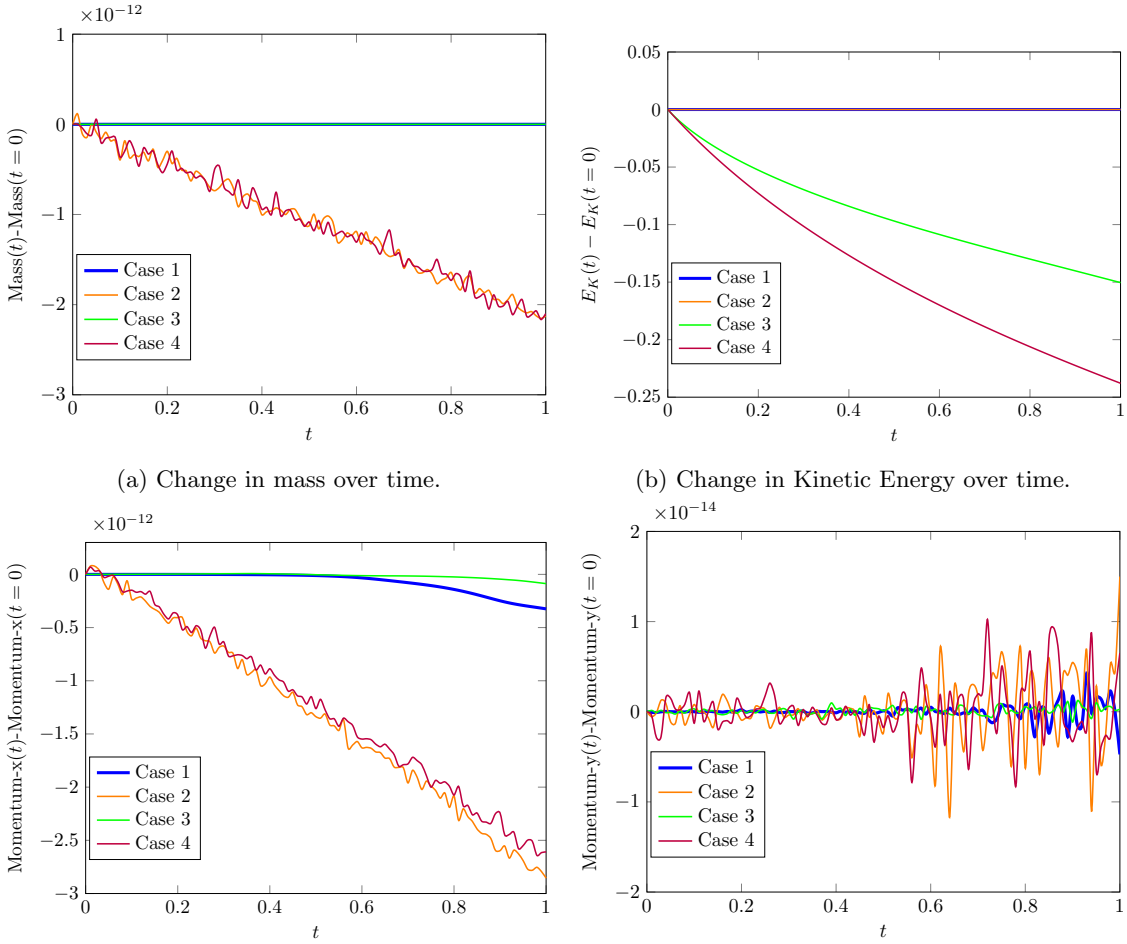

(a) Change in mass over time.

(b) Change in Kinetic Energy over time.

(c) Change in momentum (x axis).

(d) Change in momentum (y axis).

Figure 2.8: Results of the horizontal shear test for Cases 1-4.

and viscosity across the four cases. The time step is $\Delta t = 0.0005$ and the simulation ends at $t = 1$. We set $\eta = \delta_1/\sqrt{2}$ and $M = 10^{-7}$.

Table 2.4: Material settings for different cases of the horizontal shear.

Case ID	ρ_0	ρ_1	μ_0	μ_1
Case 1	1	1	0	0
Case 2	1	10	0	0
Case 3	1	1	0.001	0.01
Case 4	1	10	0.001	0.01

Mass and momentum should be conserved in all four cases investigated. Since surface tension is negligible, kinetic energy should be conserved in inviscid cases and gradually decline in viscous cases. We calculate the total mass, momentum and kinetic energy as

$$m_{\text{total}} = \sum_{i,j} \left(\rho_0 + (\rho_1 - \rho_0)\,\gamma_{i,j}\right) \Delta\Omega \tag{2.104}$$

$$(m\mathbf{u})^x_{\text{total}} = \sum_{i,j} \left(\rho_{i-1/2,j}\right) \left(u_{i-1/2,j}\right) \Delta\Omega \tag{2.105}$$

$$E_k = \frac{1}{2} \sum_{i,j} \left(\left(\rho_{i-1/2,j}\right) \left(u_{i-1/2,j}\right)^2 + \left(\rho_{i,j-1/2}\right) \left(v_{i,j-1/2}\right)^2 \right) \Delta\Omega, \tag{2.106}$$

where $\Delta\Omega = \Delta x \Delta y$ is the cell volume, and $(m\mathbf{u})^y_{\text{total}}$ is computed analogously.

The results of the tests are presented in Figure 2.8. Cases 1 and 3 exhibits zero mass change, while cases 2 and 4 have small decline with a magnitude of 10^{-12}. As expected, the inviscid cases maintain constant kinetic energy, while cases 3 and 4, with viscosity, show a gradual decline. Because our velocities are stored on faces instead of cell centers, we compute our kinetic energy differently from [47], but we observe similar results. We observe almost no change in momentum for cases without viscosity, and we see a minor change in viscous cases.

Shearing artifacts with large gradients

We observe some artifacts at the interface at the tested resolutions for inviscid cases 1 and 2, as illustrated in Figure 2.9. Increasing the resolution from 128 to 512 demonstrates that the artifacts go away under refinement. The artifact is caused by consistent advection in the presence of sharp γ gradients and shearing flow. The artifact is not present if

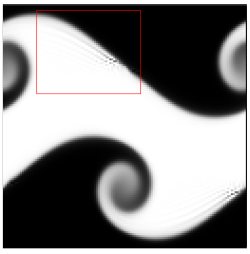

(a) One of the regions where artifacts can be seen in Case 1.

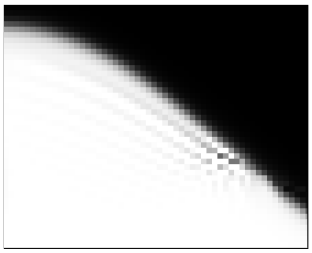

(b) A closer look at that region (a).

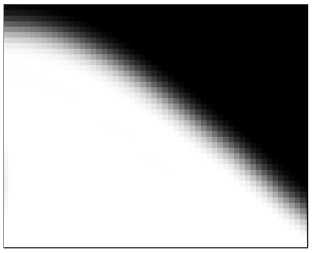

(c) The same region (a) if Case 1 is repeated with Cahn-Hilliard parameters $M = 10^{-5}$ and $\sigma = 1$ (no surface tension forces are applied in this example).

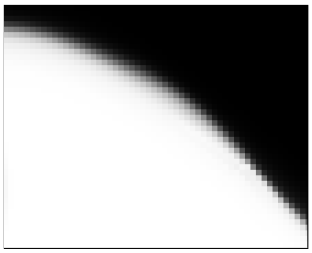

(d) The same region (a) if Case 1 is repeated using WENO advection for momentum advection.

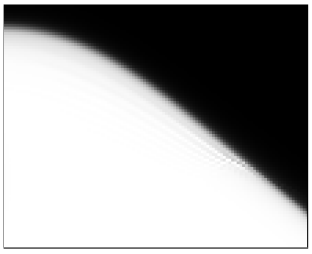

(e) The same region (a) if Case 1 is repeated with $N = 256$.

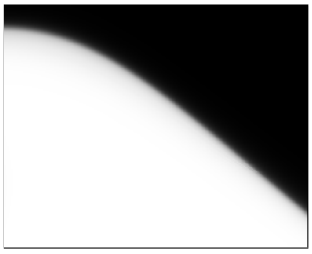

(f) The same region (a) if Case 1 is repeated with $N = 512$.

Figure 2.9: Artifacts in horizontal shear Case 1, and the effects of different parameters and methods on those artifacts.

WENO advection is used for momentum advection, however that scheme fails to preserve numerical consistency of mass and momentum. Strengthening the effects of Cahn-Hilliard also eliminates the artifact. It is unknown if these artifacts were also present in [47], as they only give bulk averaged measurements (which are consistent with ours), which do not reveal the artifacts we observed.

Table 2.5: Material settings for different cases of the translating circle test (surface tension, density).

Case ID	ρ_0	ρ_1	σ
Case 1	1	1	10^{-12}
Case 2	1	10^3	10^{-12}
Case 3	1	10^6	10^{-12}
Case 4	1	10^9	10^{-12}
Case 5	1	1	1
Case 6	1	10^3	1
Case 7	1	10^6	1
Case 8	1	10^9	1

2.4.5 Translating circle

This test examines the accuracy of advection in our method at different density ratios, based on the method used in [47]. We use a $[0,1]^2$ domain, with a cell size of $\Delta x = 1/128$ and the time step of $\Delta t = \Delta x/10$, with periodic boundary conditions in all axes. The initial configuration of the test comprises a circular drop of fluid 1 with a radius of $r = 0.1$ centered at $(0.5, 0.5)$. The initial velocity is $\langle 1, 1\rangle$ everywhere. The simulation ends at $t = 1$, when the drop is expected to return to the initial position. Fluid 1 is tested with varying densities of $\rho_1 = 1, 10^3, 10^6, 10^9$. The surrounding fluid 0 has density $\rho_0 = 1$. The viscosity of both fluids is zero. All density ratios are tested with surface tension values set to $\sigma = 1$ and $\sigma = 10^{-12}$. The test is carried out in the absence of external forces. We set $\eta = 3\Delta x$ and $M = 10^{-7}$. The material settings are summarized in Table 2.5.

In the ideal solution of the test, the drop returns to its initial location, preserving its original circular shape. The velocity remains constant throughout the simulation for all cases. Pressure maintains its initial value of zero in the absence of surface tension. However, in the presence of surface tension, a pressure jump should be observed around the surface of the bubble. A snapshot of velocity streamlines at the conclusion of the simulation is depicted

Table 2.6: Error results for the advection test without surface tension.

Variable	Norm	$\rho_1/\rho_0 = 1$	$\rho_1/\rho_0 = 10^3$	$\rho_1/\rho_0 = 10^6$	$\rho_1/\rho_0 = 10^9$
u	L_2	8.81e-13	2.60e-13	3.49e-11	6.07e-08
	L_∞	7.36e-12	1.87e-12	2.55e-10	1.69e-06
v	L_2	8.81e-13	2.60e-13	3.49e-11	6.06e-08
	L_∞	7.36e-12	1.88e-12	2.55e-10	1.57e-06

Table 2.7: Error results for the advection test with surface tension.

Variable	Norm	$\rho_1/\rho_0 = 1$	$\rho_1/\rho_0 = 10^3$	$\rho_1/\rho_0 = 10^6$	$\rho_1/\rho_0 = 10^9$
u	L_2	7.93e-04	2.25e-05	7.44e-07	8.47e-08
	L_∞	6.42e-03	1.50e-04	5.40e-06	1.16e-06
v	L_2	7.93e-04	2.25e-05	7.44e-07	8.47e-08
	L_∞	6.42e-03	1.50e-04	5.40e-06	1.27e-06

for cases without surface tension in Figure 2.10, and with surface tension in Figure 2.11 . The drop consistently preserves its shape until the end of the simulation, and velocities remain almost constant, aligning with their initial streamlines in both cases.

The L_2 and L_∞ errors for velocities are detailed in Tables 2.6 and 2.7 for cases without and with surface tension, respectively. The error is computed by comparing the final velocities with the initial value. We observe that our error is inversely correlated with the density ratio in cases without surface tension and they are consistent with the findings reported by Huang et al. [47], and the errors in the cases with surface tension are somewhat better than those reported in [47].

2.4.6 Rising air bubble

The primary objective of this experiment is to assess the convergence of our method toward the sharp interface solution within a real-world scenario characterized by a substan-

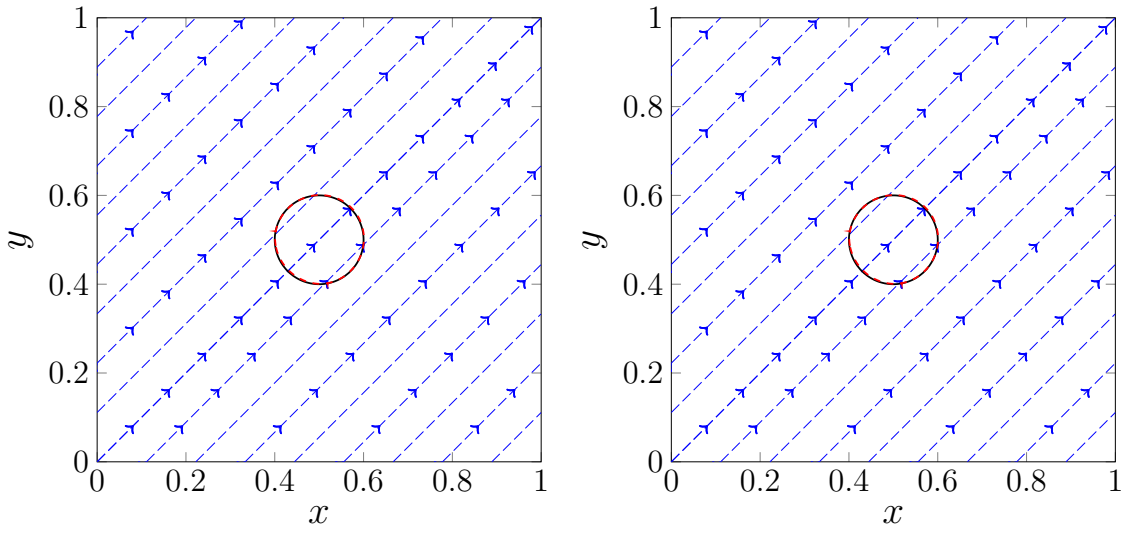

(a) $\rho_1/\rho_0 = 1$

(b) $\rho_1/\rho_0 = 10^3$

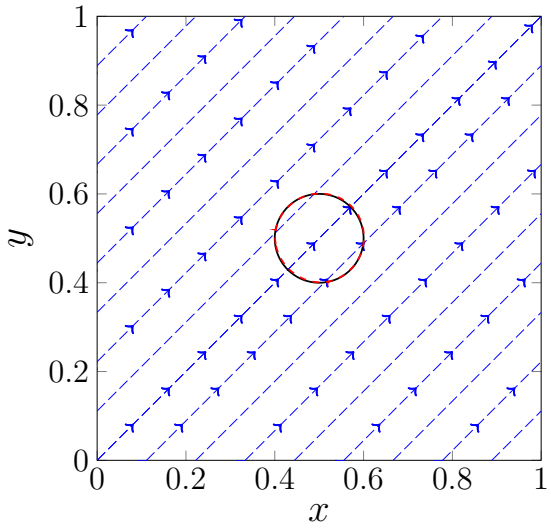

(c) $\rho_1/\rho_0 = 10^6$

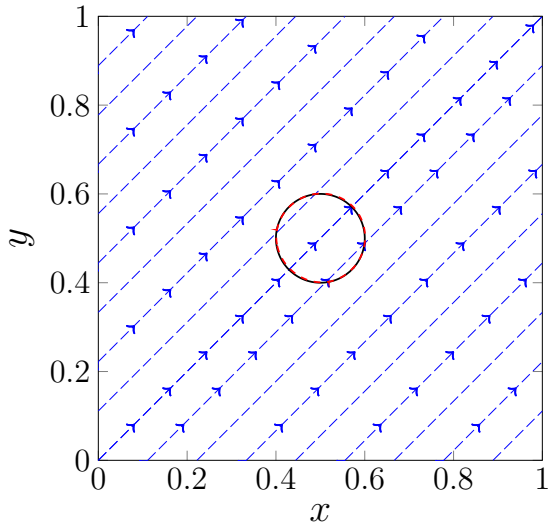

(d) $\rho_1/\rho_0 = 10^9$

Figure 2.10: Initial and final ($t = 1$) state of the drop with $\sigma = 10^{-12}$. The solid black line is the initial state and the dotted red line is the final state.

tial difference in density and viscosity. This evaluation holds particular significance because it examines the convergence toward the sharp interface solution by adjusting the parameter η while simultaneously modifying the resolution N. As suggested by the findings of Huang et al. [47], increasing the resolution while keeping η constant leads to the experiment's re-

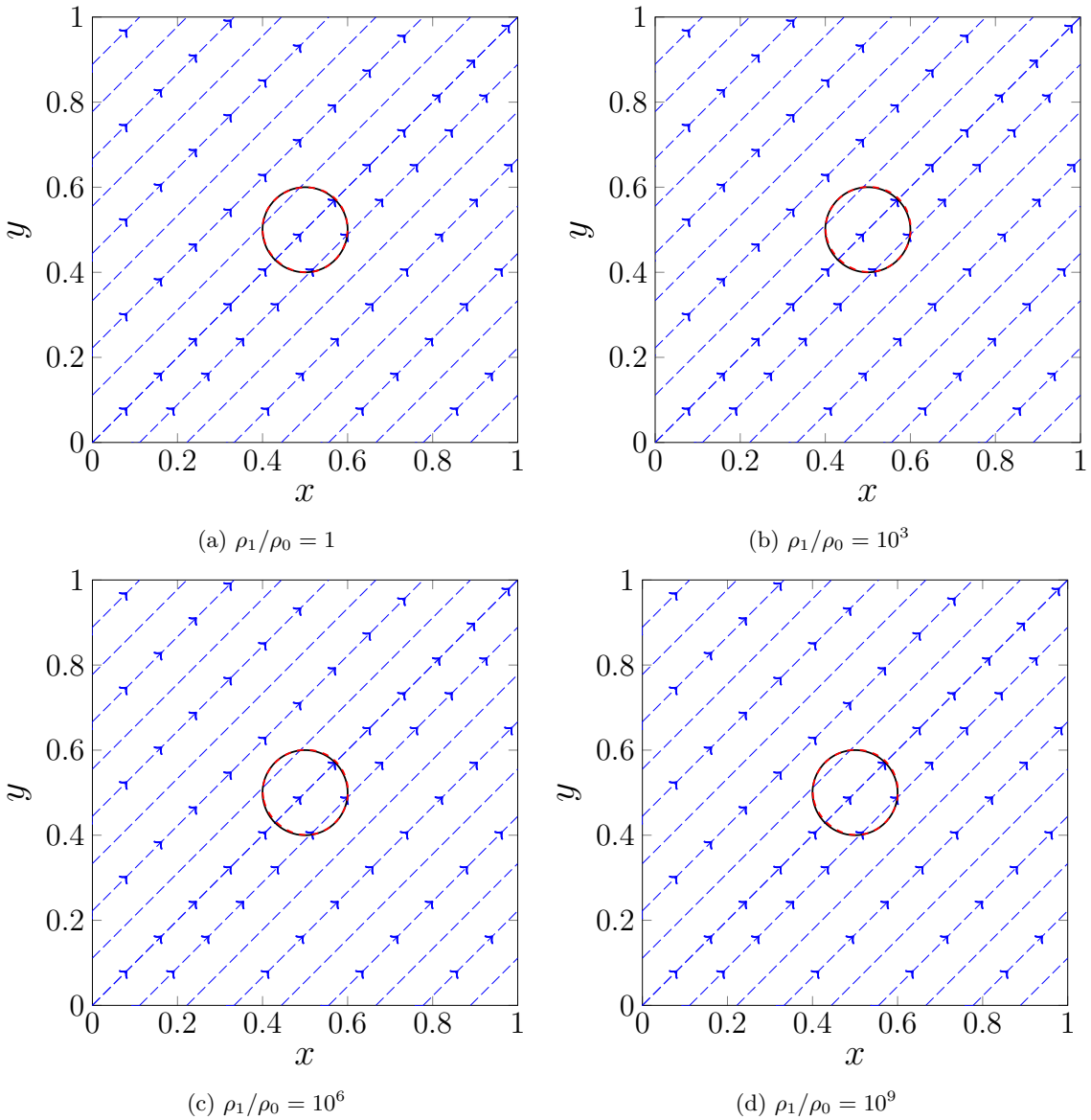

(a) $\rho_1/\rho_0 = 1$

(b) $\rho_1/\rho_0 = 10^3$

(c) $\rho_1/\rho_0 = 10^6$

(d) $\rho_1/\rho_0 = 10^9$

Figure 2.11: Initial and final ($t = 1$) state of the drop with $\sigma = 1$. The solid black line is the initial state and the dotted red line is the final state.

sults converging toward a solution with a transitional region of length $O(\eta)$. However, by decreasing η while simultaneously augmenting the resolution, we ensure the convergence toward the desired sharp interface solution.

We examine a $[0,1] \times [0,2]$ domain with cell size $\Delta x = 1/N$. The top and bottom walls exhibit a no-slip boundary condition, while the left and right walls follow a slip boundary condition. The initial setup involves a bubble with an initial diameter of 0.5 positioned at the center $(0.5, 0.5)$ and assigned a zero initial velocity. Fluid 0 within the bubble has properties $\rho_0 = 1$ and $\mu_0 = 0.1$, whereas the surrounding fluid 1 has $\rho_1 = 1000$ and $\mu_1 = 10$. This results in a density ratio of 1000 and a viscosity ratio of 100. Surface tension σ is 1.96, and gravity is $(0, -0.98)$. The time step size is $\Delta t = 0.128/N$ and the simulation stops at $t = 1$. We reduce the length of the transition region by setting $\eta = \eta_0 (N h_0)^{-X_\eta}$ where $\eta_0 = h_0 = 1/32$. $X_\eta \leq 1$ so that we have the same number of cells in the transition region (or more) as we refine [47]. We set the mobility variable $M = M_0 (\eta/\eta_0)^{X_M}$ where $M_0 = 10^{-7}$. Based on [49], X_M must be $1 \leq X_M < 2$.

We conduct six sets of tests and run each set with $N = 16, 32, 64, 128, 256$. In the first 5 sets of tests, we set $X_M = 1$ and $X_\eta = 0, \frac{1}{3}, \frac{1}{2}, \frac{2}{3}, 1$ to test the effects of X_η. In the last test, we set $X_M = \frac{3}{2}, X_\eta = \frac{2}{3}$ which makes $M \sim \Delta x$. To test the convergence of all test cases we compute the following three parameters:

$$\psi_c = \frac{P_a}{P_b} = \frac{2\sqrt{\int_{\gamma < \frac{1}{2}} \pi d\Omega}}{P_b} \tag{2.107}$$

$$y_c = \frac{\int_\Omega y(1-\gamma) d\Omega}{\int_\Omega (1-\gamma) d\Omega} \tag{2.108}$$

$$v_c = \frac{\int_\Omega v(1-\gamma) d\Omega}{\int_\Omega (1-\gamma) d\Omega}. \tag{2.109}$$

In (2.107), P_a is the perimeter of the circle with the same area as the bubble, P_b is the perimeter of the bubble and ψ_c is the circularity of the bubble. P_b is computed by discretiz-

	Grid	$X_\eta = 0, X_M = 1$		$X_\eta = \frac{1}{3}, X_M = 1$		$X_\eta = \frac{1}{2}, X_M = 1$		$X_\eta = \frac{2}{3}, X_M = 1$		$X_\eta = \frac{2}{3}, X_M = \frac{3}{2}$		$X_\eta = 1, X_M = 1$	
		L_2		L_2		L_2		L_2		L_2		L_2	
ψ_c	16	3.54e-03		7.60e-03		9.70e-03		1.22e-02		1.21e-02		1.88e-02	
	32	2.50e-03	0.51	1.85e-03	2.04	2.26e-03	2.10	2.46e-03	2.30	2.45e-03	2.31	2.61e-03	2.85
	64	1.06e-03	1.24	8.01e-04	1.21	8.01e-04	2.10	9.07e-04	1.44	9.36e-04	1.39	1.20e-03	1.12
	128	3.92e-04	1.44	3.00e-04	1.42	2.58e-04	1.63	4.47e-04	1.02	4.86e-04	0.95	6.94e-04	0.80
		L_2		L_2		L_2		L_2		L_2		L_2	
y_c	16	9.24e-03		1.50e-02		1.69e-02		1.88e-02		1.87e-02		2.36e-02	
	32	2.27e-03	2.03	6.23e-03	1.27	6.86e-03	1.30	7.12e-03	1.40	7.10e-03	1.40	7.17e-03	1.72
	64	4.61e-04	2.30	2.65e-03	1.23	2.68e-03	1.30	2.47e-03	1.53	2.45e-03	1.53	1.92e-03	1.90
	128	6.49e-05	2.83	9.49e-04	1.48	8.64e-04	1.63	7.05e-04	1.81	6.96e-04	1.82	4.26e-04	2.17
		L_2		L_2		L_2		L_2		L_2		L_2	
v_c	16	1.75e-02		2.42e-02		2.65e-02		2.89e-02		2.89e-02		3.53e-02	
	32	5.71e-03	1.62	1.00e-02	1.27	1.07e-02	1.31	1.10e-02	1.40	1.10e-02	1.40	1.10e-02	1.68
	64	1.68e-03	1.76	4.06e-03	1.30	4.05e-03	1.31	3.75e-03	1.55	3.76e-03	1.55	2.99e-03	1.88
	128	3.00e-04	2.49	1.36e-03	1.58	1.25e-03	1.70	1.06e-03	1.82	1.07e-03	1.81	6.83e-04	2.13

Table 2.8: L_2 error and order compared to $N = 256$ on all the cases for rising air bubble test.

ing the interface surface using a marching squares algorithm and computing the total length between successive nodes. $\psi_c = 1$ when the shape of the bubble is a circle and $\psi_c < 1$ when the bubble deforms [47]. y_c is center of mass and v_c is the velocity of center mass in the y direction (rising velocity).

In the case where $X_M = 1, X_\eta = 0$, we expect the simulation to converge to the exact solution of the phase-field model where $\eta = \eta_0$ since setting $X_\eta = 0$ results in using the same value for η in all of the simulations [47]. We show our results for this particular case in Figure 2.12. We observe that our results match the results shown in [47]. In the case where $X_\eta \neq 0$ we expect the simulation to converge to a sharp interface solution. We compare our results for each case where $N = 256$ in Figure 2.13. The error and convergence order of each case can be found in Table 2.8 where we compare all cases with $N = 16$ to $N = 128$ to the results from the simulation where $N = 256$. We observe second order convergence where $X_\eta = 0$ and maintain an order of about 1.5-2.0 on all other cases.

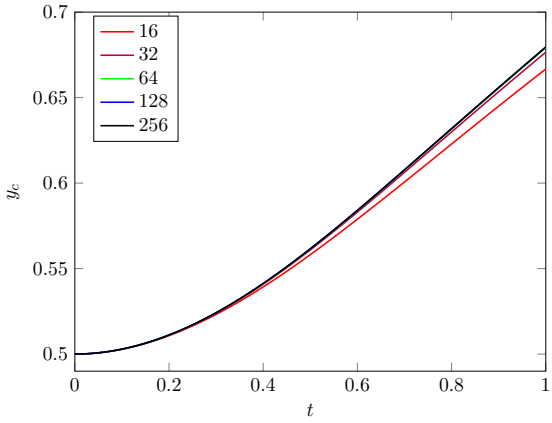

(a) Location of center of mass over time.

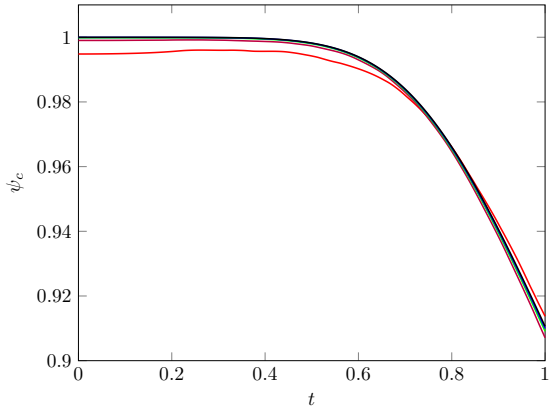

(b) Circularity of the bubble over time.

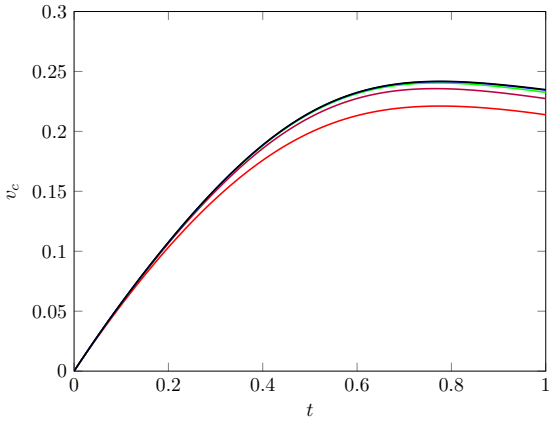

(c) Velocity of center of mass over time.

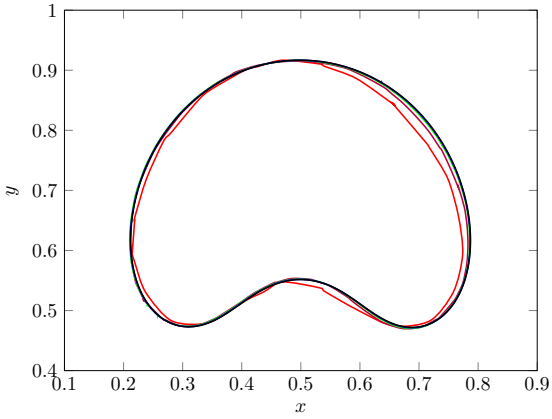

(d) Surface of the bubble at $t = 1$.

Figure 2.12: Rising bubble test results with $X_\eta = 0, X_M = 1$.

2.4.7 Comparisons of surface tension

The aim of this test is to compare different surface tension methods to determine how well they show expected properties. We measure the direction and location of surface tension in Section 2.4.7 and its effects on pressure in Section 2.4.7. We explore the impact of introducing $g(\gamma)$ as detailed in Section 2.3.2 and varying the parameter a in (2.47). The specific functions utilized in our comparative tests are outlined in Table 2.9. In cases 1 and 2 we use the surface tension used by Shen and Yang [72] and Huang et al. [47]

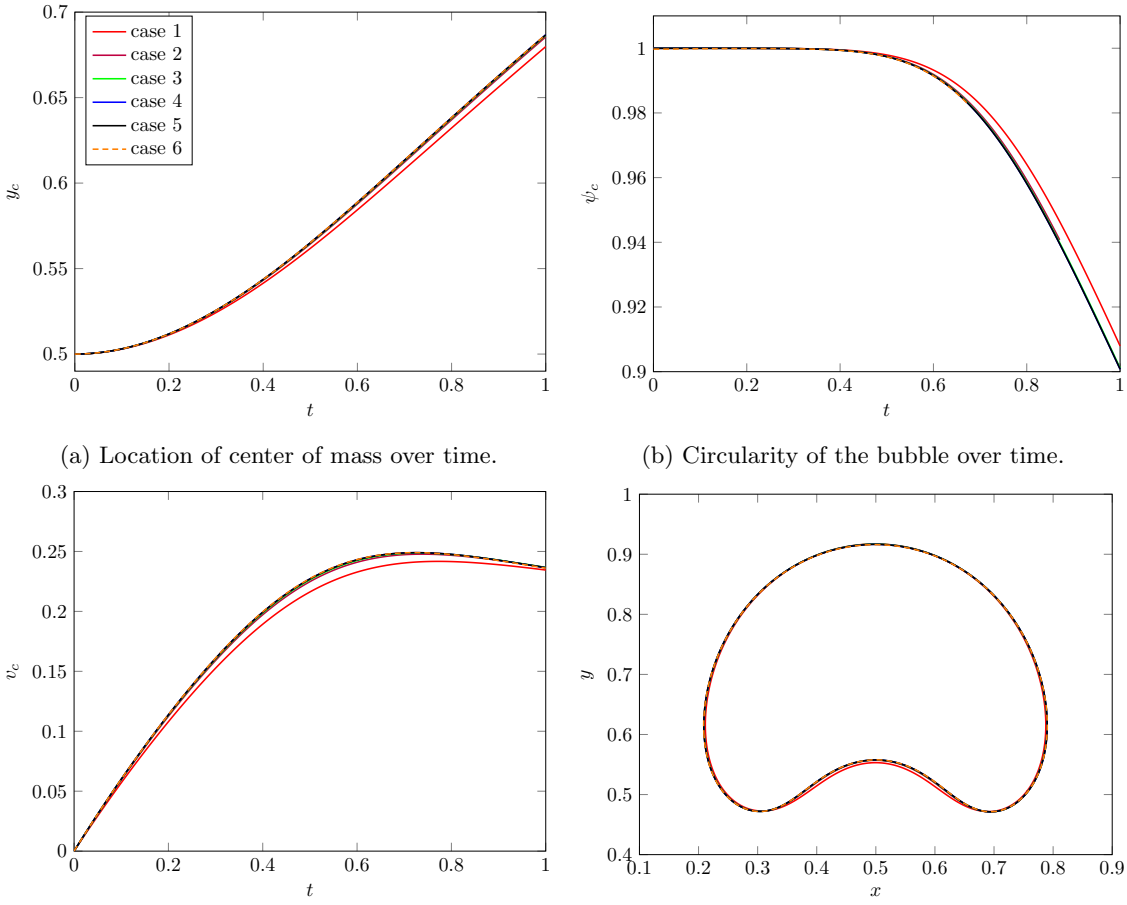

(a) Location of center of mass over time.

(b) Circularity of the bubble over time.

(c) Velocity of center of mass over time.

(d) Surface of the bubble at $t = 1$.

Figure 2.13: Rising bubble test results of test described in table 2.8 with $N = 256$.

respectively. Cases 3 to 7 we apply the function introduced in (2.47), varying the values of a as $a = 0, 0.1, 0.2, 0.3, 0.5$. In cases 8 and 9 we use the same scheme as cases 3 to 7 using a different functions as $g(\gamma)$. In all the tests described we set $\sigma = 1$.

We conduct the test in a $[0, 1]^2$ domain with a cell size of $\Delta x = 1/256$, where all the walls feature slip boundary conditions. We use $\Delta t = 0.00025$ and run the simulation until $t = 10$. The initial configuration features a bubble with an initial radius of $r = 0.2$, centered at $(0.5, 0.5)$, with zero initial velocity. The fluid inside the bubble and the surrounding fluid both have a density of $\rho_0 = \rho_1 = 1000$ and viscosity of $\mu_0 = \mu_1 = 0$.

Table 2.9: Material settings for different cases for the surface tension and pressure comparison test.

Case ID	Surface Tension	a
Case 1	$\lambda\nabla\cdot(\nabla\gamma\otimes\nabla\gamma)$	
Case 2	$4\xi\nabla\gamma$	
Case 3	$\sigma\kappa\nabla(g(\gamma))$	0
Case 4	$\sigma\kappa\nabla(g(\gamma))$	0.1
Case 5	$\sigma\kappa\nabla(g(\gamma))$	0.2
Case 6	$\sigma\kappa\nabla(g(\gamma))$	0.3
Case 7	$\sigma\kappa\nabla(g(\gamma))$	0.5
Case 8	$\sigma\kappa\nabla\left(\frac{1}{2}\left(1+\tanh(4\gamma-2)\right)\right)$	
Case 9	$\sigma\kappa\nabla\gamma$	

We define η and M similar to Section 2.4.6, with $M_0 = 10^{-5}$, $\eta_0 = h_0 = 1/8$, $X^\eta = 2/3$ and $X^M = 3/2$. This gives $\eta = 0.03125$ and $M = 1.25 \times 10^{-6}$, which we use for all cases.

Magnitude and angle

Visual representations of the test results are shown in Figures 2.14 and 2.15. The angle between the surface normal and the surface tension force is measured in radians. The contour $\gamma = 0.5$ representing the center of the interface is displayed as a dashed circle.

Notably, cases 1 and 2 show strong disagreement between the surface tension direction and normal just beyond the interface center, and case 1 shows negligible magnitude at the interface center. Cases 2, 3, 8, and 9 all show strong disagreement in the angle far from the interface, but the magnitude of the surface tension in those areas is negligible as expected.

Cases 3 through 7 show the effects of the a parameter in our surface tension method. We observe that, as expected, the areas where the surface tension magnitude is

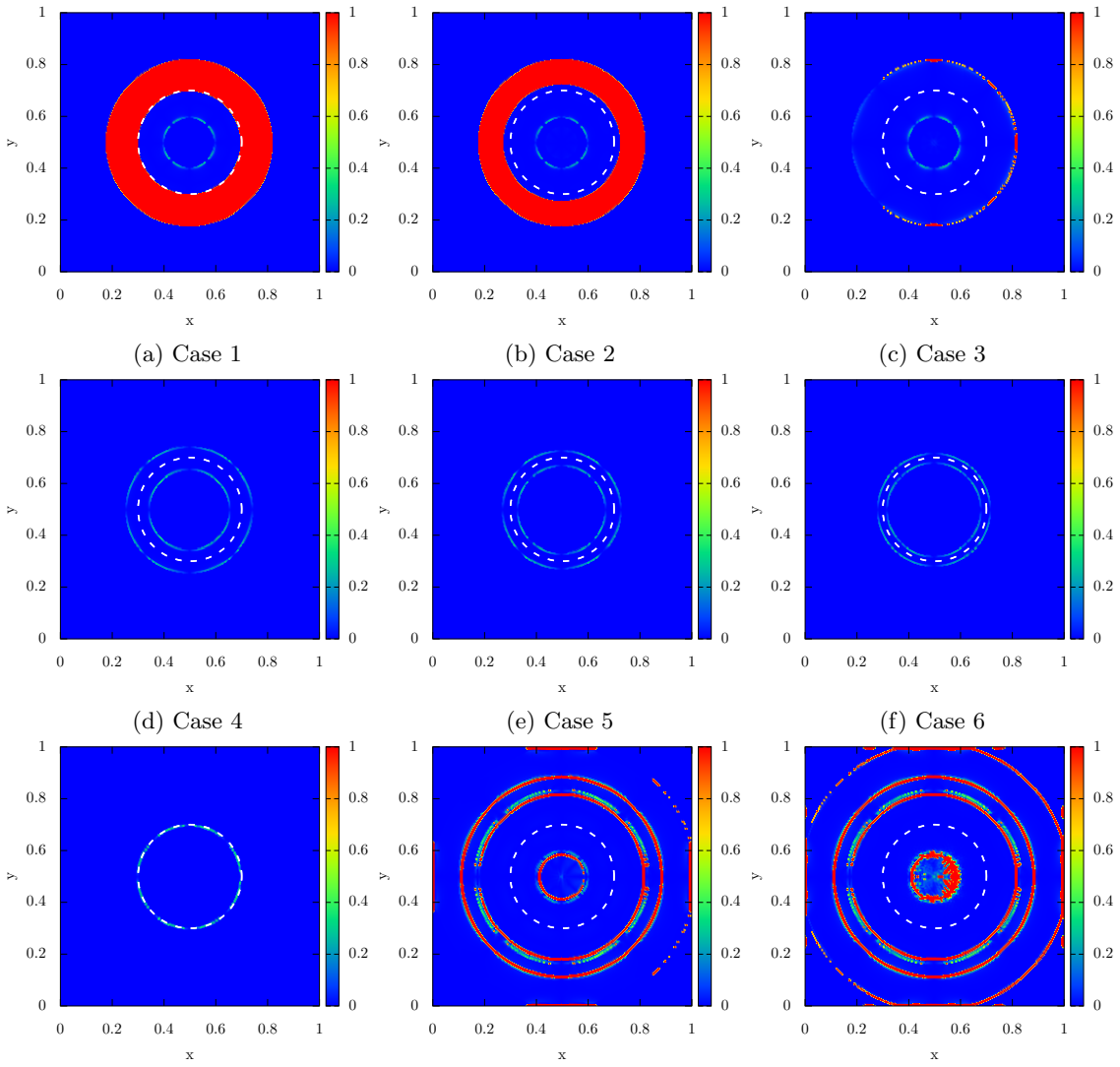

(a) Case 1 (b) Case 2 (c) Case 3

(d) Case 4 (e) Case 5 (f) Case 6

(g) Case 7 (h) Case 8 (i) Case 9

Figure 2.14: Comparisons of the angle between surface tension force and surface normal (radians) for different surface tension formulations.

nonzero begins to closely fit the interface center contour as a approaches 0.5. In the case where $a = 0.5$, the surface tension force closely matches the interface contour, as we would expect from a sharp interface solution. These cases also show the advantage of a finite support around the interface (in cases 4-7), which gives a surface tension force vector $\mathbf{0}$ away from the interface. In cases 3 (where $a = 0$), 8, and 9, we see that the surface tension

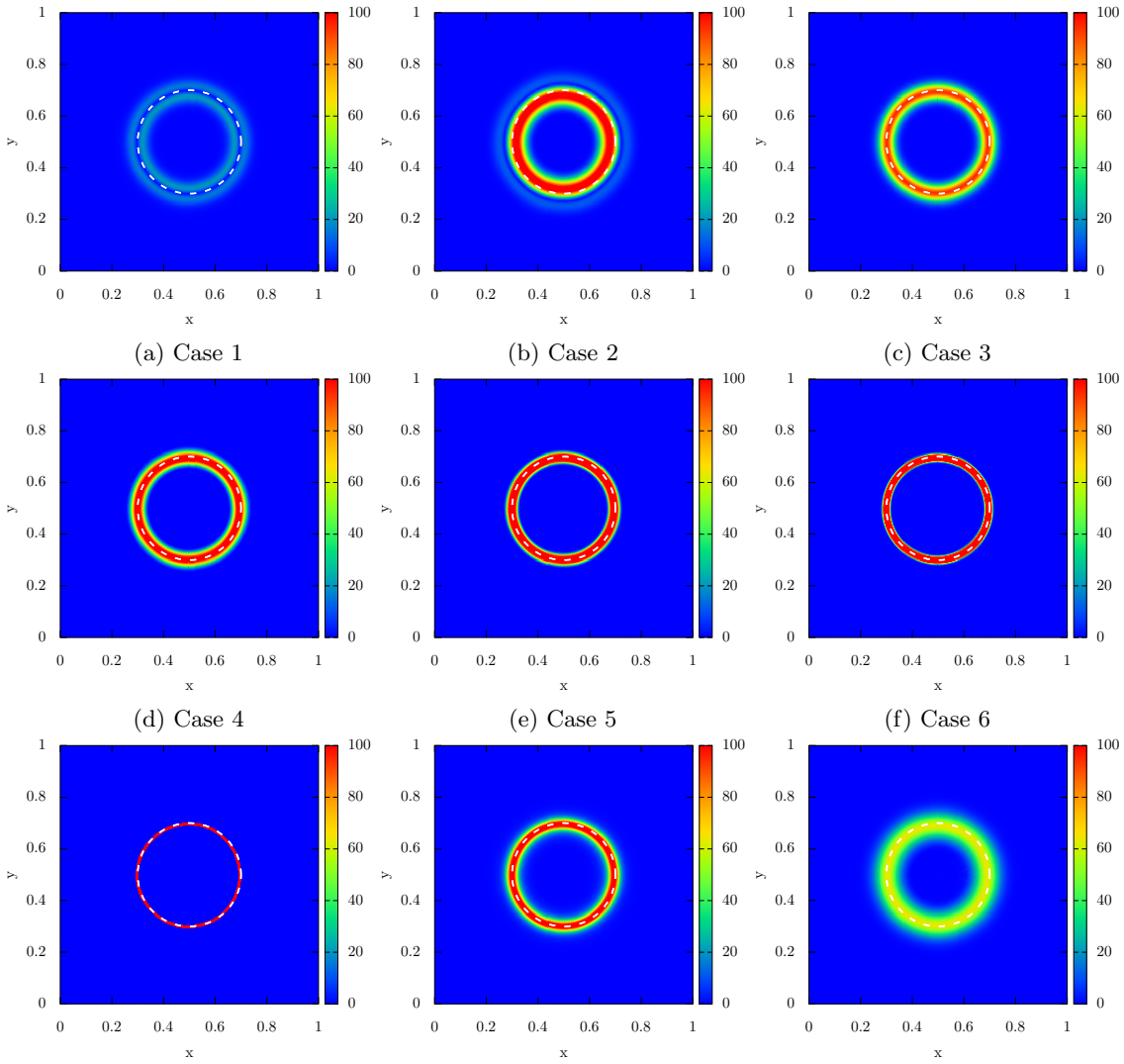

Figure 2.15: Comparisons of the magnitude of surface tension force for different surface tension formulations.

is still being calculated away from the interface. While the magnitudes are negligible in these areas, they are not 0.

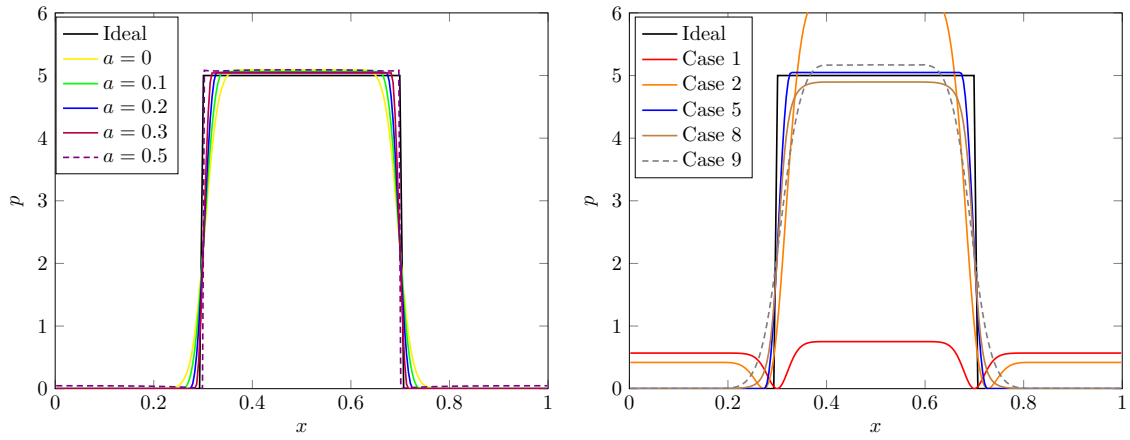

(a) Comparing pressure in cases using $\sigma\kappa\nabla g(\gamma)$ for surface tension.

(b) Comparing pressure in the remaining cases with case 5 ($a = 0.2$).

Figure 2.16: Change in pressure in the x axis at $y = 0.5$ of Section 2.4.7.

Effects on pressure

Ideally, we anticipate the pressure to be a constant value inside and outside of the bubble with a pressure jump on the surface. We compare our results to the ideal physical pressure along the x-axis at $y = 0.5$ in Figure 2.16.

We show in Figure 2.16a that as a goes from 0 to 0.5, the results move toward the ideal pressure jump caused by a sharp interface. All parameters of a produce acceptable results for pressure, which makes $\sigma\kappa\nabla(g(\gamma))$ the best of the methods by this criteria. Figure 2.16b shows that cases 8 and 9, which are similar to our preferred method, are also reasonably close to the ideal pressure. Note that in Case 1, the formulation of the surface force introduces a gradient term which will be compensated for in the pressure correction; the plot for Case 1 shows the pseudo-pressure which includes the compensating term [75]. Case 2 deviates significantly from the ideal in our tests.

2.4.8 Rayleigh-Taylor instability

We simulate the classic Rayleigh-Taylor instability, where a denser fluid is initially positioned above a lighter one in the presence of gravitational force. This instability test serves as a benchmark for evaluating the behavior of two-phase flows. The tests was first investigated by Rayleigh [70] and is normally characterized by "Atwood ratio" $A_t = (\rho_1 - \rho_0)/(\rho_1 + \rho_0)$, a measure of the density difference between the two phases. Daly [19] conducted a numerical analysis of the test. Long-time instability analysis of the test for inviscid incompressible fluids without surface tension with $A_t = 0.5$ is done by Tryggvason [77]. We examine a $[0, 1] \times [0, 4]$ domain with cell sizes $\Delta x = 1/128$. Free-slip boundary conditions are enforced at the top and bottom walls, while the left and right walls are subject to periodic boundary conditions. The initial setup involves a heavier fluid with density $\rho_1 = 3, 30, 1000, 3000$ and viscosity $\mu_1 = 0.001$ positioned on top of a lighter fluid with density $\rho_0 = 1$ and viscosity $\mu_0 = 0.001$. The velocity is initialized to zero, and the initial interface between the two fluids is situated at $y = 2 + 0.1\cos(2\pi x)$. The specified parameters for the simulation include a surface tension $\sigma = 10^{-12}$, gravitational force vector $\langle 0, -1 \rangle$, and a time step size of $\Delta t = 5 \times 10^{-4}/\sqrt{A_t}$. The simulation concludes at $t\sqrt{A_t} = 8$. We set M so that $\lambda M = 10^{-15}$ and $\eta = 0.01$.

Snapshots of the test with $\rho_1 = 3$ are presented in Figure 2.17, offering a comparative analysis with the outcomes from our implementation of Huang et al. [47]'s method. Notably, our simulation closely aligns with the results obtained by Huang et al. [47]. Figure 2.18 provides a visual depiction of the Rayleigh-Taylor test's progression at a density ratio of 3, while Figure 2.19 showcases the evolution of simulations across various density

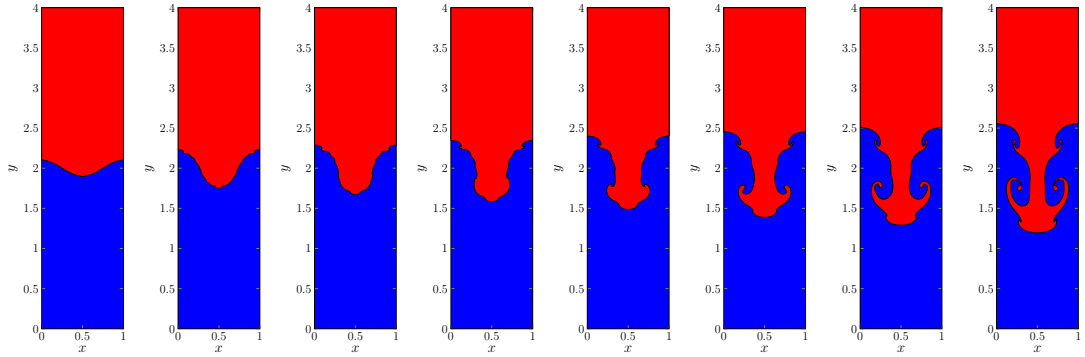

(a) Rayleigh-Taylor test results using Huang et al. [47]'s method.

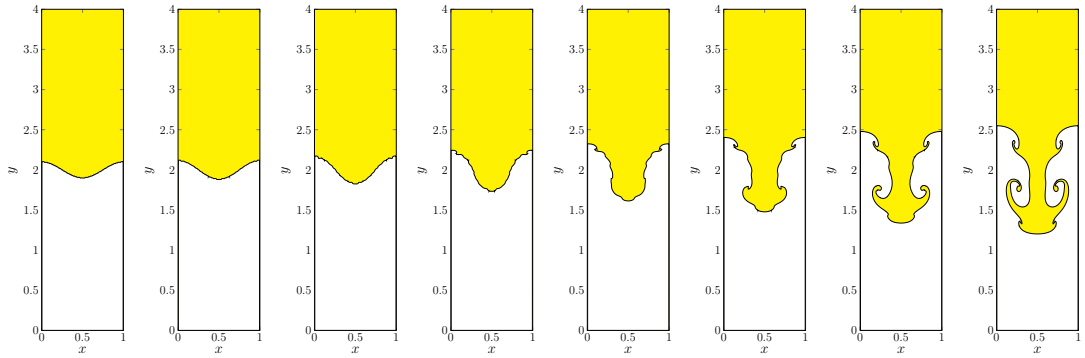

(b) Rayleigh-Taylor test results using our method.

Figure 2.17: Rayleigh-Taylor test at times $t = 0, 1, 1.25, 1.5, 1.75, 2, 2.25, 2.5$ and density ratio of 3.

ratios. In both Figure 2.18 and Figure 2.19, the simulations maintain symmetry throughout, even as the interface develops intricate shapes in later stages. As the density ratio increases, the simulation exhibits accelerated movement and a simpler evolution. Due to the minor impact of viscosity in these simulations, a stable state is not reached before the simulations conclude at $t\sqrt{A_t} = 8$.

In Figure 2.20 we plot a quantitative measurement of the test by measuring the highest and lowest point of the interface between the two fluids with density ratio of 3 from

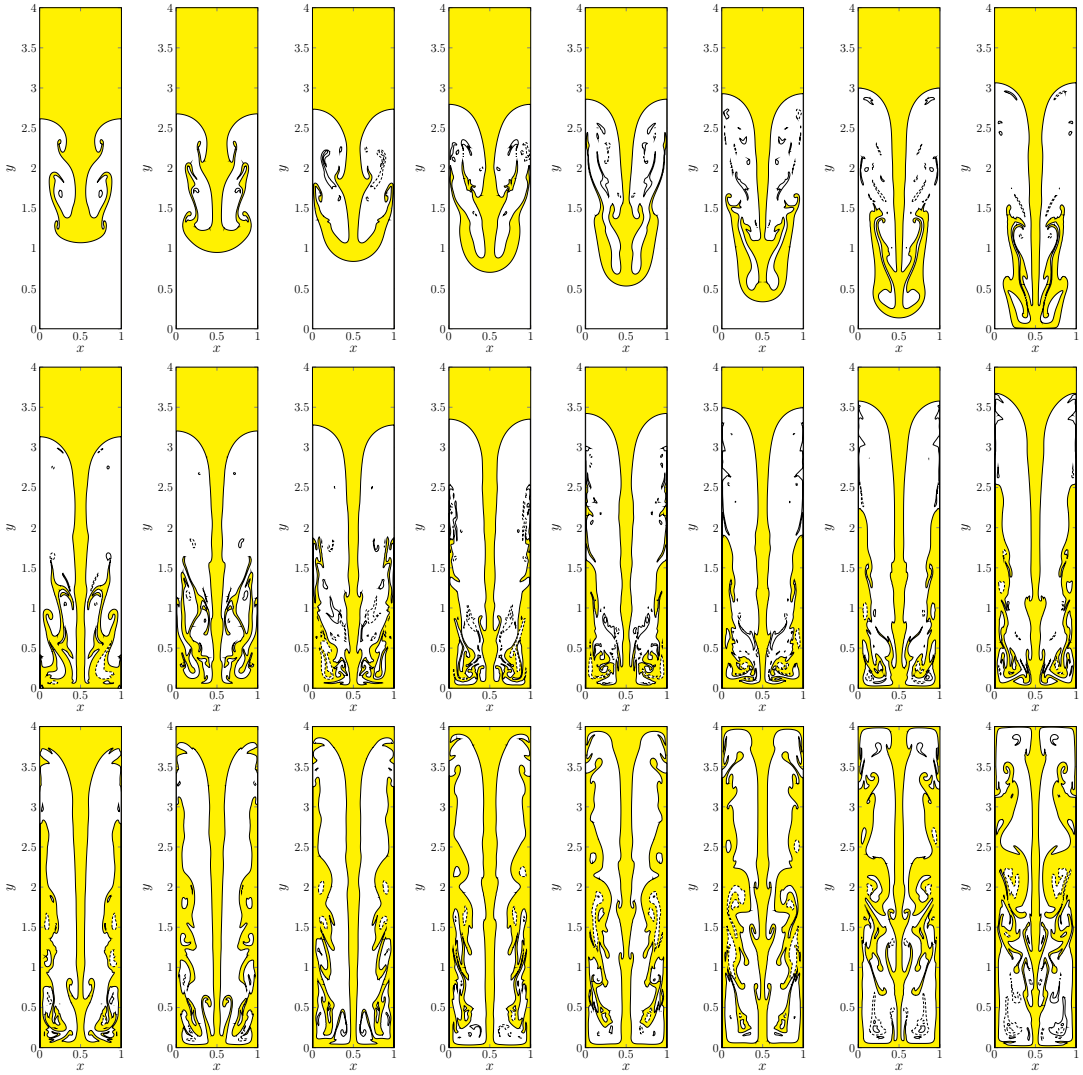

Figure 2.18: Rayleigh-Taylor test results with $\rho_0 = 3$, from $t = 2.25$ to $t = 8$ in 0.25 increments.

$t = 0$ to $t = 2.5$. Our results are comparable to the results reported by Huang et al. [47], [21] and Guermond and Quartapelle [35] which use similar values for density and viscosity.

2.4.9 Dam break

The dam break test is employed to assess the method's performance in scenarios characterized by high density ratios. In this test, we simulate the classic test as in Martin

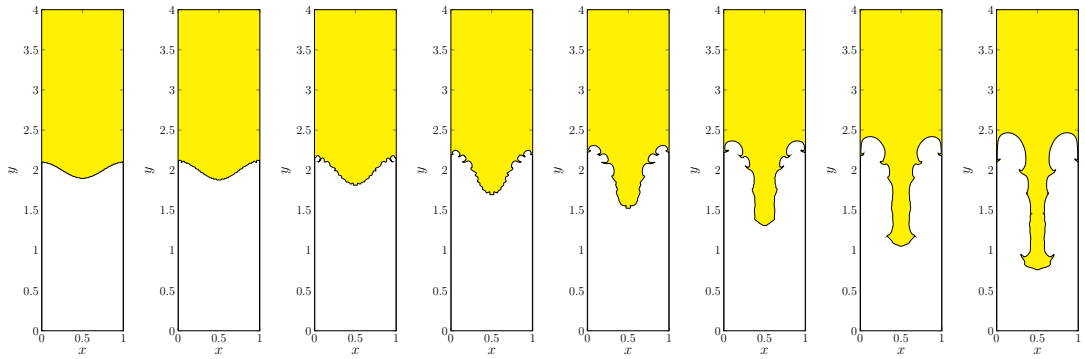

(a) $\rho_1 = 30$

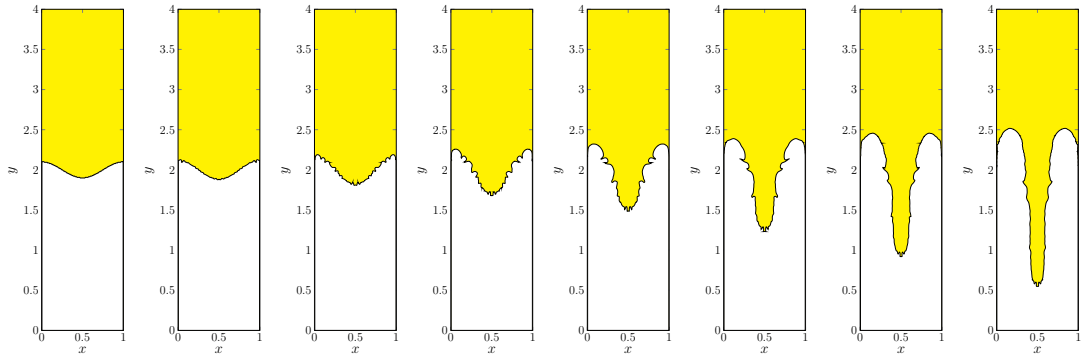

(b) $\rho_1 = 1000$

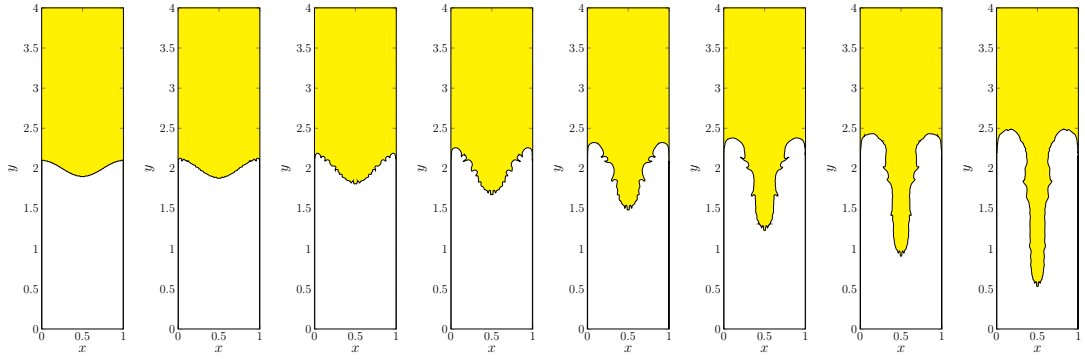

(c) $\rho_1 = 3000$

Figure 2.19: Rayleigh-Taylor simulation with density ratio of 30, 1000 and 3000 at times $t = 0, 0.25, 0.5, 0.75, 1, 1.25, 1.5, 1.75$.

and Moyce [65] where a specific volume of water is confined within a rectangular box of dimensions $[a \times a]$, enclosed by walls on both the left and right sides. In the initial frame, the right wall of the box containing the water, is removed, leading to the observation of the gravitational evolution of water movement within a larger $[0, 4a] \times [0, 2a]$ domain. We

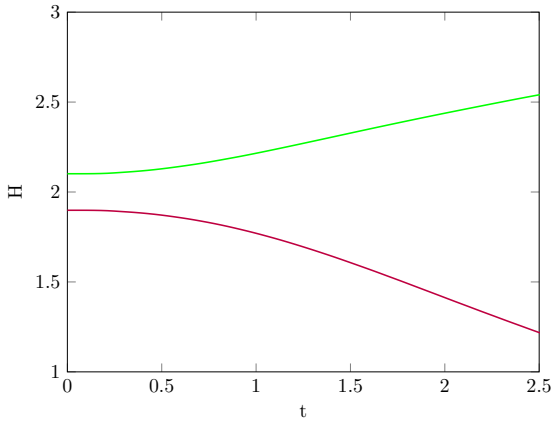

Figure 2.20: Location of the maximum and minimum x of the interface in the Rayleigh-Taylor test with density ratio of 3.

examine this domain with cell sizes $\Delta x = a/64$ where $a = 0.05715$. The all the walls are subject to a no-slip boundary condition. The initial setup involves a heavier fluid (water) with density $\rho_0 = 998.207$ and viscosity $\mu_0 = 1.002 \times 10^{-3}$ confined in a $[a \times a]$ box surrounded by a lighter fluid (air) with density $\rho_1 = 1.204$ and viscosity $\mu_1 = 1.78 \times 10^{-5}$ with initial velocity of zero. The specified parameters for the simulation include a surface tension $\sigma = 7.28 \times 10^{-2}$, gravitational force vector $\langle 0, -9.8 \rangle$, and a time step size of $\Delta t = 7.1437 \times 10^{-5}$. The simulation concludes at $t = 10$. We set M so that $\lambda M = 10^{-7}$ and $\eta = 0.01a$.

As previously noted, the simulation begins with zero velocity, and at time $t = 0$, removing the box containing the denser fluid instigates fluid motion due to gravity. As the simulation progresses, the denser fluid reaches the right wall of the domain, where it is pushed to rise along the wall before crashing back down. The simulation attains a stable condition by the conclusion of the simulation. Visual snapshots of distinct stages within the simulation are shown in Figures 2.22 and 2.23. We non-dimensionalize t by dividing it

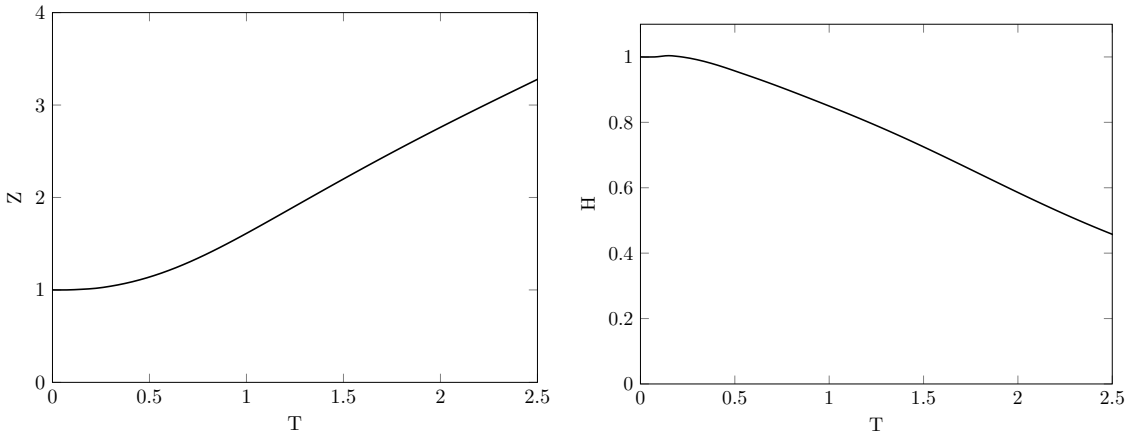

(a) Location of the front of fluid phase 1.

(b) Location of the height of fluid phase 1.

Figure 2.21: Fluid height and front over time in the dam break test.

by $\sqrt{\frac{a}{|g_y|}}$ so that $T = t/\sqrt{\frac{a}{|g_y|}}$. We do the same for length as well by diving it by a. We measure our results quantitatively by computing the front of the interface and the highest point of the interface from $T = 0$ to $T = 2.5$ in Figure 2.21. Our results are comparable to those reported by Huang et al. [47] and Martin and Moyce [65].

2.5 Conclusion

In this chapter we constructed a novel, simple, and highly stable discretization of the Cahn-Hilliard equation. We coupled this to the Navier-Stokes equations to simulate phase separation in a two-phase fluid flow in two dimensions. We demonstrate that the resulting scheme is second order accurate in γ and velocity and compare it with published results on a number of tests. The scheme is mass-momentum consistent and works with large density ratios.

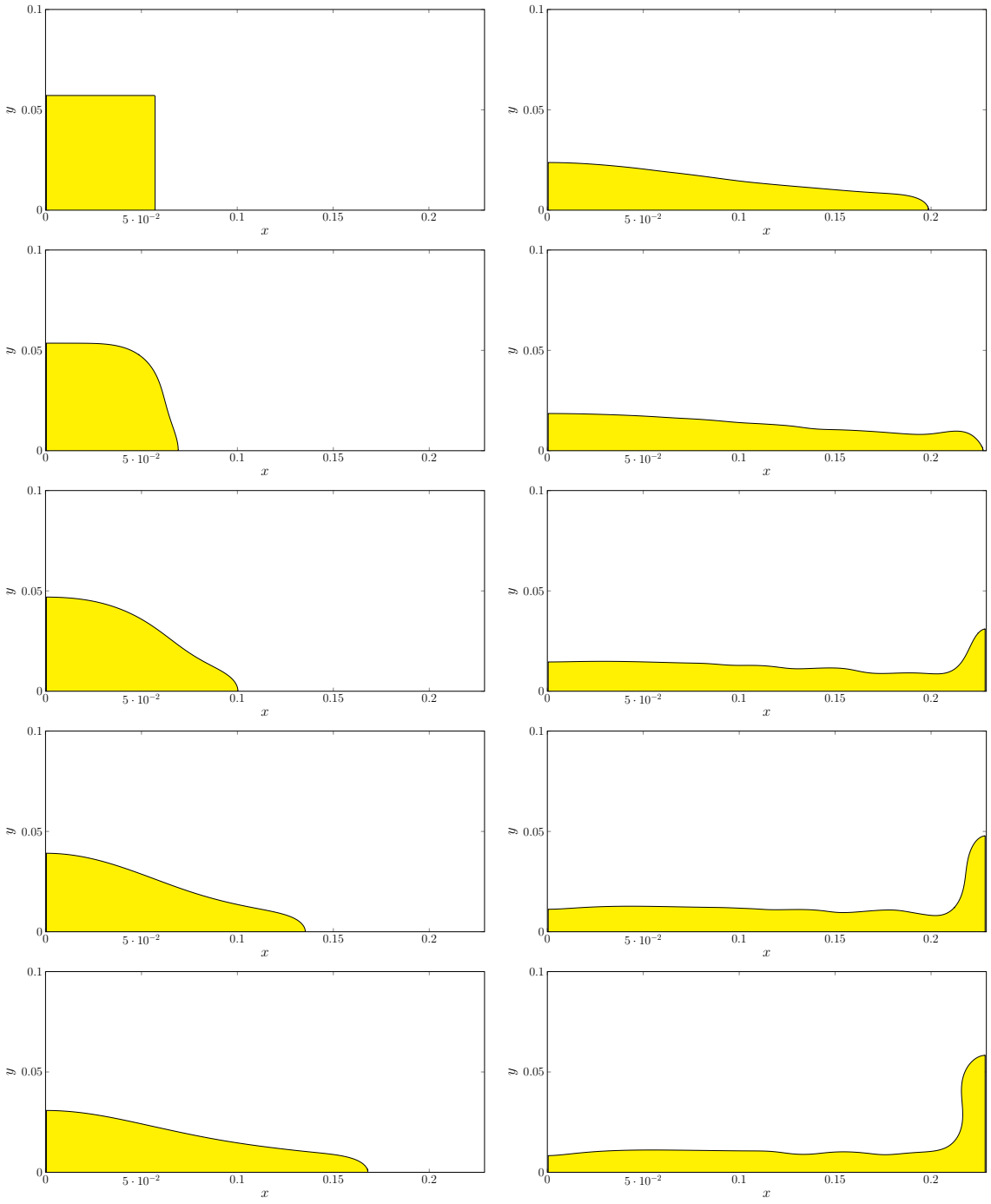

(a) $T = 0$ to $T = 2$

(b) $t = 2.5$ to $t = 5$

Figure 2.22: The evolution of the dam break test with water and air from $T = 0$ to $T = 5$ in 0.5 increments.

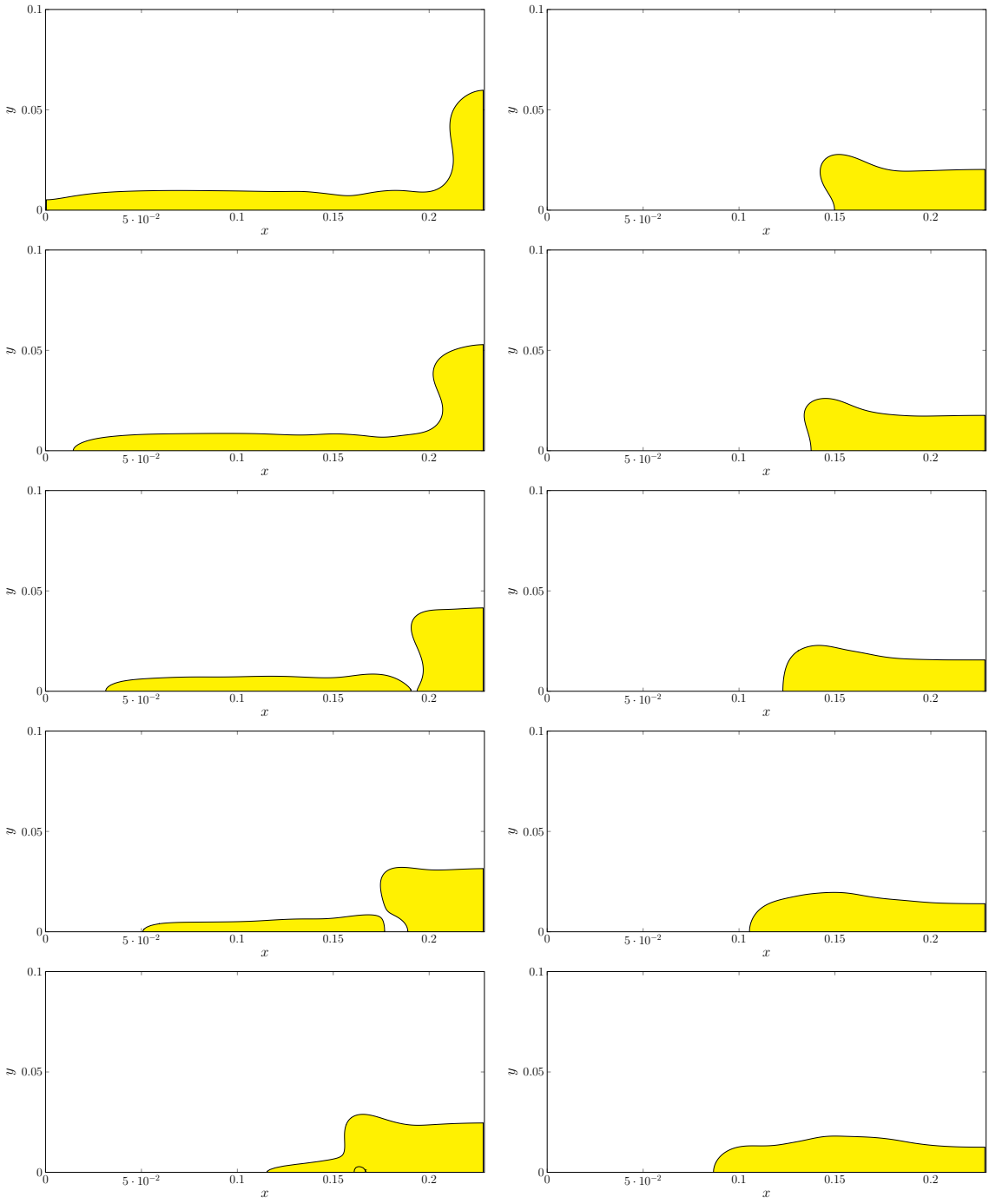

(a) $T = 5$ to $T = 7$ (b) $T = 7.5$ to $T = 9.5$

Figure 2.23: The evolution of the dam break test with water and air from $T = 5$ to $T = 9.5$ in 0.5 increments.

We also replace existing discretizations of the surface tension force on phase-field variables with one that has finite support around the transition region. The model has a parameter that allows it to transition from a smoothed continuum surface force to a fully sharp interface formulation, in which case the surface tension applied is equivalent to a sharp interface treatment using jump conditions. We compared our formulation of surface tension against other surface treatments used for the Cahn-Hilliard Navier-Stokes equations and found that our treatment compares favorably.

We have also noticed some limitations in the proposed scheme. As noted in Section 2.4.4, shearing flows with sharp γ transitions can lead to artifacts, though these are observed to diminish with refinement. The consistent advection used for the momentum equations are generally observed to be less numerically robust than a more classical WENO-based advection scheme. We have also observed that the evolution of γ can produce values outside the range $[0, 1]$, which can lead to negative densities if the density ratio is large. We correct this using the gamma redistribution scheme from [46], though we note that this redistribution is effectively global and thus less than ideal. In our implementation, it also comes at the cost of an additional Poisson solve; a more physically plausible solution to this problem is desirable.

2.6 Acknowledgements

The work in this chapter was supported in part by National Science Foundation award NSF-2006570 as well as University of California award M23PL6076.

Chapter 3

Conservative, bounded, and nonlinear discretization of the Cahn-Hilliard-Navier-Stokes equations

The Cahn-Hilliard equation describes phase separation in a binary mixture, typically modeled with a phase variable that represents the concentration of one phase or the concentration difference between the two phases. Though the system is energetically driven toward solutions within the physically meaningful range of the phase variable, numerical methods often struggle to maintain these bounds, leading to physically invalid quantities and numerical difficulties. In this work, we introduce a novel splitting and discretization for the Cahn-Hilliard equation, coupled with the Navier-Stokes equations, which inherently

preserves the bounds of the phase variable. This approach transforms the fourth-order Cahn-Hilliard equation into a second-order Helmholtz equation and a second-order nonlinear equation with implicit energy barriers, which is reformulated and solved with a safeguarded optimization-based solution method. Our scheme ensures the phase variable remains in the valid range, robustly handles large density ratios, conserves mass and momentum, maintains consistency between these quantities, and achieves second-order accuracy. We demonstrate the method's effectiveness through a variety of studies of two-dimensional, two-phase fluid mixtures.

3.1 Introduction

The Cahn-Hilliard equation describes the separation of a binary fluid mixture into domains that are pure in each phase [13, 25]. The mixture is typically modeled with a phase variable γ that represents the concentration of one phase ($\gamma \in [0, 1]$) or the concentration difference between the two phases ($\gamma \in [-1, 1]$). A variety of schemes have been developed for the numerical solution of the Cahn-Hilliard equation, including Fourier spectral methods [88, 43, 58], finite difference methods [32, 60, 38, 15, 47], and finite element methods [26, 10, 8, 29, 79, 41]. Though the system is energetically driven toward solutions within the physically meaningful range of γ, numerical methods for the solution of the Cahn-Hilliard equation may generate values outside this range, leading to physically invalid quantities and numerical difficulties [33, 46, 48]. Specifically, the phase variable is used to compute effective densities and viscosities. Under large density ratios, even a small excursion outside the valid

range of values for γ can result in negative effective densities, and hence ill-posedness of the viscous momentum equation and loss of positive-definiteness in numerical solvers.

To model two-phase incompressible flows, the Cahn-Hilliard equation is coupled to the incompressible Navier-Stokes equations. Several works have investigated variants of this system, including the case of matched densities [44, 5], the Boussinesq approximation [49, 63, 4], and the more general Cahn-Hilliard-Navier-Stokes (CHNS) equations with varying densities and viscosities [74, 72, 52, 21, 24, 38, 47, 33].

Cahn-Hilliard models vary based on the choice of potential and mobility functions, and this impacts the theoretical boundedness properties of the phase variable. A common approach is to use the Ginzburg-Landau double-well polynomial potential with constant mobility [31, 47, 33], suitable for situations where the diffusion is not strongly dependent on the concentration field. This model permits the phase variable to go outside physically meaningful bounds. The Cahn-Hilliard model with concentration-dependent degenerate mobility, which is zero in pure phases, has also been widely used [8]. In this form, given initial data that satisfies the physical bounds, the solution has been shown to maintain the bounds [27]. Another commonly employed model uses a logarithmic potential based on the Flory-Huggins theory of polymer solutions [1, 14, 6]. The potential is singular with infinite energy barriers at the pure concentrations $\gamma = 0$ or $\gamma = 1$, preventing the solution from attaining or exceeding these values. This formulation admits a maximum principle so that the analytic solution remains within bounds [20, 66, 1].

Preserving the physical bounds of the phase variable in numerical solutions can be challenging even in models that admit a maximum principle. This requirement may also

impose additional time step restrictions [18, 7, 67]. There have been many works aimed at developing bounds-preserving numerical methods. Several methods have addressed the issue of keeping γ in its physical bounds by using combinations of flux and slope limiters [31, 62]. Another approach to maintain the bounds of the phase variable is to explicitly clamp the variable in regions that exceed the bounds [23]. However, in order to conserve mass, the clipped mass must then be redistributed in a bounds-respecting manner. Chiu and Lin [16] applied such a strategy, uniformly distributing the clipped mass in the interfacial transition region. Huang et al. [46] proposed a boundedness mapping, a volume redistribution scheme that maintains the phase variable in the physical range. This method determines a set of conservative fluxes that maintain the global mass of the system while distributing mass from regions that undershoot or overshoot. This method was used to maintain bounds in the simulation of the Cahn-Hilliard-Navier-Stokes equations in both [47] and [33]. One drawback of the approach is that the choice of mass redistribution is controlled by a weight function and the determination of the fluxes requires a computationally expensive Poisson equation solve. The boundedness mapping approach was further developed in [48] for the more challenging case of multiphase flows with three or more phases.

When modeled with a singular logarithmic potential, numerical methods for the Cahn-Hilliard equation must be carefully designed to maintain the solution strictly within the physical bounds. Copetti and Elliott [18] developed a piecewise linear finite element scheme with backward Euler time discretization for the Cahn-Hilliard equation with a logarithmic free energy and gave conditions on the time step and initial data to ensure boundedness of the solution. Barrett and Blowey [7] further proved error bounds for this scheme.

Yang and Zhao [82] developed an unconditionally energy-stable scheme for the CH equation with logarithmic potential that is linear and symmetric positive definite.

Based on the work of Eyre [28], several approaches utilize convex splitting, where the potential is expressed as a difference of convex functions and a convex nonlinear subproblem is formulated and solved implicitly to maintain the solution bounds. Li et al. [59] proposed an unconditionally stable nonlinear scheme based on convex splitting of the potential and solved by Newton iteration. The convergence of the scheme was analyzed in [22] by converting the problem into a convex minimization. Also based on a convex splitting of the potential and implicit treatment of the logarithmic terms, Chen et al. [14] developed first and second order finite difference schemes where the positivity of the logarithmic argument is maintained without incurring an additional time step restriction.

Bailo et al. [6] used a convex splitting approach combined with an upwind methodology for discretization of the mobility to construct a semi-implicit scheme that unconditionally maintains the boundedness of the phase variable. Acosta-Soba et al. [3] also pursued an upwind methodology for both the flow velocity and the mobility in a discontinuous Galerkin scheme for the convective Cahn-Hilliard equation with polynomial potential and degenerate mobility, maintaining the bounds on the solution. A bounds-preserving upwind scheme was also developed in [45].

In this chapter, we introduce a novel splitting for the numerical solution of the Cahn-Hilliard-Navier-Stokes equations that maintains the phase variable $\gamma \in [0, 1]$ by construction. We use a piecewise potential approximation with logarithmic terms singular at the pure phases. Similar to convex splitting approaches, our method results in a nonlinear

equation implicit in the phase variable that maintains boundedness of the solution. We reformulate the nonlinear equation as a convex optimization facilitating solution through a safeguarded optimization-based scheme. The resulting method is second order accurate and can robustly simulate large density ratios. We demonstrate the method's effectiveness through a variety of studies of two-dimensional, two-phase fluid mixtures.

3.2 Governing equations

3.2.1 Cahn-Hilliard equation

The Cahn-Hilliard equations can be expressed as

$$\frac{\partial \gamma}{\partial t} + \nabla \cdot (\mathbf{u}\gamma) = \nabla \cdot (M \nabla \xi) + S_\gamma \tag{3.1}$$

$$\xi = \lambda(F'(\gamma) - \nabla^2 \gamma) \tag{3.2}$$

$$\lambda = \frac{3}{2\sqrt{2}} \sigma \eta. \tag{3.3}$$

We label the two fluid phases as 0 and 1. The volume fraction of fluid 1 is represented as the phase-field function $\gamma \in [0, 1]$. The chemical potential is ξ. λ, called the mixing energy density in Huang et al. [46], is a parameter that incorporates the surface tension constant σ and η, a parameter which influences the width of the phase transition region. $\mathbf{u}$ is the fluid velocity, M is the mobility, S_γ is an external source term, and F is a double well potential function. The details of F and its corresponding derivative F' are described in Section 3.3.1.

The properties of fluid phases 0 and 1 are density (ρ_0, ρ_1) and viscosity (μ_0, μ_1) respectively. For a given location $\mathbf{x}$, we compute the effective density and viscosity of the phase mixture with

$$\rho(\mathbf{x}) = \rho_0 + (\rho_1 - \rho_0)\,\gamma(\mathbf{x}) \tag{3.4}$$

$$\mu(\mathbf{x}) = \mu_0 + (\mu_1 - \mu_0)\,\gamma(\mathbf{x}). \tag{3.5}$$

3.2.2 Navier-Stokes equations

The Navier-Stokes equations for incompressible flow are given by

$$\frac{\partial \rho}{\partial t} + \nabla \cdot \mathbf{m} = S_m \tag{3.6}$$

$$\nabla \cdot \mathbf{u} = 0 \tag{3.7}$$

$$\frac{\partial(\rho \mathbf{u})}{\partial t} + \nabla \cdot (\mathbf{m} \otimes \mathbf{u}) = -\nabla p + \nabla \cdot (\mu(\nabla \mathbf{u} + (\nabla \mathbf{u})^T)) + \rho g + \sigma \kappa \nabla(h\,(\gamma)) + S_{\mathbf{u}}, \tag{3.8}$$

where ρ is the effective density, $\mathbf{m}$ is the mass flux consistent with the γ evolution (3.1) [47], S_m is an external mass source, $\mathbf{u}$ is the velocity, p is the pressure, μ is the effective viscosity, g is the acceleration of gravity, σ is the coefficient of surface tension, κ is the interface curvature, $h(\gamma)$ is a regularized Heaviside function as defined in [33], and $S_{\mathbf{u}}$ is the external momentum source.

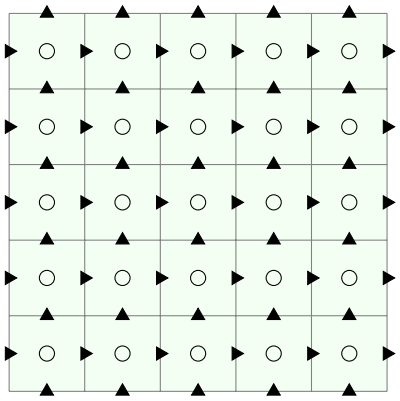

Figure 3.1: The MAC grid stores γ and pressure on cell centers (circles). Velocties are stored by component on faces (represented by triangles), (Reproduced from [33].)

3.3 Discretizations

In this section we describe the temporal and spatial discretizations of the Cahn-Hilliard and Navier-Stokes equations. As in [33], we use a uniform MAC grid (Figure 3.1) with γ and pressure stored at cell centers. Velocities are split by components and stored on cell faces. Unless otherwise specified, we use the same discretizations as in [33].

3.3.1 Cahn-Hilliard equation

Goulding et al. [33] introduced a discretization that was simple and effective, but it did not ensure $\gamma \in [0, 1]$. Instead, they used the bounds-enforcing scheme introduced in Huang et al. [46] to correct gamma in a postprocess. That postprocess is non-local, which is undesirable since mass conservation is a local conservation property. It also requires a Poisson solve to determine associated conservative fluxes which incurs significant computational cost [33]. In this chapter, we construct a scheme that automatically guarantees $\gamma \in (0, 1)$ without the need for any postprocessing steps. We do this by formulating F with

a barrier at 0 and 1 (much as some existing formulations of F do [13]) and treating the term $F'(\gamma^{n+1})$ implicitly.

Scheme derivation

We begin our formulation of our scheme with the scheme from [33] where the fourth order Cahn-Hilliard equation is split into two second-order Helmholtz equations as

$$A - s\widehat{\Delta t}\nabla^2 A = \gamma^* + B + \widehat{\Delta t} S_\gamma^{n+1} \tag{3.9}$$

$$\gamma^{n+1} - s\widehat{\Delta t}\nabla^2 \gamma^{n+1} = A - B, \tag{3.10}$$

where γ^* is the result of advecting γ^n. In the absence of source terms, the scheme should be discretely mass conserving, requiring

$$\int_\Omega \gamma^{n+1}\, dV = \int_\Omega \gamma^n\, dV \tag{3.11}$$

Note that by the divergence theorem, any field B with zero flux or periodic boundary conditions satisfies

$$\int_\Omega \nabla^2 B\, dV = 0, \tag{3.12}$$

so that Laplacian terms do not contribute to mass conservation. Therefore, assuming $S_\gamma^{n+1} = 0$ and integrating equations (3.9) and (3.10), we get

$$\int_\Omega A\,dV = \int_\Omega \gamma^*\,dV + \int_\Omega B\,dV \tag{3.13}$$

$$\int_\Omega \gamma^{n+1}\,dV = \int_\Omega A\,dV - \int_\Omega B\,dV \tag{3.14}$$

$$= \int_\Omega \gamma^*\,dV = \int_\Omega \gamma^n\,dV, \tag{3.15}$$

where the last equality comes from assuming conservative advection. Observe that the contents of B do not matter, since it is added before solving a Helmholtz equation and subtracted off afterwards. As a useful rule, terms that are not Laplacians must be added and subtracted in this way to achieve conservation.

Next we turn to the general form we want for our scheme. Schemes such as [47] also include $\nabla^2 F'(\gamma)$ terms, which we allow in our scheme as well. We also use γ^{AB}, described below, as an explicit estimate of γ^{n+1}. This leads to a potential general scheme of the form

$$A + a_1\nabla^2 A = \gamma^* + a_2\gamma^{AB} + a_3\nabla^2 F'(\gamma^{AB}) + a_4 F'(\gamma^{AB}) \tag{3.16}$$

$$\gamma^{n+1} + c_1\nabla^2\gamma^{n+1} = A + c_2\gamma^{AB} + c_3\nabla^2 F'(\gamma^{AB}) + c_4 F'(\gamma^{AB}) + c_5 F'(\gamma^{n+1}), \tag{3.17}$$

which adds in the necessary implicit treatment of F' but fails to be conservative since the $F'(\gamma^{n+1})$ term is not canceled (unless $c_5 = 0$, which would then not be implicit). To restore

conservation, we need to cancel out the implicit term, which suggests a scheme of the form

$$A + a_1\nabla^2 A = \gamma^* + a_2\gamma^{AB} + a_3\nabla^2 F'(\gamma^{AB}) + a_4 F'(\gamma^{AB}) \tag{3.18}$$

$$C + c_1\nabla^2 C = A + c_2\gamma^{AB} + c_3\nabla^2 F'(\gamma^{AB}) + c_4 F'(\gamma^{AB}) + c_5 F'(\gamma^{n+1}) \tag{3.19}$$

$$\gamma^{n+1} = C + g_2\gamma^{AB} + g_3\nabla^2 F'(\gamma^{AB}) + g_4 F'(\gamma^{AB}) + g_5 F'(\gamma^{n+1}), \tag{3.20}$$

which will be conservative provided $a_2 + c_2 + g_2 = 0$, $a_4 + c_4 + g_4 = 0$, and $c_5 + g_5 = 0$. Schemes of this form exist, but the $F'(\gamma^{AB})$ terms are problematic, since $F(\gamma)$ has barriers at 0 and 1 but γ^{AB} need not lie within this range. Instead, we replace them with $F'(\gamma)^{AB} = 2F'(\gamma^n) - F'(\gamma^{n-1})$, which is safe to compute since $0 < \gamma^n < 1$ will always be bounded. This suggests we should look for a scheme of the form

$$A + a_1\nabla^2 A = \gamma^* + a_2\gamma^{AB} + a_3\nabla^2 F'(\gamma)^{AB} + a_4 F'(\gamma)^{AB} \tag{3.21}$$

$$C + c_1\nabla^2 C = A + c_2\gamma^{AB} + c_3\nabla^2 F'(\gamma)^{AB} + c_4 F'(\gamma)^{AB} + c_5 F'(\gamma^{n+1}) \tag{3.22}$$

$$\gamma^{n+1} = C + g_2\gamma^{AB} + g_3\nabla^2 F'(\gamma)^{AB} + g_4 F'(\gamma)^{AB} + g_5 F'(\gamma^{n+1}) \tag{3.23}$$

subject to the constraints on the coefficients needed for conservation.

What remains is to select coefficients such that the scheme is consistent and formally 1.5 order accurate. We also prefer to discard terms from (3.23) where possible.

Performing the truncation analysis leads to the scheme

$$A - s\widehat{\Delta t}\nabla^2 A = \gamma^* - 2\gamma^{AB} + \widehat{\Delta t} M\lambda \nabla^2 F'(\gamma)^{AB} \tag{3.24}$$

$$C - s\widehat{\Delta t}\nabla^2 C = A + 2\gamma^{AB} - bs\widehat{\Delta t}^2 \nabla^2 F'(\gamma)^{AB} + b\widehat{\Delta t} F'(\gamma^{n+1}) \tag{3.25}$$

$$\gamma^{n+1} = C - b\widehat{\Delta t} F'(\gamma^{n+1}), \tag{3.26}$$

where $s = \sqrt{\frac{M\lambda}{\widehat{\Delta t}}}$ and $\widehat{\Delta t} = \frac{2}{3}\Delta t$. This scheme is consistent for any constant b. We examine restrictions on this constant in Section 3.3.1.

Avoiding nested solves

We will solve (3.25) using Newton's method. Observe that for each Newton iteration, we must solve (3.26), which is a pointwise nonlinear equation. To stabilize Newton's method, we would like to formulate it as an optimization problem so that line searches can be employed. This requires us to integrate (3.25) with respect to C to form the objective, so that the optimality conditions recover (3.25). If we let $\gamma^{n+1} = f(C)$ denote the process of solving (3.26), then forming the objective requires us to integrate the function f. If f is obtained as that output of a numerical procedure, then computing this integral would be problematic. To have a practical chance of computing this integral, we will need a closed-form solution for f. Let g be the integral so that $\gamma^{n+1} = g'(C)$.

For most choices of the double-well potential F, the function $g'(C)$ will not be solvable in closed form. We must therefore restrict the form of F in such a way that it has the correct qualitative form while allowing g' to be computed and integrated in closed form.

We note that this is possible for two special forms. If $F(x)$ is a cubic polynomial, then

$$F(x) = a_3x^3 + a_2x^2 + a_1x + a_0 \tag{3.27}$$

$$\gamma = C - b\widehat{\Delta t}F'(\gamma) = C - b\widehat{\Delta t}(3a_3\gamma^2 + 2a_2\gamma + a_1), \tag{3.28}$$

which leads to a quadratic equation in γ that can be solved in closed form. Further, the quadratic equation for γ takes the general form $\gamma = g'(C) = k_0 + \sqrt{k_1 + k_2C}$, which can be integrated in closed form. Another form for F with this property is

$$F(x) = a_2x^2 + a_1x + a_0 + a_3\ln(x) \tag{3.29}$$

$$\gamma = C - b\widehat{\Delta t}F'(\gamma) = C - b\widehat{\Delta t}(2a_2\gamma + a_1 + a_3\gamma^{-1}). \tag{3.30}$$

Clearing the fractions leads to another quadratic equation in γ, this time of the form $\gamma = g'(C) = (k_0C + k_1) + \sqrt{(k_0C + k_1)^2 + k_2}$, which can also be integrated in closed form. (3.29) is notable in that it has a barrier at 0.

A suitable formulation of F must be a double-well energy function with barriers at 0 and 1. Neither form above has these properties, but a suitable function F can be constructed by combining energy terms of these forms piecewise. We note that piecewise formulations for F have been employed before [9, 34, 86]. It is clear that two logarithmic pieces will be required to get the necessary barriers. In addition, two cubic pieces are used

to complete the double-well profile. We are thus looking for a potential of the form

$$F(\gamma) = \begin{cases} F_0(\gamma) & 0 \le \gamma \le r \\ F_1(\gamma) & r < \gamma < \frac{1}{2} \\ F_1(1-\gamma) & \frac{1}{2} < \gamma \le 1 - r \\ F_0(1-\gamma) & 1 - r < \gamma \le 1 \end{cases} \tag{3.31}$$

$$F_0(\gamma) = b_2 x^2 + b_1 x + b_0 + b_3 \ln(x) \tag{3.32}$$

$$F_1(\gamma) = a_3 x^3 + a_2 x^2 + a_1 x + a_0 \tag{3.33}$$

where we have assumed the symmetry $F(\gamma) = F(1-\gamma)$.

When solving the equation $\gamma = C - b\widehat{\Delta t} F'(\gamma)$, there is an additional complication. The piecewise boundaries of $F'(\gamma)$ are in terms of γ, not C. The corresponding boundaries for C could of course be computed by substituting boundary values for γ and solving for C, but we instead pursue a simpler strategy. We note that the double-well potential F will have two minima and a maximum. If we place the minima of F at r and $1-r$ and the maximum at $\frac{1}{2}$, then $F'(r) = F'(\frac{1}{2}) = F'(1-r) = 0$. If γ is one of these values, then $\gamma = C - b\widehat{\Delta t} F'(\gamma) = C$, so that the piecewise boundaries for γ and C are the same.

The piecewise formulation for F has eight degrees of freedom. Enforcing C^2 continuity eliminates four degrees of freedom. Placing a minimum at r and shifting the minimum to zero (i.e., $F'(r) = F(r) = 0$) eliminates two more. We only need to construct $F(\gamma)$ up to a global scale (we will scale it appropriately later), which eliminates one more. We are

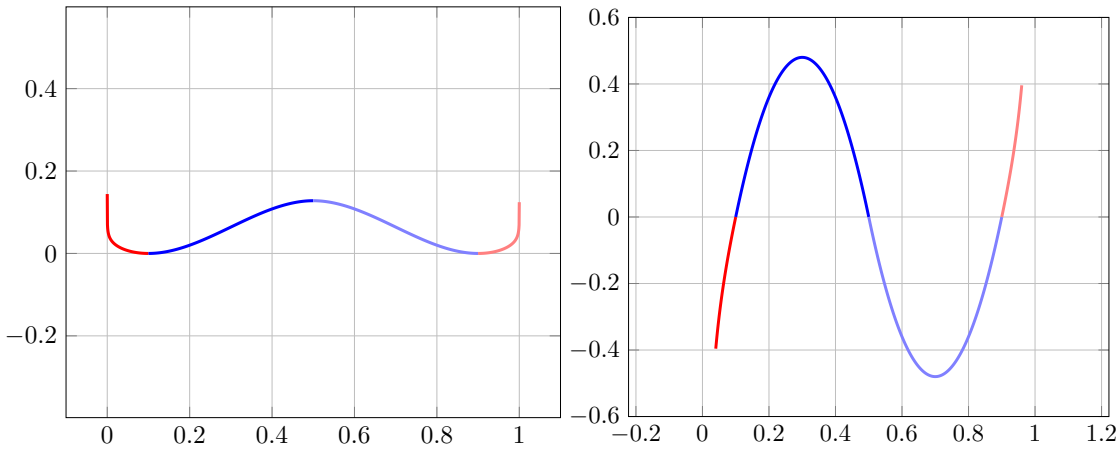

Figure 3.2: Plots of $F(C)$ (left) and $F'(C)$ (right) corresponding to $q = 0.5$ and $r = 0.1$.

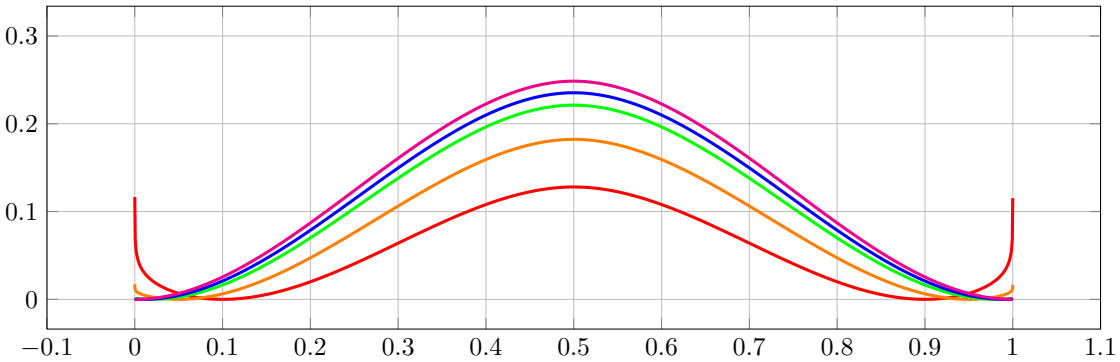

Figure 3.3: Plot of $F(C)$ for different values of r: 0.1 (—), 0.05 (—), 0.02 (—), 0.01 (—), and 0.001 (—). The potential function converges pointwise in the limit $r \to 0$ over the range $0 < C < 1$.

left with one more degree of freedom, so we choose to enforce C^3 continuity at r. We are now left with

$$F_0(\gamma) = 3(\gamma - r)(8r^2 - 4r\gamma - r + \gamma) - 12r^3 \ln \frac{\gamma}{r} \qquad F_1(\gamma) = (r - \gamma)^2(3 - 2r - 4\gamma).$$

Figure 3.2 shows a plot of $F(\gamma)$ and $F'(\gamma)$. Besides a global scale, this potential is also a function of the parameter r, which specifies the location of the minima. The dependence of this potential on r can be seen in Figure 3.3. The potential converges in the limit $r \to 0$,

which allows our scheme to be run with r very nearly zero. This is important, since in regions far from the interface, γ will be comparable to r or $1-r$.

The function $\gamma = g'(C)$ is defined as the solution of $\gamma = C - kF'(\gamma)$, where in the scheme we have the constant $k = b\widehat{\Delta t}$. The global scaling on F is absorbed into the constant b. g' can be expressed in closed form as

$$g'(C) = \begin{cases} g_0'(C) & 0 \le C \le r \\ g_1'(C) & r < C < \frac{1}{2} \\ 1 - g_1'(1-C) & \frac{1}{2} < C \le 1-r \\ 1 - g_0'(1-C) & 1-r < C \le 1 \end{cases} \tag{3.34}$$

$$q = 6k(1-2r) \qquad p = 1 + 6k(1-4r) \qquad s = 6r(1-6r)k \tag{3.35}$$

$$g_0'(C) = \frac{1}{2p} h_0'(C+s) \qquad h_0'(x) = x + \sqrt{x^2+L} = -\frac{L}{x - \sqrt{x^2+L}} \qquad L = 48kr^3p \tag{3.36}$$

$$g_1'(C) = \frac{1}{2} + h_1'\left(\frac{C-\frac{1}{2}}{12k}\right) \quad h_1'(x) = K - \sqrt{K^2 - x} = \frac{x}{K + \sqrt{K^2-x}} \quad K = \frac{1-q}{24k} \tag{3.37}$$

We note that the first form of h_0' and h_1' is convenient for differentiation and integration, but the second form is more numerically robust since $x > 0$ and $K > 0$. In addition to $g'(C)$, which is used to compute γ^{n+1}, we also need g (for the optimization objective) and

g'' (for the Hessian of the objective). The derivative g'' is straightforward

$$g''(C) = \begin{cases} g_0''(C) & 0 \le C \le r \\ g_1''(C) & r < C < \frac{1}{2} \\ g_1''(1-C) & \frac{1}{2} < C \le 1-r \\ g_0''(1-C) & 1-r < C \le 1 \end{cases} \tag{3.38}$$

$$g_0''(C) = \frac{1}{2p} h_0''(C+s) \qquad h_0''(x) = 1 + \frac{x}{\sqrt{x^2+L}} \tag{3.39}$$

$$g_1''(C) = \frac{1}{12k} h_1'' \left(\frac{C - \frac{1}{2}}{12k} \right) \qquad h_1''(x) = \frac{1}{2\sqrt{K^2 - x}} \tag{3.40}$$

When computing the integral, we must be careful to ensure continuity.

$$g(C) = \begin{cases} g_0(C) - g_0(r) + g_1(r) & 0 \le C \le r \\ g_1(C) & r < C < \frac{1}{2} \\ C - \frac{1}{2} + g_1(1-C) & \frac{1}{2} < C \le 1-r \\ C - \frac{1}{2} + g_0(1-C) - g_0(r) + g_1(r) & 1-r < C \le 1 \end{cases} \tag{3.41}$$

$$g_0(C) = \frac{1}{2p} h_0(C+s) \qquad h_0(x) = \frac{x}{2} h_0'(x) + \frac{L}{2} \ln(h_0'(x)) \tag{3.42}$$

$$g_1(C) = \frac{C}{2} + 12k h_1 \left(\frac{C - \frac{1}{2}}{12k} \right) \qquad h_1(x) = Kx + \frac{2}{3}(K^2 - x)^{3/2} \tag{3.43}$$

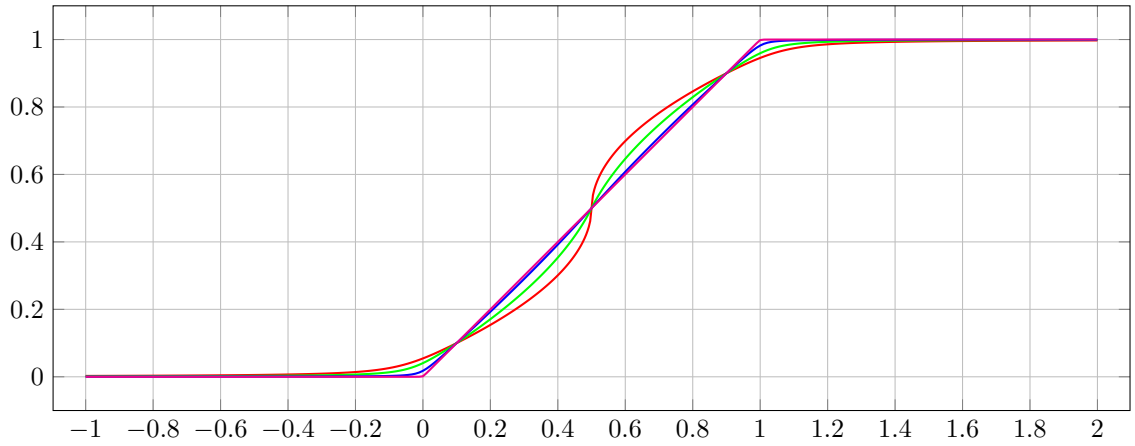

Figure 3.4: Plot of $g'(C)$ for different values of q: 0.99 (—), 0.9 (—), 0.5 (—), 0.001 (—). The function g' converges to piecewise-linear in the limit $q \to 0$ and develops an infinite slope at $C = \frac{1}{2}$ in the limit $q \to 1$. When $q > 1$, (3.26), when viewed as a function $C(\gamma)$, is not monotonic. In this case, g' would become multivalued. Useful values of q are thus restricted to $0 < q < 1$ to ensure that (3.26) has a unique and continuous solution.

In addition to r, the function g' also depends on k. The influence of this parameter is easier to understand in terms of the related quantity q, as seen in Figure 3.4. In the limit $q \to 0$, $\gamma \to C$ when $0 < C < 1$, with γ clamped to 0 or 1 outside this interval. In the limit $q \to 1$, we have $g'(\frac{1}{2}) \to \infty$. For $q > 1$ the relationship $C = \gamma + kF'(\gamma)$ ceases to be monotonic, so that its inverse g' does not exist as a continuous function. For the proposed scheme to exist, we must have $0 < q < 1$. While q is always positive, the requirement $q < 1$ effectively imposes a time step restriction. Figure 3.5 shows plots of $g(C)$ and $g''(C)$. Note that $g''(C)$ is continuous and positive (from (3.38) and (3.40)), which improves the conditioning of the optimization problem.

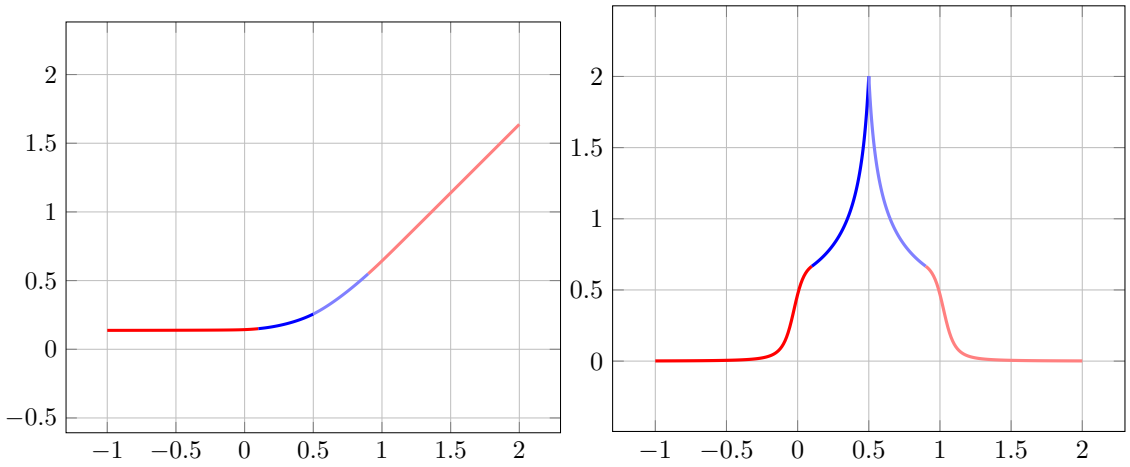

Figure 3.5: Plots of $g(C)$ (left) and $g''(C)$ (right) corresponding to $q = 0.5$ and $r = 0.1$.

Temporal discretization

We begin by combining (3.1) and (3.2) to get the form of the Cahn-Hilliard equation that we wish to discretize:

$$\frac{\partial \gamma}{\partial t} + \nabla \cdot (\mathbf{u}\gamma) = M\lambda\nabla^2(F'(\gamma) - \nabla^2\gamma) + S_\gamma. \tag{3.44}$$

As in Goulding et al. [33], we discretize the time derivative using the second-order scheme $\frac{\alpha\gamma^{n+1} - \alpha\gamma^{BD}}{\Delta t}$ with $\alpha = \frac{3}{2}$ and $\gamma^{BD} = \frac{4}{3}\gamma^n - \frac{1}{3}\gamma^{n-1}$. For the first time step we use a first-order single-step scheme with $\alpha = 1$ and $\gamma^{BD} = \gamma^n$. Explicit quantities for $\mathbf{u}$ and γ are discretized using an Adams-Bashforth scheme, where $\gamma^{AB} = \gamma^n$, $\mathbf{u}^{AB} = \mathbf{u}^n$ in the first step and $\gamma^{AB} = 2\gamma^n - \gamma^{n-1}$, $\mathbf{u}^{AB} = 2\mathbf{u}^n - \mathbf{u}^{n-1}$ in subsequent steps. We let $\widehat{\Delta t} = \Delta t/\alpha$, as α and Δt always occur together in practice.

Next, we derive the scheme presented in Section 3.3.1 directly from Equation (3.44). It will be demonstrated in Section 3.4.1 that the scheme has $O(\Delta t^{1.5})$ convergence. We begin

with temporal discretization choices for γ and $\mathbf{u}$,

$$\frac{\gamma^{n+1} - \gamma^{BD}}{\widehat{\Delta t}} + \nabla \cdot \left(\mathbf{u}^{AB}\gamma^{AB}\right) = M\lambda\nabla^2\left(F'\left(\gamma^{n+1}\right) - \nabla^2\gamma^{n+1}\right) + S_\gamma^{n+1}. \tag{3.45}$$

Next we split out the advection term as an update from γ^{BD} to an intermediate quantity γ^*:

$$\frac{\gamma^* - \gamma^{BD}}{\widehat{\Delta t}} + \nabla \cdot \left(\mathbf{u}^{AB}\gamma^{AB}\right) = 0 \tag{3.46}$$

$$\frac{\gamma^{n+1} - \gamma^*}{\widehat{\Delta t}} = M\lambda\nabla^2\left(F'\left(\gamma^{n+1}\right) - \nabla^2\gamma^{n+1}\right) + S_\gamma^{n+1}. \tag{3.47}$$

Expanding on Shen and Yang [74] and Goulding et al. [33], we define s so that $s^2\widehat{\Delta t} = M\lambda$ and introduce extra terms (denoted T_1, T_2, and T_3) to facilitate the further splitting of the equation. Each term introduces a small error but decreases rapidly under refinement (noting $s = O(\Delta t^{-0.5})$ and $a = O(\Delta t)$, with M and λ fixed):

$$T_1 = 2s(\gamma^{n+1} - \gamma^{AB}) = O(\Delta t^{1.5}) \tag{3.48}$$

$$T_2 = -M\lambda a\nabla^2\left(F'(\gamma^{n+1}) - F'(\gamma)^{AB}\right) = O(\Delta t^3) \tag{3.49}$$

$$T_3 = (as - M\lambda)\left(F'(\gamma^{n+1}) - F'(\gamma)^{AB}\right) = O(\Delta t^2) \tag{3.50}$$

We incorporate the terms into Eq. (3.47) as

$$\frac{\gamma^{n+1} - \gamma^*}{\widehat{\Delta t}} = \nabla^2\left(M\lambda F'(\gamma^{n+1}) - M\lambda\nabla^2\gamma^{n+1} + T_1 + T_2 + T_3\right) + S_\gamma^{n+1}. \tag{3.51}$$

Observe that the inclusion of T_1 formally limits us to convergence order 1.5. We define C according to (3.26) as

$$C = \gamma^{n+1} + aF'(\gamma^{n+1}), \tag{3.52}$$

Plugging in the definitions of T_1, T_2, T_3, and C into Eq. (3.51), cancelling like terms, and rearranging, we get

$$\begin{aligned}\frac{\gamma^{n+1}-\gamma^*}{\widehat{\Delta t}} = \nabla^2\Big(&sC - s^2\widehat{\Delta t}\nabla^2 C + (M\lambda - as)\,F'(\gamma)^{AB} + s\gamma^{n+1} - 2s\gamma^{AB} \\ &+ as^2\widehat{\Delta t}\nabla^2 F'(\gamma)^{AB}\Big) + S_\gamma^{n+1}\end{aligned} \tag{3.53}$$

Using Eq. (3.52) to eliminate γ^{n+1} in Eq. (3.53) and defining

$$A = C - s\widehat{\Delta t}\nabla^2 C - aF'(\gamma^{n+1}) - 2\gamma^{AB} + as\widehat{\Delta t}\nabla^2 F'(\gamma)^{AB}, \tag{3.54}$$

Eq. (3.53) becomes

$$A - s\widehat{\Delta t}\nabla^2 A = \gamma^* - 2\gamma^{AB} + \widehat{\Delta t}M\lambda\nabla^2 F'(\gamma)^{AB} + \widehat{\Delta t}S_\gamma^{n+1}. \tag{3.55}$$

Recall $\gamma^{n+1} = g'(C)$ as described in Section 3.3.1. Substituting this into Eq. (3.52) and rearranging, we get $aF'(\gamma^{n+1}) = C - g'(C)$. Substituting this into Eq. (3.54) and combining the right hand side into B, we get a nonlinear equation satisfied by C:

$$B = A + 2\gamma^{AB} - as\widehat{\Delta t}\nabla^2 F'(\gamma)^{AB} \qquad\qquad g'(C) - s\widehat{\Delta t}\nabla^2 C = B. \tag{3.56}$$

From these expressions, we have our four-stage scheme:

1. Compute γ^* by advection using Eq. (3.46).

2. Solve the Helmholtz equation for A given in Eq. (3.55).

3. Solve the nonlinear equation for C given in Eq. (3.56).

4. Update γ^{n+1} as $\gamma^{n+1} = g'(C)$.

Optimization-based formulation of the nonlinear solve

We solve the nonlinear equation (3.56) for C by reformulating it as a minimization of the objective function

$$E = \sum_i g(C_i) - \frac{1}{2} s\widehat{\Delta t} \sum_{i,j} C_i L_{ij} C_j - \sum_i C_i B_i, \tag{3.57}$$

where L is the discrete Laplacian matrix. The corresponding gradient is

$$\frac{\partial E}{\partial C_i} = g'(C_i) - s\widehat{\Delta t} \sum_j L_{ij} C_j - B_i \tag{3.58}$$

so that the optimality conditions $\frac{\partial E}{\partial C_i} = 0$ reduce to (3.56). Since we will be using a Newton-based solver, we will also need the Hessian

$$\frac{\partial^2 E}{\partial C_i \partial C_j} = \delta_{ij} g''(C_i) - s\widehat{\Delta t} L_{ij}. \tag{3.59}$$

Since $g''(C_i) > 0$, the Hessian is symmetric and positive definite. The optimization problem is thus convex, guaranteeing a unique local minimum, which is also the global minimum. We

solve this optimization problem using Newton's method with Wolfe conditions line searches. We use zero as the initial guess during the first time step and C^{n-1} as the initial guess for the second time step. Thereafter, we warm-start our solver using $C^{AB} = 2C^{n-1} - C^{n-2}$ as the initial guess.

Boundary conditions

We consider two types of boundary conditions for γ: periodic and Neumann ($\mathbf{n} \cdot \nabla\gamma^{n+1} = 0$). In order to solve both implicit equations, we need boundary conditions for C and A. From $\gamma^{n+1} = g'(C)$ we have

$$\mathbf{n} \cdot \nabla\gamma^{n+1} = g''(C)\,(\mathbf{n} \cdot \nabla C)\,. \tag{3.60}$$

As $g''(C) \neq 0$, $\mathbf{n} \cdot \nabla\gamma^{n+1} = 0$ implies $\mathbf{n} \cdot \nabla C = 0$. For $\mathbf{n} \cdot \nabla A$, we start by substituting Eq. (3.52) into Eq. (3.54):

$$A = C - s\widehat{\Delta t}\nabla^2\gamma^{n+1} - as\widehat{\Delta t}\nabla^2 F'(\gamma^{n+1}) - 2\gamma^{AB} + as\widehat{\Delta t}\nabla^2 F'(\gamma)^{AB} - aF'(\gamma^{n+1}) \tag{3.61}$$

$$\begin{aligned} &= \gamma^{n+1} - 2\gamma^{AB} + s\widehat{\Delta t}\left(F'(\gamma^{n+1}) - \nabla^2\gamma^{n+1}\right) - s\widehat{\Delta t}F'(\gamma^{n+1}) \\ &\quad - as\widehat{\Delta t}\nabla^2\left(F'(\gamma^{n+1}) - F'(\gamma)^{AB}\right). \end{aligned} \tag{3.62}$$

As in [47], we define ξ^{n+1} to be a discrete version of the chemical potential following the derivation in Section 3.3.1 as

$$\begin{aligned} \xi^{n+1} = \lambda\Big(&F'(\gamma^{n+1}) - \nabla^2\gamma^{n+1} + \frac{2s}{M\lambda}\left(\gamma^{n+1} - \gamma^{AB}\right) - a\nabla^2\left(F'(\gamma^{n+1}) - F'(\gamma)^{AB}\right) \\ &- \frac{(M\lambda - as)}{M\lambda}\left(F'(\gamma^{n+1}) - F'(\gamma)^{AB}\right)\Big). \end{aligned} \tag{3.63}$$

Substituting in our equation for A leads to

$$A = \left(a - s\widehat{\Delta t}\right) F'(\gamma)^{AB} - \left(\gamma^{n+1} + aF'(\gamma^{n+1})\right) + \frac{s\widehat{\Delta t}}{\lambda}\xi^{n+1}. \tag{3.64}$$

Recognizing that $\mathbf{n} \cdot \nabla F'(\gamma) = F''(\gamma)\left(\mathbf{n} \cdot \nabla\gamma\right)$, the boundary condition for A is

$$\begin{aligned} \mathbf{n} \cdot \nabla A = &\left(a - s\widehat{\Delta t}\right)\left(2F''(\gamma^n)\left(\mathbf{n} \cdot \nabla\gamma^n\right) - F''(\gamma^{n-1})\left(\mathbf{n} \cdot \nabla\gamma^{n-1}\right)\right) - \mathbf{n} \cdot \nabla\gamma^{n+1} \\ &- aF''(\gamma^{n+1})\left(\mathbf{n} \cdot \nabla\gamma^{n+1}\right) + \frac{s\widehat{\Delta t}}{\lambda}\mathbf{n} \cdot \nabla\xi^{n+1} \end{aligned} \tag{3.65}$$

$$= \frac{s\widehat{\Delta t}}{\lambda}\mathbf{n} \cdot \nabla\xi^{n+1}, \tag{3.66}$$

where we have used $\mathbf{n} \cdot \nabla\gamma^{n-1} = \mathbf{n} \cdot \nabla\gamma^n = \mathbf{n} \cdot \nabla\gamma^{n+1} = 0$. Following [47] we use the boundary condition $\mathbf{n} \cdot \nabla\xi^{n+1} = 0$, which leads to $\mathbf{n} \cdot \nabla A = 0$. This gives us the necessary boundary conditions for both of our systems.

3.3.2 Navier-Stokes equations

Temporal discretization

We discretize the Navier-Stokes equations as in Goulding et al. [33]. As in Section 3.3.1, we discretize the time derivative as $\frac{\alpha\rho^{n+1}\mathbf{u}^{n+1} - \alpha(\rho\mathbf{u})^{BD}}{\Delta t}$. For the first time step, $\alpha = 1$ and $(\rho\mathbf{u})^{BD} = \rho^n\mathbf{u}^n$. To achieve second-order accuracy, we thereafter use a backwards-difference scheme with $\alpha = \frac{3}{2}$ and $(\rho\mathbf{u})^{BD} = \frac{4}{3}\rho^n\mathbf{u}^n - \frac{1}{3}\rho^{n-1}\mathbf{u}^{n-1}$. Explicit quantities for $\mathbf{u}$ are discretized using Adams-Bashforth, where $\mathbf{u}^{AB} = \mathbf{u}^n$ in the first time step and $\mathbf{u}^{AB} = 2\mathbf{u}^n - \mathbf{u}^{n-1}$ afterwards. As before, $\Delta t = \alpha\widehat{\Delta t}$ is used to simplify the equations. $\mathbf{u}^v$ is an intermediate estimate of $\mathbf{u}^{n+1}$ using an approximation for pressure, which

is computed in an intermediate implicit solve, and $\mathbf{m}$ is the total density flux detailed in Section 3.3.2. With these, the discretized equations are

$$\frac{\rho^{n+1}\mathbf{u}^* - (\rho\mathbf{u})^{BD}}{\widehat{\Delta t}} + \nabla\cdot\left(\mathbf{m}\otimes\mathbf{u}^{AB}\right) = 0 \tag{3.67}$$

$$\begin{aligned}\frac{\mathbf{u}^{**}-\mathbf{u}^*}{\widehat{\Delta t}} = &-\frac{1}{\rho^{n+1}}\nabla p^n + g + \frac{1}{\rho^{n+1}}\sigma\kappa\nabla(h(\gamma)) + \frac{1}{\rho^{n+1}}\nabla\cdot\left(\mu^{n+1}\left(\nabla\mathbf{u}^{AB}\right)^T\right)\\ &+ \frac{1}{\rho^{n+1}}S_{\mathbf{u}}^{n+1}\end{aligned} \tag{3.68}$$

$$\frac{\mathbf{u}^{v}-\mathbf{u}^{**}}{\widehat{\Delta t}} = \frac{1}{\rho^{n+1}}\nabla\cdot\left(\mu^{n+1}\nabla\mathbf{u}^{v}\right) \tag{3.69}$$

$$\nabla\cdot\left(\frac{1}{\rho^{n+1}}\nabla p'\right) = \frac{\nabla\cdot\mathbf{u}^{v}}{\widehat{\Delta t}} \tag{3.70}$$

$$\frac{\mathbf{u}^{n+1}-\mathbf{u}^{v}}{\widehat{\Delta t}} = -\frac{1}{\rho^{n+1}}\nabla p'. \tag{3.71}$$

Momentum flux

Everything in the Navier-Stokes equations is independent of Cahn-Hilliard except for the density flux term $\mathbf{m}$. We follow Huang et al. [47] and Goulding et al. [33] and give a modification of $\mathbf{m}$ here that is consistent with our new Cahn-Hilliard discretization in Section 3.3.1. Beginning with

$$\frac{\rho^{n+1}-\rho^{BD}}{\widehat{\Delta t}} + \nabla\cdot\mathbf{m} = S_m^{n+1}, \tag{3.72}$$

where $\mathbf{m}$ includes advection and Cahn-Hilliard separation, and S_m takes the effects of the forcing term S_γ, we express $\mathbf{m}$ in terms of γ:

$$\nabla \cdot \mathbf{m} = -\frac{\rho^{n+1} - \rho^{BD}}{\widehat{\Delta t}} + S_m^{n+1} \tag{3.73}$$

$$= -\left(\rho_1 - \rho_0\right) \frac{\gamma^{n+1} - \gamma^{BD}}{\widehat{\Delta t}} + S_m^{n+1} \tag{3.74}$$

$$= -\left(\rho_1 - \rho_0\right) \left(\frac{\gamma^{n+1} - \gamma^*}{\widehat{\Delta t}} + \frac{\gamma^* - \gamma^{BD}}{\widehat{\Delta t}} \right) + S_m^{n+1}. \tag{3.75}$$

Using Equations (3.46), (3.52), (3.54), and (3.55), defining $S_m^{n+1} = \left(\rho_1 - \rho_0\right) S_\gamma^{n+1}$, and canceling terms, this becomes

$$\nabla \cdot \mathbf{m} = \left(\rho_1 - \rho_0\right) \left(\nabla \cdot \left(\mathbf{u}^{AB} \gamma^{AB} \right) - \nabla \cdot \left(s \nabla C + s \nabla A + (M\lambda - as) \nabla F'(\gamma)^{AB} \right) \right). \tag{3.76}$$

As shown in [33], this definition of $\mathbf{m}$ is only well-defined up to a divergence-free shift. We determine the shift in the same way as in that work, by considering the case $\rho_0 = \rho_1$. This leads to the same shift of $\nabla \cdot \left(\rho_0 \mathbf{u}^{AB} \right)$ as in [33], which is consistent with the shift in [47]. We add this divergence-free shift to (3.76):

$$\begin{aligned} \nabla \cdot \mathbf{m} = \nabla \cdot \left(\rho_0 \mathbf{u}^{AB} \right) + \left(\rho_1 - \rho_0\right) \left(\nabla \cdot \left(\mathbf{u}^{AB} \gamma^{AB} \right) - \nabla \cdot \left(s \nabla C + s \nabla A \right. \right. \\ \left. \left. + (M\lambda - as) \nabla F'(\gamma)^{AB} \right) \right). \end{aligned} \tag{3.77}$$

This leads to a definition of

$$\mathbf{m} = \rho_0 \mathbf{u}^{AB} + \left(\rho_1 - \rho_0\right) \left(\mathbf{u}^{AB} \gamma^{AB} - s \nabla C - s \nabla A - (M\lambda - as) \nabla F'(\gamma)^{AB} \right). \tag{3.78}$$

Like in [33], the term $\mathbf{u}^{AB}\gamma^{AB}$ is replaced by the flux computed by the WENO conservative advection described in that work.

3.3.3 Discretization summary

For convenience, we provide a summary of a single step of the full discretized algorithm.

1. At the beginning of the step, the Adams-Bashforth and backwards-difference quantities must be computed from previous data. We compute γ^{BD} and γ^{AB} on cell centers and $(\rho\mathbf{u})^{BD}$ and $\mathbf{u}^{AB}$ on cell faces. First-order time discretizations are used on the first time step:

$$\gamma^{BD} = \gamma^n \qquad \gamma^{AB} = \gamma^n \qquad (\rho\mathbf{u})^{BD} = \rho^n\mathbf{u}^n \qquad \mathbf{u}^{AB} = \mathbf{u}^n \qquad \widehat{\Delta t} = \Delta t. \tag{3.79}$$

   Second-order time discretizations are used on every subsequence time step:

$$\begin{aligned} &\gamma^{BD} = \frac{4}{3}\gamma^n - \frac{1}{3}\gamma^{n-1} \qquad \gamma^{AB} = 2\gamma^n - \gamma^{n-1} \qquad (\rho\mathbf{u})^{BD} = \frac{4}{3}\rho^n\mathbf{u}^n - \frac{1}{3}\rho^{n-1}\mathbf{u}^{n-1} \\ &\mathbf{u}^{AB} = 2\mathbf{u}^n - \mathbf{u}^{n-1} \quad \widehat{\Delta t} = \frac{2}{3}\Delta t. \end{aligned} \tag{3.80}$$

2. We use a conservative scheme as in [33] to compute γ^* from γ^{BD} as

$$\gamma^*_{i,j} = \gamma^{BD}_{i,j} - \widehat{\Delta t}\left(\frac{\mathcal{F}^W_{i+1/2,j} - \mathcal{F}^W_{i-1/2,j}}{\Delta x} + \frac{\mathcal{F}^W_{i,j+1/2} - \mathcal{F}^W_{i,j-1/2}}{\Delta y}\right), \tag{3.81}$$

where the fluxes $\mathcal{F}^W$ are computed with WENO interpolation [50]. These fluxes are also stored for later use in computing the mass flux $\mathbf{m}$.

3. Next, we compute the intermediate term A from γ^* by solving the Helmholtz equation

$$A - s\widehat{\Delta t}\nabla^2 A = \gamma^* - 2\gamma^{AB} + \widehat{\Delta t}M\lambda\nabla^2 F'(\gamma)^{AB} + \widehat{\Delta t}S_\gamma^{n+1}. \tag{3.82}$$

4. We solve the nonlinear equation (3.56) for C by reformulating it as a minimization of the objective function

$$E = \sum_i g\left(C_i\right) - \frac{1}{2}s\widehat{\Delta t}\sum_{i,j} C_i L_{ij} C_j - \sum_i C_i B_i. \tag{3.83}$$

5. The final phase fraction γ^{n+1} is computed from C using g' (defined in (3.34)).

$$\gamma^{n+1} = g'(C), \tag{3.84}$$

6. With the Cahn Hilliard step complete, we begin the Navier-Stokes step. We compute effective densities and viscosities on faces by interpolating γ^{n+1} linearly to faces and then using equations (3.4) and (3.5).

$$\rho_{i+\frac{1}{2},j}^{n+1} = \rho_0 + \left(\rho_1 - \rho_0\right)\gamma_{i+\frac{1}{2},j}^{n+1} \tag{3.85}$$

$$\mu_{i+\frac{1}{2},j}^{n+1} = \mu_0 + \left(\mu_1 - \mu_0\right)\gamma_{i+\frac{1}{2},j}^{n+1}. \tag{3.86}$$

7. Compute the discrete mass flux using the Cahn-Hilliard intermediates A and C,

$$\mathbf{m} = \rho_0 \mathbf{u}^{AB} + (\rho_1 - \rho_0)\left(\mathcal{F}^W - s\nabla C - s\nabla A - (M\lambda - as)\nabla F'(\gamma)^{AB}\right). \tag{3.87}$$

8. Update momentum consistently with the movement of mass from Cahn-Hilliard as in [33]:

$$\rho^{n+1}\mathbf{u}^* = (\rho\mathbf{u})^{BD} - \widehat{\Delta t}\nabla\cdot\left(\mathbf{m}\otimes\mathbf{u}^{AB}\right). \tag{3.88}$$

9. Compute $\mathbf{u}^*$ by dividing off ρ^{n+1}.

10. Apply explicit forces:

$$\begin{aligned}\mathbf{u}^{**} = \mathbf{u}^* + \widehat{\Delta t}\mathbf{g} + \frac{\widehat{\Delta t}}{\rho^{n+1}}\sigma\kappa\nabla(h\left(\gamma^{n+1}\right)) + \frac{\widehat{\Delta t}}{\rho^{n+1}}\nabla\cdot\left(\mu^{n+1}\left(\nabla\mathbf{u}^{AB}\right)^T\right) - \frac{\widehat{\Delta t}}{\rho^{n+1}}\nabla p^n \\ + \widehat{\Delta t}S_{\mathbf{u}}^{n+1}\end{aligned} \tag{3.89}$$

Surface tension is descritized as in [33].

$$\kappa = -\nabla \cdot \left(\frac{\nabla \gamma}{\|\nabla \gamma\|} \right) \tag{3.90}$$

$$h(\gamma) = \begin{cases} 1, & \text{if } \gamma \geq 1 - a \\ 0, & \text{if } \gamma < a \\ \frac{(-\gamma+a)^2(2\gamma+4a-3)}{(2a-1)^3}, & \text{otherwise} \end{cases} \tag{3.91}$$

$$a = 0.2 \tag{3.92}$$

The viscosity term is discretized consistently as in [47].

11. Solve the Helmholtz equation to apply the implicit portion of viscosity

$$\mathbf{u}^v - \frac{\widehat{\Delta t}}{\rho^{n+1}} \nabla \cdot \left(\mu^{n+1} \nabla \mathbf{u}^v \right) = \mathbf{u}^{**}. \tag{3.93}$$

12. Solve the Poisson equation for the pressure correction, and update the pressure:

$$\nabla \cdot \left(\frac{\widehat{\Delta t}}{\rho^{n+1}} \nabla p' \right) = \nabla \cdot \mathbf{u}^v \tag{3.94}$$

$$p^{n+1} = p^n + p', \tag{3.95}$$

13. Project $\mathbf{u}^{n+1}$ to be divergence free by applying the pressure correction:

$$\mathbf{u}^{n+1} = \mathbf{u}^v - \frac{\widehat{\Delta t}}{\rho^{n+1}} \nabla p'. \tag{3.96}$$

3.4 Numerical examples

We demonstrate the numerical properties of our scheme through a series of numerical tests. All the units in the following tests are SI units.

3.4.1 Manufactured solution

We test our discrete solvers using a manufactured solution for γ, $\mathbf{u}$, and p. Accuracy is measured by comparing the final simulated state against the manufactured solution. The source terms that enforce the manufactured solution are

$$S_\gamma = \frac{\partial \gamma}{\partial t} + \nabla \cdot (\mathbf{u}\gamma) - \nabla \cdot (M \nabla \xi) \tag{3.97}$$

$$S_{\mathbf{u}} = \frac{\partial \rho \mathbf{u}}{\partial t} + \nabla \cdot (\mathbf{m} \otimes \mathbf{u}) + \nabla p - \rho g - \sigma \kappa \nabla (h(\gamma)) - \nabla \cdot \left(\mu \left(\nabla \mathbf{u} + (\nabla \mathbf{u})^T \right) \right). \tag{3.98}$$

The accuracy of the Cahn-Hilliard solver is tested alone, then the Navier-Stokes solver is added for a second test of the full system. We also perform two additional tests to show that changes in r and b do not affect the accuracy of our solver. The parameters used follow the similar tests in [47] and [33]. All tests use a $[-\pi, \pi]^2$ domain and end at $t = 1$, with time step of $\Delta t = 0.08/N$ and cell size $\Delta x = 2\pi/N$. Fluid phase density is set to be $\rho_0 = 1$ and $\rho_1 = 3$ with viscosity constants $\mu_0 = 0.01$ and $\mu_1 = 0.02$. Unless otherwise noted, the Cahn-Hilliard parameters used in these tests are $M = 0.001$, $\lambda = 0.001$, $\eta = 0.1$, $r = 0.1$, and $b = 0.01$.

Table 3.1: At larger N, our Cahn-Hilliard scheme shows second order convergence at $t = 1$.

	$r = 0.1$				$r = 0.05$				$r = 0.01$			
N	L_2		L_∞		L_2		L_∞		L_2		L_∞	
8	1.28e-05		2.12e-05		1.28e-05		2.09e-05		1.27e-05		2.07e-05	
16	6.25e-06	1.04	1.27e-05	0.74	6.31e-06	1.02	1.27e-05	0.72	6.30e-06	1.01	1.27e-05	0.70
32	3.84e-06	0.70	1.22e-05	0.05	3.85e-06	0.71	1.22e-05	0.05	3.85e-06	0.71	1.23e-05	0.05
64	2.49e-06	0.63	1.14e-05	0.10	2.49e-06	0.62	1.15e-05	0.10	2.50e-06	0.62	1.15e-05	0.09
128	8.64e-07	1.52	4.85e-06	1.23	8.71e-07	1.52	4.90e-06	1.23	8.76e-07	1.51	4.94e-06	1.22
256	1.85e-07	2.22	1.05e-06	2.21	1.86e-07	2.22	1.05e-06	2.22	1.87e-07	2.22	1.06e-06	2.22
512	4.45e-08	2.05	2.55e-07	2.04	4.48e-08	2.06	2.57e-07	2.04	4.51e-08	2.06	2.59e-07	2.04

Cahn-Hilliard solver

To assess the convergence of the Cahn-Hilliard solver alone, we use the solution

$$\gamma(x, y, t) = \frac{1}{2} + \frac{10}{21} \cos(x) \cos(y) \left(1 - \sin(t)\right). \tag{3.99}$$

This solution is chosen such that $\mathbf{n} \cdot \nabla\gamma = 0$ and $\gamma \in (0, 1)$ within the time tested. We omit the Navier-Stokes update for this test and set $u = v = 0$. The initial conditions are set using the manufactured solution for $t = 0$. We refine N from 8 to 512 and use the L_2 and L_∞ errors at each level of refinement to measure the convergence rate. Table 3.1 shows that our Cahn-Hilliard solver exhibits second order convergence.

Cahn-Hilliard-Navier-Stokes solver

In this test, we repeat the test in Section 3.4.1 with the same solution for γ but this time with the coupled Cahn-Hilliard-Navier-Stokes solver and nonzero solutions for u,

Table 3.2: The coupled Cahn-Hilliard-Navier-Stokes scheme shows second order convergence at $t = 1$.

	γ				u				v				p			
N	L_2		L_∞		L_2		L_∞		L_2		L_∞		L_2		L_∞	
8	1.77e-02		3.39e-02		5.52e-02		1.35e-01		1.74e-02		4.50e-02		2.03e-02		4.64e-02	
16	2.98e-03	2.57	9.28e-03	1.87	1.23e-02	2.17	3.18e-02	2.08	3.43e-03	2.34	8.74e-03	2.36	4.01e-03	2.34	1.32e-02	1.82
32	5.68e-04	2.39	1.42e-03	2.71	3.04e-03	2.02	8.43e-03	1.92	7.64e-04	2.17	2.55e-03	1.78	8.43e-04	2.25	2.48e-03	2.41
64	1.39e-04	2.03	3.41e-04	2.06	7.59e-04	2.00	2.14e-03	1.97	1.88e-04	2.02	6.24e-04	2.03	2.10e-04	2.01	6.40e-04	1.95
128	3.49e-05	2.00	8.89e-05	1.94	1.91e-04	1.99	5.34e-04	2.01	4.81e-05	1.97	1.61e-04	1.96	5.49e-05	1.93	1.60e-04	2.00
256	8.77e-06	1.99	2.31e-05	1.94	4.82e-05	1.98	1.31e-04	2.02	1.36e-05	1.83	4.40e-05	1.87	1.57e-05	1.80	4.68e-05	1.77

v, and p:

$$u(x, y, t) = \sin(x)\cos(y)\cos(t) \tag{3.100}$$

$$v(x, y, t) = -\cos(x)\sin(y)\cos(t) \tag{3.101}$$

$$p(x, y, t) = \cos(x)\cos(y)\sin(t), \tag{3.102}$$

which are the same solutions used in [47] and [33]. These solutions provide a divergence-free velocity field throughout the test. We set gravity to $g = \langle 1, -2 \rangle$. The manufactured solutions are used to set the initial and boundary conditions. As in Section 3.4.1, N is refined from 8 to 256. The L_2 and L_∞ error is measured for γ, $\mathbf{u}$, and p at each level of refinement and used to measure the convergence rate. Second order convergence is observed in all quantities as shown in Table 3.2.

Varying b

Our time integration scheme includes one free parameter b. The convergence rate of the scheme is independent of this parameter, though the parameter is bounded by the restriction $0 < q < 1$ as noted in Section 3.3.1. To evaluate the effects of the constant b on the accuracy of the coupled Cahn-Hilliard and Navier-Stokes solvers, we fix $N = 128$

Table 3.3: L_2 and L_∞ errors in γ for varying values of q.

q	b	L_2	L_∞
9.90e-01	1.32e+01	3.62e-05	9.11e-05
9.00e-01	1.20e+01	3.60e-05	9.05e-05
8.00e-01	1.07e+01	3.57e-05	8.99e-05
7.00e-01	9.33e+00	3.54e-05	8.93e-05
6.00e-01	8.00e+00	3.52e-05	8.89e-05
5.00e-01	6.67e+00	3.51e-05	8.85e-05
4.00e-01	5.33e+00	3.49e-05	8.84e-05
3.00e-01	4.00e+00	3.49e-05	8.83e-05
2.00e-01	2.67e+00	3.48e-05	8.84e-05
1.00e-01	1.33e+00	3.48e-05	8.86e-05
1.00e-02	1.33e-01	3.49e-05	8.89e-05
1.00e-03	1.33e-02	3.49e-05	8.89e-05
1.00e-04	1.33e-03	3.49e-05	8.89e-05
1.00e-05	1.33e-04	3.49e-05	8.89e-05
1.00e-06	1.33e-05	3.49e-05	8.89e-05

and instead vary b (or equivalently, q). We use the same manufactured solutions as in the previous tests. Table 3.3 shows that the solver accuracy (represented by the L_2 and L_∞ error of γ) is insensitive to the choice of b. Although accuracy is not appreciably affected by b, we observe that the scheme is more stable when b is large. This is somewhat expected, since the strength of the barrier is proportional to b, as one observes in (3.25) and (3.26). Indeed, if $b = 0$, the barrier is lost, and (3.25) reduces to a linear Helmholtz equation. Unless otherwise indicated, we run with $b = 0.01$ in all of our numerical examples, except when this would result in $q > 0.5$; in this case, we compute b so that $q = 0.5$.

Varying r

Our formulation of the potential F includes an extra free parameter r, which is the minimum of the double-well potential. In this test, we evaluate the effects of r on the accuracy of our solver. We test the coupled Cahn-Hilliard Navier-Stokes solver with two

different manufactured solutions for γ over a range of values for r. The first solution is the same as in the previous manufactured solution tests,

$$\gamma_1(x, y, t) = \frac{1}{2} + \frac{10}{21}\cos(x)\cos(y)(1 - \sin(t)). \tag{3.103}$$

This solution has $\gamma \in [\frac{1}{42}, 1 - \frac{1}{42}]$, which means that as r becomes very small the barrier portion of F outside the minima will never be used. To account for this, we repeat this test using the second manufactured solution

$$\gamma_2(x, y, t) = \frac{1}{2}(1 - r)\left(1 + \cos(\frac{x}{2} + \frac{\pi}{2})\cos(\frac{y}{2} + \frac{\pi}{2})\right) + \frac{r}{2}. \tag{3.104}$$

so that $\gamma \in [\frac{r}{2}, 1 - \frac{r}{2}]$ extends into the tails of F. The following solutions for $\mathbf{u}$ and p are used in both cases:

$$u(x, y, t) = \sin(x)\cos(y)\cos(t) \tag{3.105}$$

$$v(x, y, t) = -\cos(x)\sin(y)\cos(t) \tag{3.106}$$

$$p(x, y, t) = \cos(x)\cos(y)\sin(t). \tag{3.107}$$

We fix $N = 128$ and vary r, as shown in Table 3.4. We observe that varying r does not strongly affect the accuracy, especially when r is small. This is consistent with the observation that F converges pointwise in the limit $r \to 0$, as can be seen in Figure 3.3. The barrier portion of the F becomes extremely sharp in this limit. Unlike traditional barrier methods, the sharpness of the barrier only weakly affects the performance of the

Table 3.4: Analysis of manufactured solution error dependence on values of r.

(a) L_2 and L_∞ error for γ_1 at varying r values.

r	L_2	L_∞
4.00e-01	3.48e-05	8.88e-05
3.00e-01	3.49e-05	8.89e-05
2.00e-01	3.49e-05	8.89e-05
1.00e-01	3.49e-05	8.89e-05
1.00e-02	3.49e-05	8.89e-05
1.00e-03	3.49e-05	8.89e-05
1.00e-04	3.49e-05	8.89e-05
1.00e-05	3.49e-05	8.89e-05
1.00e-06	3.49e-05	8.89e-05

(b) L_2 and L_∞ error for γ_2 at varying r values.

r	L_2	L_∞
4.00e-01	1.33e-05	3.54e-05
3.00e-01	1.57e-05	4.32e-05
2.00e-01	1.81e-05	5.18e-05
1.00e-01	2.05e-05	6.13e-05
1.00e-02	2.28e-05	7.08e-05
1.00e-03	2.30e-05	7.18e-05
1.00e-04	2.31e-05	7.19e-05
1.00e-05	2.31e-05	7.19e-05
1.00e-06	2.31e-05	7.19e-05

method; although $F(\gamma)$ has a sharp barrier in the limits $\gamma \to 0$ and $\gamma \to 1$, $F(g'(C))$ only grows gradually as C approaches infinity. We do sometimes observe numerical difficulties when r is extremely small (below 10^{-4}). Unless otherwise specified, we run all of our tests with $r = 0.01$.

3.4.2 Binary separation of phases

We demonstrate fluid phase separation over time using a random initial γ distribution. No forces are calculated during this simulation and there is no γ source term. This test uses the same parameters as [33] and [43]. The domain is $[0, 2\pi]^2$ with periodic boundaries. The initial distribution is uniformly random in the range $[0.475, 0.575]$. The time step size is $\Delta t = 0.0001$ and the cell size is $\Delta x = 1/512$. The test runs until $t = 5$. The Cahn-Hilliard parameters are chosen to satisfy $ML = \eta^2 = 0.001$ with $\sigma = 1$. Figure 3.6 depicts the test results in several snapshots from $t = 0$ to $t = 5$. These snapshots are qualitatively similar to the results shown in [43], with increasing phase separation over time.

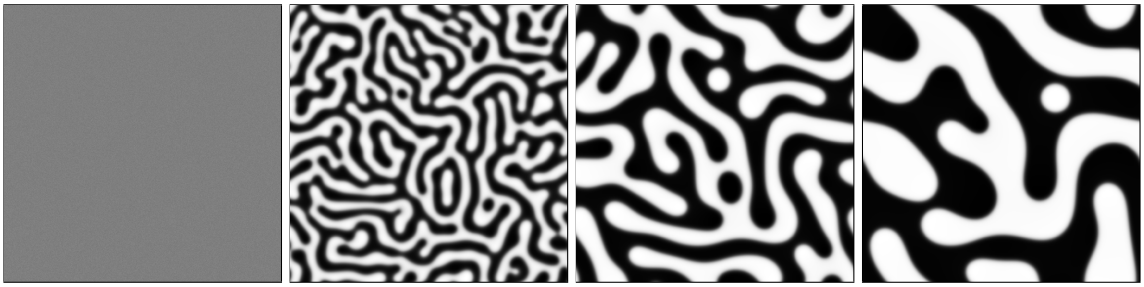

(a) $t = 0$ (b) $t = 0.1$ (c) $t = 1$ (d) $t = 5$

Figure 3.6: Snapshots of phase separation over time.

3.4.3 Stationary circle

We test the balance between pressure and surface tension forces by simulating a stationary circle of fluid. We take the test parameters from [47] and [33]. We measure the final velocity of the simulation to determine the magnitude of the spurious currents caused by force imbalance. We test 5 cases with differing density ratios, surface tension, and viscosity, and show how each case changes under refinement.

We use a $[0, 1]^2$ domain with free-slip boundary conditions and cell size $\Delta x = 1/N$. The test runs until $t = 10$ in time steps of $\Delta t = 0.064/N$. For each case we refine from $N = 16$ to $N = 256$. The circle of fluid is initialized at $(0.5, 0.5)$ with radius $r = 0.2$ and density $\rho_1 = 1000$. The viscosity of the circle differs depending on test case. The surrounding fluid varies in density and viscosity for each test case, and both fluids begin with no initial velocity. Table 3.5 lists the density, viscosity, and surface tension parameters for each case.

Following [47] and [33], we narrow the interface width η with refinement to show convergence to a sharp interface solution:

$$\eta = \eta_0 \left(\frac{\Delta x}{h_0} \right)^{X^\eta} = \eta_0 (N h_0)^{-X^\eta} \tag{3.108}$$

$$M = M_0 \left(\frac{\eta}{\eta_0} \right)^{X^M} = \frac{M_0}{N h_0} \tag{3.109}$$

$$\eta_0 = h_0 = \frac{1}{32} \qquad M_0 = 10^{-5} \qquad X^\eta = \frac{2}{3} \qquad X^M = \frac{3}{2}. \tag{3.110}$$

As in [47] and [33], we average the final velocity to cell centers and compare the magnitude $\|\mathbf{u}\|_2$ with the ideal value of 0. We compute the L_2 and L_∞ error and plot the change under refinement compared to the ideal first and second order case in Figure 3.7. Figure 3.7b shows that L_2 decreases with first order whenever viscosity is nonzero, though no improvement is observed in L_∞. That is, the maximum magnitude of velocity error does not change much, but the region over which this error occurs shrinks.

We note that the test above is not a proper convergence test, since the coefficients of the PDE are changing under refinement. As such, it is difficult to determine whether the problems observed are a consequence of the sharpening interface or a fundamental problem with the underlying scheme. To determine whether the proposed method is converging properly on this test, we hold the PDE fixed and perform a proper refinement study. We fix $\eta = 0.02$ and $M = 10^{-6}$. The results are shown in Figure 3.8, where we observe second order convergence in L_2 and convergence ranging from first to second order in L_∞.

From these tests, we conclude that the method converges but is somewhat sensitive to the sharpness of the interface. We suspect that this is related to the smoothness of

Table 3.5: Material parameters for the five tested stationary circle cases.

Case ID	ρ_0	ρ_1	μ_0	μ_1	σ
Case 1	1000	1000	0	0	1
Case 2	1000	1000	0.1	0.1	1
Case 3	1	1000	0.1	0.1	1
Case 4	1000	1000	0.0001	0.1	1
Case 5	1000	1000	0.1	0.1	10

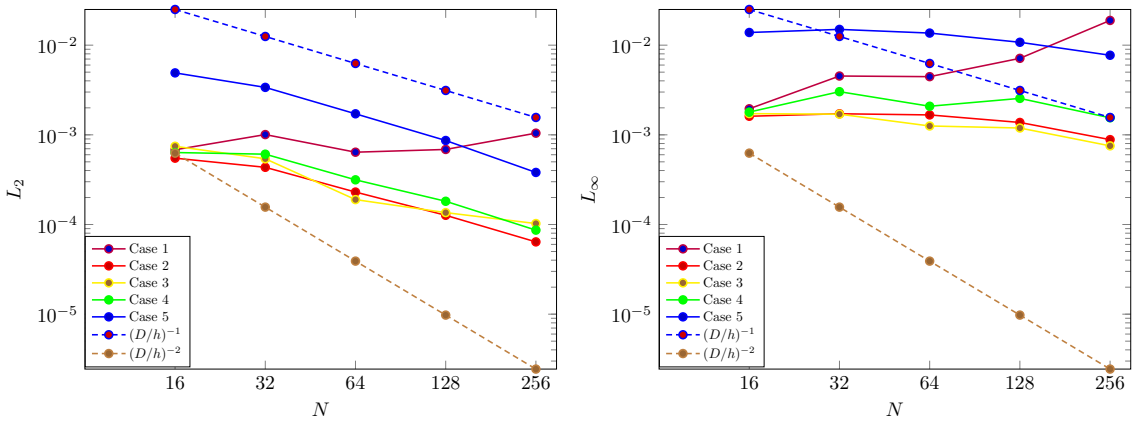

(a) L_2 error

(b) L_∞ error

Figure 3.7: The magnitude of the spurious velocity for the five stationary circle cases at different resolutions.

the Cahn-Hilliard potential. The potential function F is C^3 continuous everywhere except at $\gamma = \frac{1}{2}$, where it is only C^2 continuous. This suffices to produce a continuous Hessian. However, the time integration scheme includes terms of the general form $\nabla^2 F'(\gamma)$, which when expanded out depend on the third derivative of F. This may introduce small discontinuities in the numerical scheme near the interface, which surface tension is particularly sensitive to.

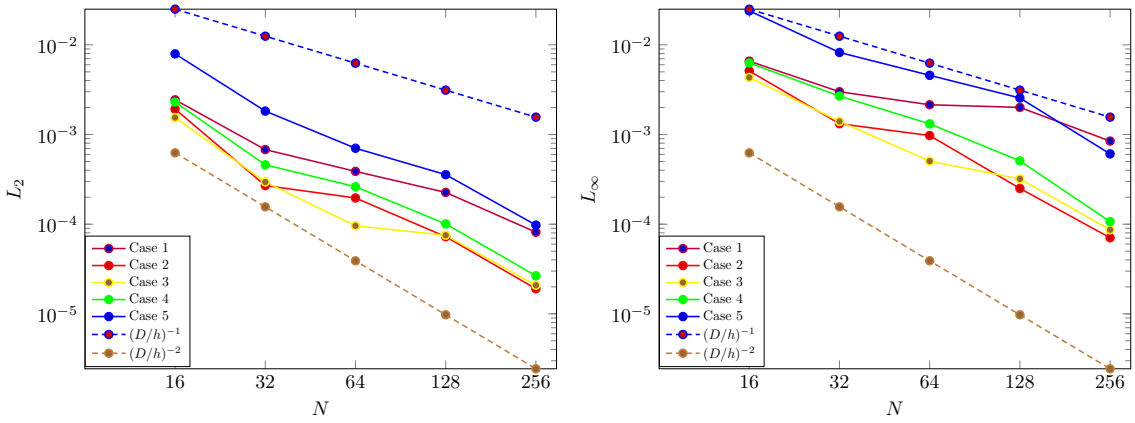

(a) L_2 error

(b) L_∞ error

Figure 3.8: The magnitude of the spurious velocity for the five stationary circle cases with fixed interface width.

3.4.4 Horizontal shear

We examine conservation of mass, conservation of momentum, and change in kinetic energy in a shearing advection test. Four cases with different density ratios and viscosities show the effects of these parameters on the test quantities. Surface tension and gravity are not used in this test.

The test setup is taken from [47] and [33]. The domain has periodic boundary conditions on all sides and has a range of $[0, 1]^2$. The time step size is $\Delta t = 0.0005$ and the tests run until $t = 1$. The cell size is $\Delta x = 1/128$. The surface tension constant is set to $\sigma = 10^{-12}$, leading to negligible surface tension forces, and $M = 10^{-7}$. The initial γ

distribution is

$$\gamma(x,y,0) = \begin{cases} \frac{1}{2}\left(1+\tanh\left(\frac{y-y_1}{\delta_1}\right)\right), & \text{if } y \leq y_0 \\ \frac{1}{2}\left(1+\tanh\left(\frac{y_2-y}{\delta_1}\right)\right), & \text{if } y > y_0 \end{cases} \tag{3.111}$$

$$y_0 = 0.5 \qquad y_1 = 0.25 \qquad y_2 = 0.75 \qquad \delta_1 = 1/30, \tag{3.112}$$

with $\eta = \delta_1/\sqrt{2}$. The shearing velocity is

$$u(x,y,0) = \begin{cases} \tanh\left(\frac{y-y_1}{\delta_1}\right), & \text{if } y \leq y_0 \\ \tanh\left(\frac{y_2-y}{\delta_1}\right), & \text{if } y > y_0 \end{cases} \tag{3.113}$$

$$v(x,y,0) = \delta_2 \sin(kx) \tag{3.114}$$

$$\delta_2 = 0.5 \qquad k = 2\pi. \tag{3.115}$$

These functions initialize fluid 1 with velocity in the postive x direction, located as a center band in the domain. Fluid 0 has a velocity in the negative x direction, and is located everywhere else. This distribution has a strong velocity gradient in the transition

Table 3.6: Material parameters for the four tested horizontal shear cases.

Case ID	ρ_0	ρ_1	μ_0	μ_1
Case 1	1	1	0	0
Case 2	1	10	0	0
Case 3	1	1	0.001	0.01
Case 4	1	10	0.001	0.01

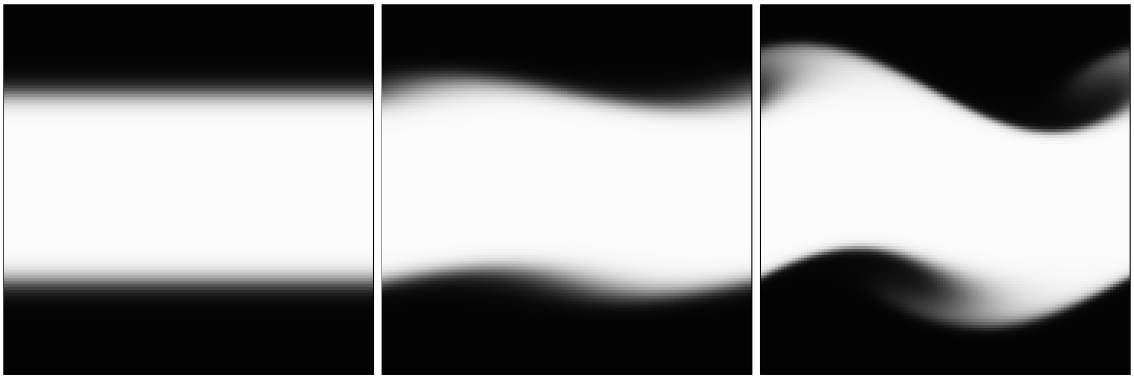

(a) $t = 0$ (b) $t = 0.5$ (c) $t = 1$

Figure 3.9: Example of Horizontal Shear (Case 3).

region between the fluids. Table 3.6 lists the variable parameters for the four different cases tested.

Following [33], we measured the change in total mass, total momentum, and kinetic energy using

$$m_{\text{total}} = \sum_{i,j} \left(\rho_0 + (\rho_1 - \rho_0)\,\gamma_{i,j}\right) \Delta x^2 \tag{3.116}$$

$$(m\mathbf{u})^x_{\text{total}} = \sum_{i,j} \left(\rho_{i-1/2,j}\right) \left(u_{i-1/2,j}\right) \Delta x^2 \tag{3.117}$$

$$E_k = \frac{1}{2} \sum_{i,j} \left(\left(\rho_{i-1/2,j}\right) \left(u_{i-1/2,j}\right)^2 + \left(\rho_{i,j-1/2}\right) \left(v_{i,j-1/2}\right)^2 \right) \Delta x^2, \tag{3.118}$$

with the y-axis momentum computed analogously to the x-axis. In the absence of surface tension and external forces, kinetic energy should only decrease in the viscous cases 3 and 4, and otherwise remain unchanged. In all four cases, momentum and mass should be conserved.

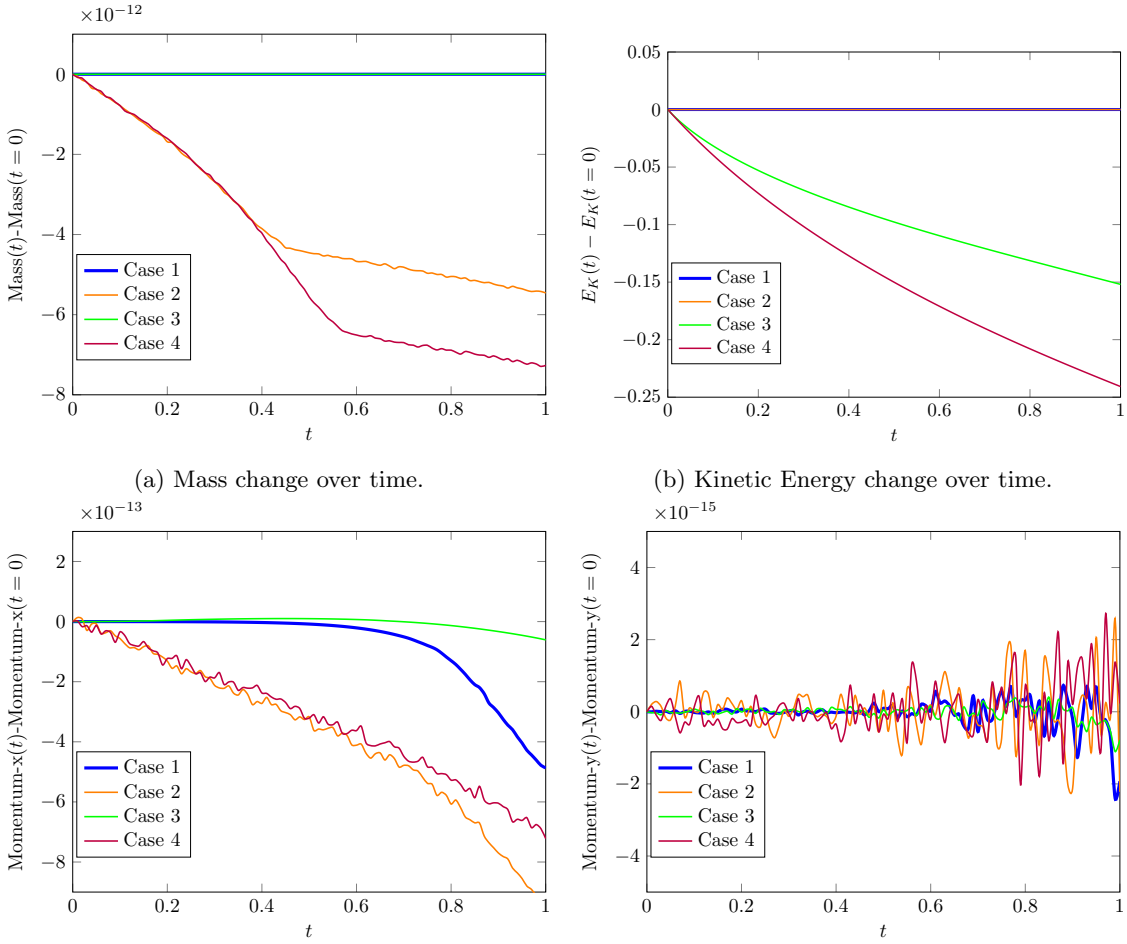

(a) Mass change over time.

(b) Kinetic Energy change over time.

(c) Momentum (x axis) change over time.

(d) Momentum (y axis) change over time.

Figure 3.10: Conservation results for the four horizontal shear cases.

We plot the change in quantities ove time in Figure 3.10. In cases 1 and 3, where the fluids have matched densities, the density is constant throughout the domain and so mass is exactly conserved. In the other cases, there is a small change over time due to solver inaccuracies. Kinetic energy is conserved as expected in the inciscid cases 1 and 2, and declines due to viscosity in the remaining two cases. Momentum remains essentially unchanged in the y-axis, but we see a small negative trend over time in the x-axis. This change is on the order of our solver tolerances.

Table 3.7: Material parameters for the eight translating circle cases.

Case ID	ρ_0	ρ_1	σ
Case 1	1	1	10^{-12}
Case 2	1	10^3	10^{-12}
Case 3	1	10^6	10^{-12}
Case 4	1	10^9	10^{-12}
Case 5	1	1	1
Case 6	1	10^3	1
Case 7	1	10^6	1
Case 8	1	10^9	1

3.4.5 Translating circle

Based on the same test in [47] and [33], we test the accuracy of our coupled Cahn-Hilliard method with momentum advection. A drop of fluid 1 with radius 0.1 centered in the $[0,1]^2$ domain is advected periodically with initial velocity $\langle 1,1\rangle$ in the whole domain. We use cell size $\Delta x = 1/128$ and take time steps of $\Delta t = \Delta x/10$ until the simulation ends at time $t = 1$. The drop is expected to complete one full revolution and return to its initial position. The Cahn-Hilliard parameters are set as $M = 10^{-7}$ and $\eta = 3\Delta x$. We test with different densities for the fluid 1, ranging from $\rho_1 = 1$ to $\rho_1 = 10^9$. Fluid 0 has density $\rho_0 = 1$ in all cases. The resulting large density ratios demonstrate the robustness of our momentum conservation through advection. We do not test with viscosity or gravity. The tests are run twice, once with the surface tension constant $\sigma = 10^{-12}$, giving negligible surface tension force, and the the second time with $\sigma = 1$. The full set of cases are listed in Table 3.7.

To evaluate the results of the test, we illustrate change in the velocity field as well as the shape of the drop. Ideally, the velocity field does not change from its initial $\langle 1,1\rangle$ values and the drop retains its circular shape. We measure the L_2 and L_∞ error in

Table 3.8: Velocity error for the four translating circle cases without surface tension (1–4).

Variable	Norm	$\rho_1/\rho_0 = 1$	$\rho_1/\rho_0 = 10^3$	$\rho_1/\rho_0 = 10^6$	$\rho_1/\rho_0 = 10^9$
u	L_2	8.73e-13	2.70e-13	2.92e-13	2.89e-13
	L_∞	7.33e-12	7.83e-13	8.76e-13	8.93e-13
v	L_2	8.73e-13	2.70e-13	2.92e-13	2.89e-13
	L_∞	7.33e-12	7.83e-13	8.76e-13	8.93e-13

Table 3.9: Velocity error for the four translating circle cases with surface tension (5–8).

Variable	Norm	$\rho_1/\rho_0 = 1$	$\rho_1/\rho_0 = 10^3$	$\rho_1/\rho_0 = 10^6$	$\rho_1/\rho_0 = 10^9$
u	L_2	7.87e-04	7.03e-06	7.35e-09	1.43e-10
	L_∞	6.36e-03	4.53e-05	4.77e-08	1.49e-09
v	L_2	7.87e-04	7.03e-06	7.35e-09	1.43e-10
	L_∞	6.36e-03	4.53e-05	4.77e-08	1.49e-09

the velocity against its ideal values at the end of the simulation ($t = 1$). Figures 3.11 and Figure 3.12 depict the final state of the velocity field as staggered streamlines as well as the initial and final shape of the bubble. We see that in all cases the velocity streamlines remain straight and the shape of the drop is preserved.

Table 3.8 lists the measured error in the velocity field for the cases without surface tension. The velocity experiences negligible change at all density ratios. Table 3.9 lists the same measurements for the cases with surface tension. In this subset of cases, we see that there is more error in the velocity field, but this error decreases as the density ratio increases. In all cases, the measured error is at least as small as the results reported in [47] and [33].

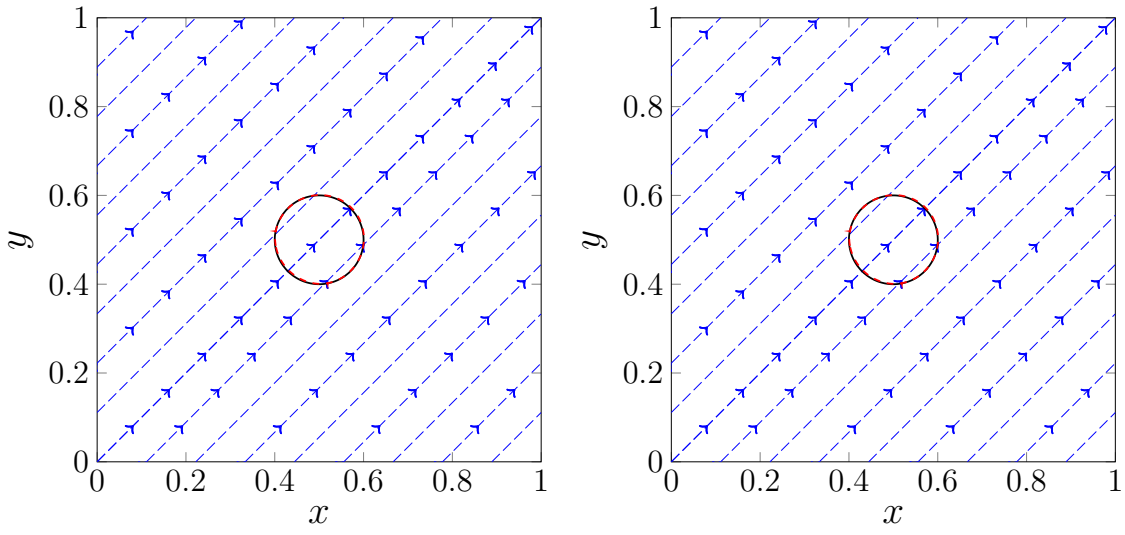

(a) $\rho_1/\rho_0 = 1$

(b) $\rho_1/\rho_0 = 10^3$

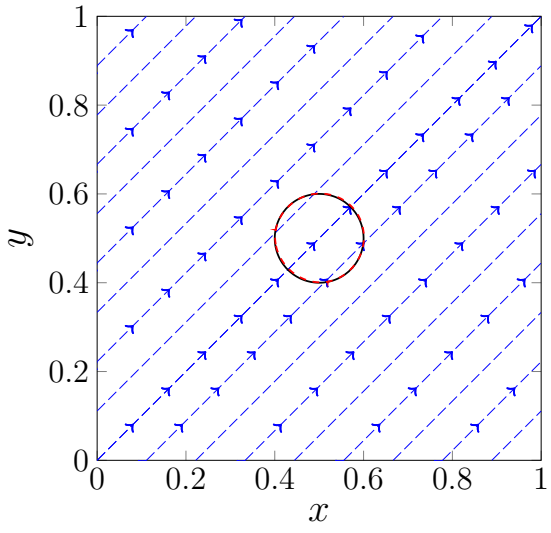

(c) $\rho_1/\rho_0 = 10^6$

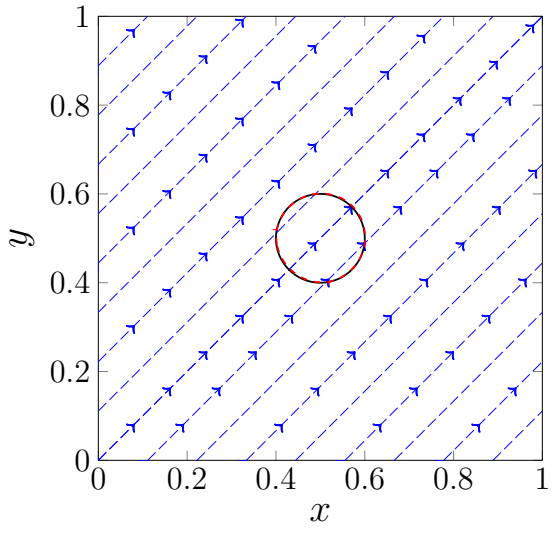

(d) $\rho_1/\rho_0 = 10^9$

Figure 3.11: The initial state of the translating circle (Cases 1–4) is represented by the solid black line. The final ($t = 1$) state is represented by the dashed red line. The blue dashed arrows represent the velocity streamlines at $t = 1$.

3.4.6 Rising air bubble

We perform the rising air bubble test from [47] and [33] to examine how our scheme converges toward a sharp interface solution. We test 6 different ways of coupling

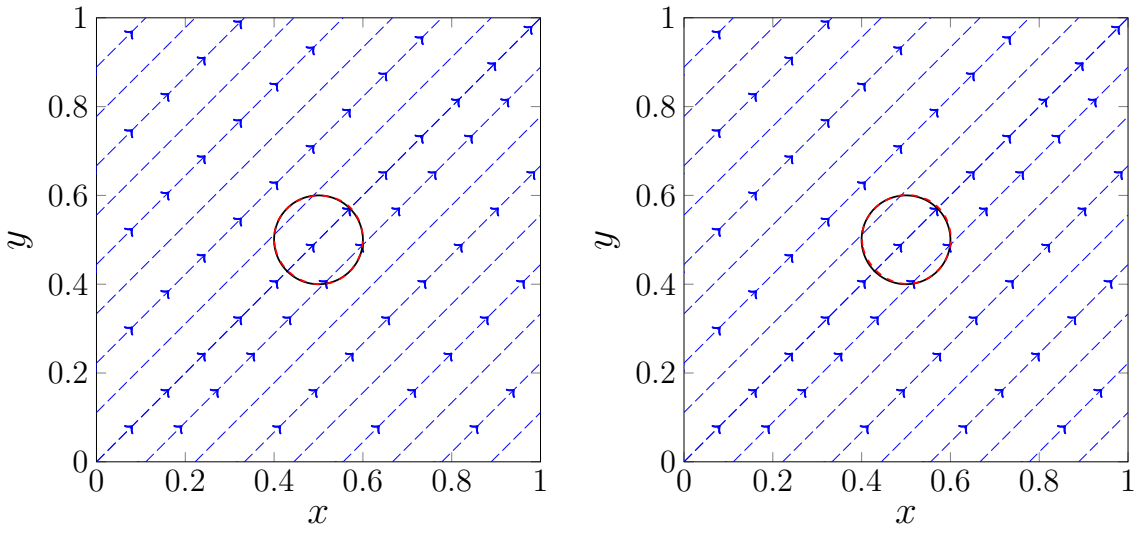

(a) $\rho_1/\rho_0 = 1$

(b) $\rho_1/\rho_0 = 10^3$

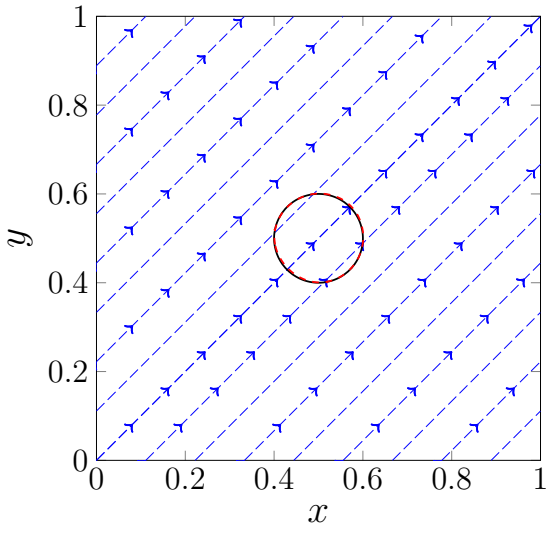

(c) $\rho_1/\rho_0 = 10^6$

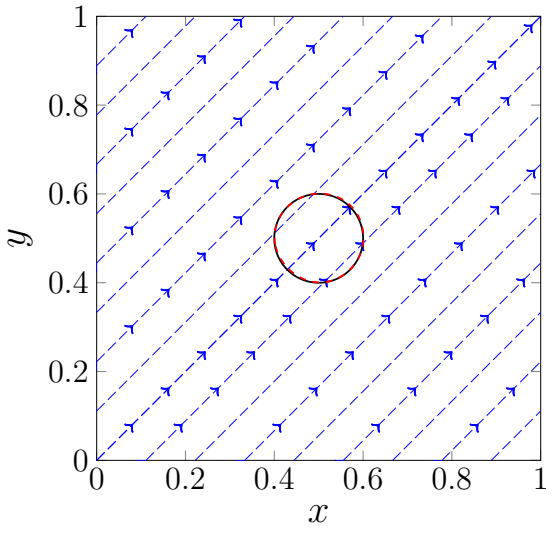

(d) $\rho_1/\rho_0 = 10^9$

Figure 3.12: The initial state of the translating circle (Cases 5–8) is represented by the solid black line. The final ($t = 1$) state is represented by the dashed red line. The blue dashed arrows represent the velocity streamlines at $t = 1$.

the interface width parameter η to the resolution N and evaluate the results by measuring the circularity, center of mass, and rising velocity of a bubble surrounded by denser fluid.

We use a $[0, 1] \times [0, 2]$ domain with no-slip boundary conditions on the top and bottom edges and slip boundary conditions on the left and right edges. The cells are

square with edge length $\Delta x = 1/N$. A circle of fluid 0 with diameter 0.5, density $\rho_0 = 1$, and viscosity $\mu_0 = 0.1$ begins centered at position $(0.5, 0.5)$. The surrounding fluid 1 has properties $\rho_1 = 1000$ and $\mu_1 = 10$. Gravity is set as $\langle 0, -0.98 \rangle$, and $\sigma = 1.96$. The fluid begins at rest, and the simulation runs until $t = 1$ with time step $\Delta t = 0.128/N$.

To couple η with N we use the following definitions from [47]:

$$\eta = \eta_0 (N h_0)^{-X_\eta} \tag{3.119}$$

$$M = M_0 (\eta/\eta_0)^{X_M}, \tag{3.120}$$

where $\eta_0 = h_0 = 1/32$ and $M_0 = 10^{-7}$. X_η and X_M are varied over the 6 different test cases, and we limit them with $X_\eta \leq 1$ based on [47] and $1 \leq X_M < 2$ from [49]. Each of the 6 test cases is refined from $N = 16$ to $N = 256$. For 5 of the tests we test the effects of varying X_η by fixing $X_M = 1$ and varying X_η in the range $[0, 1]$. In the final test, we increase X_M to $3/2$ and use $X_\eta = 2/3$, which keeps M proportional to Δx.

To measure the circularity (ψ_c), center of mass (y_c), and rising velocity (v_c), we use the methods from [47]:

$$\psi_c = \frac{P_a}{P_b} = \frac{2\sqrt{\int_{\gamma < \frac{1}{2}} \pi \, d\Omega}}{P_b} \tag{3.121}$$

$$y_c = \frac{\int_\Omega y(1-\gamma) d\Omega}{\int_\Omega (1-\gamma) d\Omega} \tag{3.122}$$

$$v_c = \frac{\int_\Omega v(1-\gamma) d\Omega}{\int_\Omega (1-\gamma) d\Omega}, \tag{3.123}$$

with P_a is the perimeter of a reference circle the same area as the bubble and P_b is the perimeter of the bubble itself. Based on this ratio, when $\psi_c = 1$ the bubble is perfectly

	Grid	$X_\eta = 0, X_M = 1$		$X_\eta = \frac{1}{3}, X_M = 1$		$X_\eta = \frac{1}{2}, X_M = 1$		$X_\eta = \frac{2}{3}, X_M = 1$		$X_\eta = \frac{2}{3}, X_M = \frac{3}{2}$		$X_\eta = 1, X_M = 1$	
		L_2		L_2		L_2		L_2		L_2		L_2	
ψ_c	16	4.91e-03		9.38e-03		1.14e-02		1.39e-02		1.38e-02		2.00e-02	
	32	1.61e-03	1.61	2.30e-03	2.03	2.78e-03	2.04	3.08e-03	2.17	3.06e-03	2.17	3.22e-03	2.64
	64	7.83e-04	1.04	8.71e-04	1.40	7.92e-04	2.04	7.22e-04	2.09	7.27e-04	2.08	8.61e-04	1.90
	128	3.02e-04	1.38	3.32e-04	1.39	2.83e-04	1.48	3.51e-04	1.04	3.66e-04	0.99	5.57e-04	0.63
		L_2		L_2		L_2		L_2		L_2		L_2	
y_c	16	7.80e-03		1.38e-02		1.58e-02		1.79e-02		1.79e-02		2.33e-02	
	32	2.01e-03	1.96	5.95e-03	1.21	6.60e-03	1.26	6.88e-03	1.38	6.87e-03	1.38	6.96e-03	1.74
	64	4.53e-04	2.15	2.60e-03	1.19	2.63e-03	1.26	2.43e-03	1.50	2.42e-03	1.50	1.88e-03	1.89
	128	9.74e-05	2.22	9.51e-04	1.45	8.64e-04	1.61	7.09e-04	1.78	7.01e-04	1.79	4.25e-04	2.14
		L_2		L_2		L_2		L_2		L_2		L_2	
v_c	16	1.34e-02		1.98e-02		2.20e-02		2.43e-02		2.43e-02		3.05e-02	
	32	4.48e-03	1.58	8.53e-03	1.21	9.19e-03	1.26	9.40e-03	1.37	9.38e-03	1.37	9.42e-03	1.69
	64	1.42e-03	1.66	3.64e-03	1.23	3.64e-03	1.26	3.34e-03	1.50	3.31e-03	1.50	2.65e-03	1.83
	128	3.00e-04	2.24	1.28e-03	1.50	1.20e-03	1.60	9.91e-04	1.75	9.70e-04	1.77	6.42e-04	2.04

Table 3.10: Rising air bubble test convergence results, using a comparison of simulations with $N = 16$ through $N = 128$ to corresponding simulations with $N = 256$.

circular, and $\psi_c < 1$ will decrease as the bubble deforms. We compute P_b using the same method as [33].

We compare the measured values against the $N = 256$, using the L_2 error to measure the rate at which the test is converging to a solution. Table 3.10 details the error and convergence rate for each case. Our results are comparable to those reported in [47] and [33]. In case 1, the interface width should not change with refinement, so the simulated problem remains fixed at all N. We plot the change in our measured parameters over time for all refinements in Figure 3.13. We see in this figure that the parameters quickly converge to $N = 256$ values. Figure 3.14 demonstrates the differences between the 6 cases at the highest level of refinement with $N = 256$. Our results for this test match the results shown in [47] and [33].

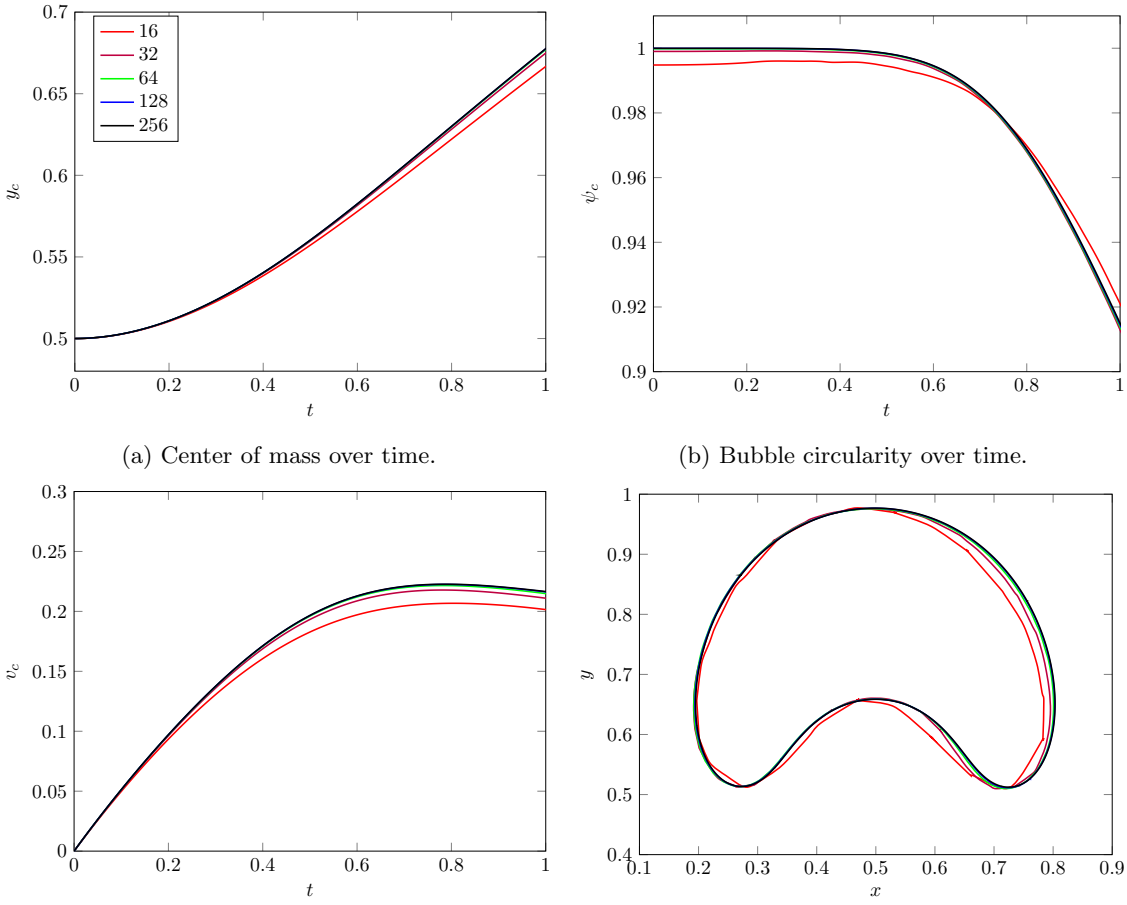

(a) Center of mass over time.

(b) Bubble circularity over time.

(c) Center of mass velocity over time.

(d) Bubble surface at $t = 1$.

Figure 3.13: Results for rising air bubble case 1.

3.4.7 Rayleigh-Taylor instability

The Rayleigh-Taylor instability experiment from [70] is a classic multi-phase fluid simulation. As in [47] and [33], we reproduce this experiment with our scheme and measure key features over time.

The initial state positions a denser fluid with $\rho_1 = 3$ over a lighter fluid with $\rho_0 = 1$ in a $[0, 1] \times [0, 4]$ domain discretized with cell size $\Delta x = 1/128$. The domain is periodic in the x-axis and has free-slip boundary conditions at the top and bottom walls. The interface

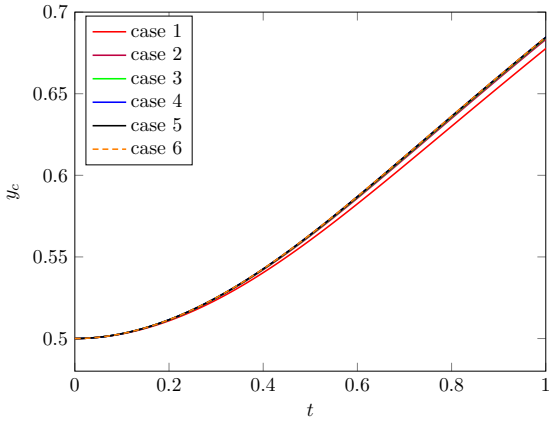

(a) Center of mass over time.

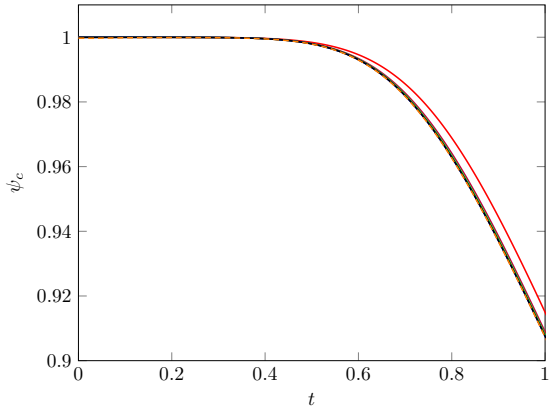

(b) Bubble circularity over time.

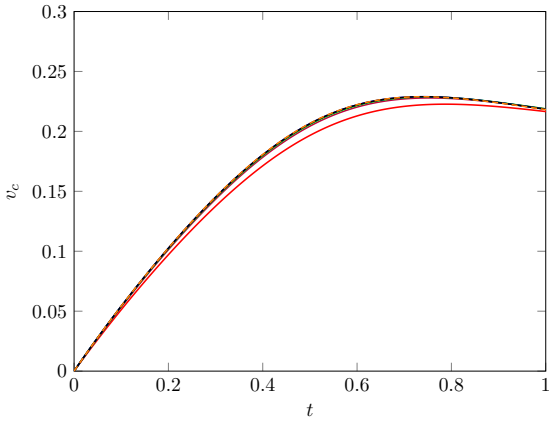

(c) Center of mass velocity over time.

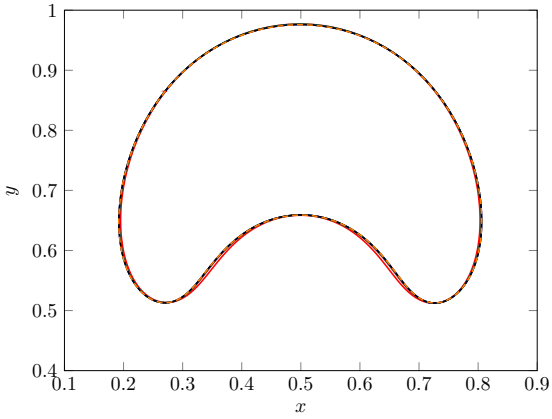

(d) Bubble surface at $t = 1$.

Figure 3.14: Comparing results for all rising bubble test cases with $N = 256$.

between the fluids is set to an unstable pertubation at $y = 2 + 0.1\cos(2\pi x)$, which will allow immediate mixing. The only external force applied is a gravity of $\langle 0, -1 \rangle$, and the fluids begin at rest. The characteristic parameter $A_t = (\rho_1 - \rho_0)/(\rho_1 + \rho_0)$, the "Atwood ratio", is used to scale the time step of $\Delta t = 5 \times 10^{-4}/\sqrt{A_t}$ and we run the simulation until $t\sqrt{A_t} = 8$. Both fluids have matched viscosity $\mu_0 = \mu_1 = 0.001$, and we set the surface tension constant $\sigma = 10^{-12}$ and the Cahn-Hilliard parameters as $\eta = 0.01$ and $\lambda M = 10^{-15}$

We show snapshots of this test in Figure 3.15 from $t\sqrt{A_t} = 0$ to $t\sqrt{A_t} = 2.5$ for our scheme and provide a comparison with our implementation of [33]. Figure 3.16 shows

the continuation of the test using our scheme from $t\sqrt{A_t} = 2.25$ to $t\sqrt{A_t} = 8$. Our results are visually comparable to the snapshots shown in [47] and [33], and maintain symmetry in the interface through the entire simulation. We also measure the location of the interface between the fluids from $t\sqrt{A_t} = 0$ to $t\sqrt{A_t} = 2.5$, plotting the highest and lowest point of the interface in Figure 3.18. Our results are similar to those of the experiments with similar parameters reported in [33], [47], [21] and [35]. As in these other works, the simulation does not reach a stable state in the time given.

As in [47] and [33], in Figure 3.17 we show a comparison of our scheme with different density values for fluid 1. We test densities $\rho_1 = 3, 30, 1000, 3000$, and our results for $t\sqrt{A_t} = 0$ to $t\sqrt{A_t} = 1.75$ are similar to those shown in previous works. However, we note that our interface does not maintain symmetry past $t\sqrt{A_t} = 4$ for the larger density ratios at the given parameters. [47] and [33] do not report past $t\sqrt{A_t} = 2$, so we cannot say whether this is a limitation of this approach or just our scheme.

3.4.8 Dam break

We simulate a dam break scenario as described in Martin and Moyce [65], where a rectangular volume of water at rest is released to flow in a larger container. This simulation shows how our scheme handles setups based on physical phenonmenon. The initial square of water with side length $a = 0.05715$ is positioned in the lower-left corner of the $[0, 4a] \times [0, 2a]$ domain. All walls in this domain are treated with the no-slip boundary condition, and each cell has size $\Delta x = a/64$. The initial velocity is zero everywhere in the domain. In

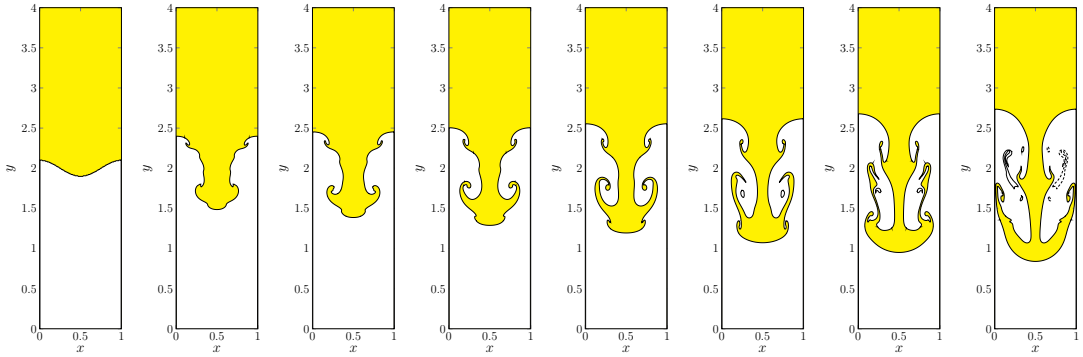

(a) Snapshots of a Rayleigh-Taylor simulation using Goulding et al. [33]'s method.

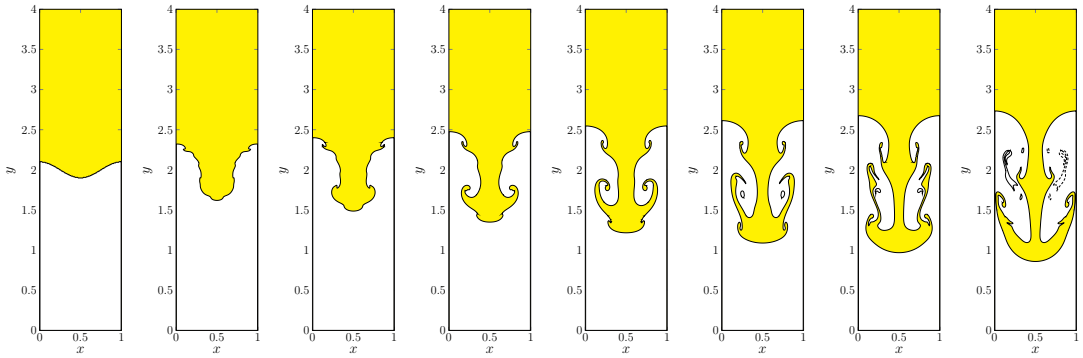

(b) Snapshots of a Rayleigh-Taylor simulation using our method.

Figure 3.15: Visual comparison of Rayleigh-Taylor simulations using different methods at $t = 0, 1, 1.25, 1.5, 1.75, 2, 2.25, 2.5$.

our simulation, fluid 1 represents water with viscosity $\mu_1 = 1.002 \times 10^{-3}$ and density $\rho_1 = 998.207$. Fluid 2 represents air and has viscosity constant $\mu_0 = 1.78 \times 10^{-5}$ and density $\rho_0 = 1.204$. The surface tension constant is $\sigma = 7.28 \times 10^{-2}$ and gravity of $\langle 0, -9.8 \rangle$ is used as an external force. We set the Cahn-Hilliard parameters based on [47] and [33], which are $M\lambda = 10^{-7}$ and $\eta = 0.01a$. We take time steps of $\Delta t = 7.1437 \times 10^{-5}$ and run the simulation until $t = 10$.

As illustrated in Figures 3.20 and 3.21, when the simulation begins gravity causes the water to flow from the left edge to the right edge of the domain. The water's momentum causes it to rise up the right wall of the domain, where gravity overcomes the momentum

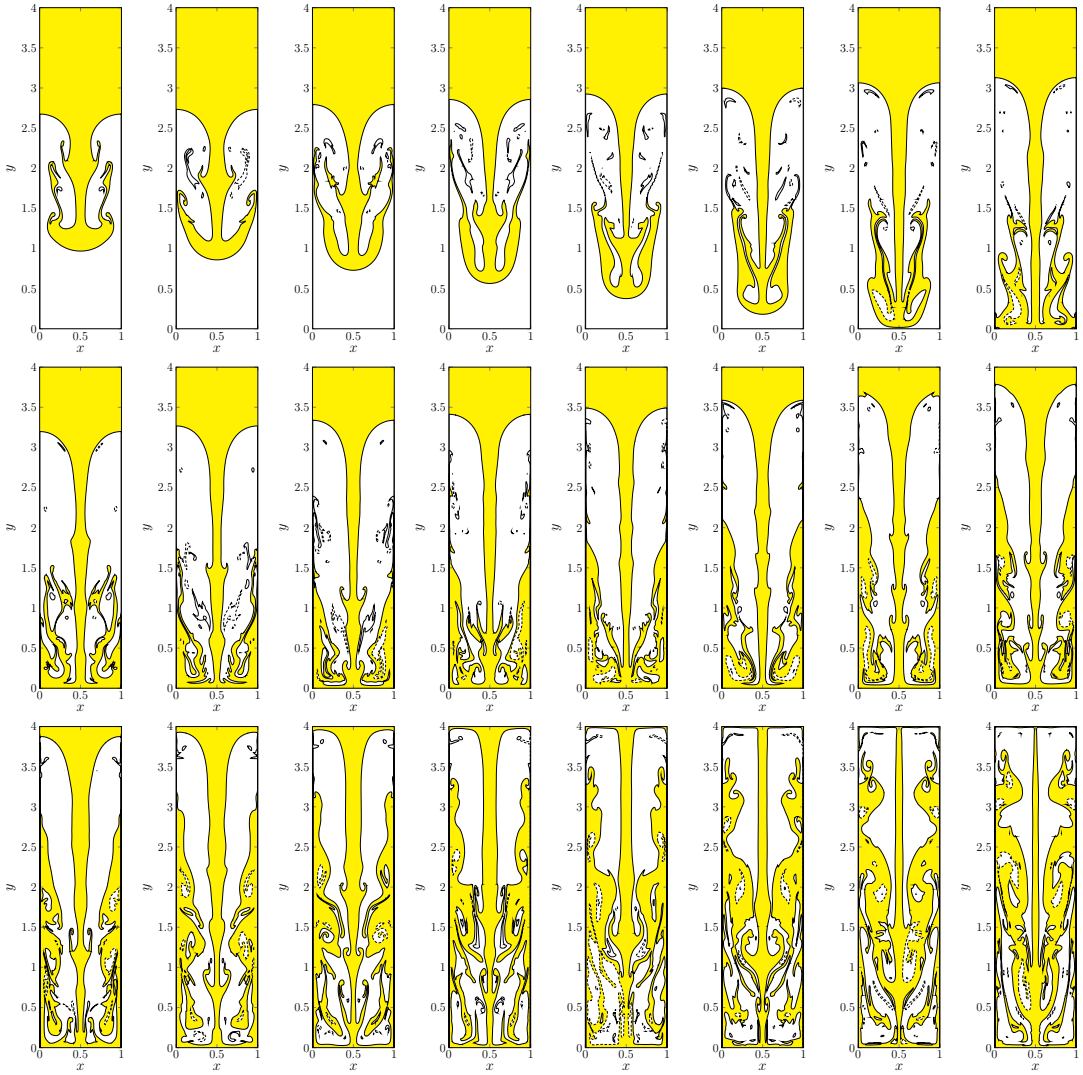

Figure 3.16: Continued snapshots of a Rayleigh-Taylor simulation using our method with $\rho_0 = 3$, from $t = 2.25$ to $t = 8$ in 0.25 increments.

and the water collapses back down on itself. Following [47] and [33], when reporting our results we non-dimensionalize t as $T = t\sqrt{\frac{|g_y|}{a}}$ and length by dividing by a. Figure 3.19 shows the location of the front of the water Z and the highest point H from $T = 0$ to

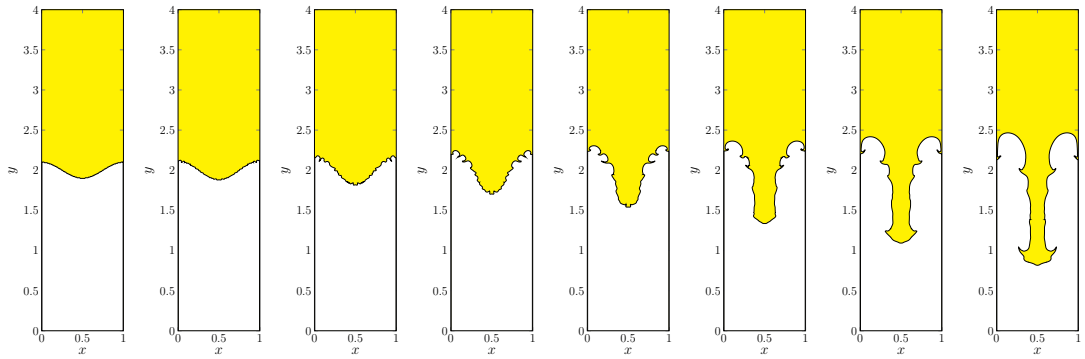

(a) $\rho_1 = 30$

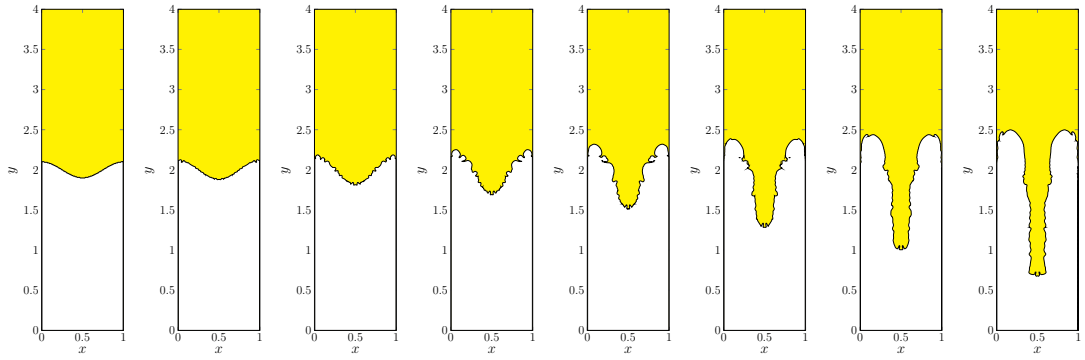

(b) $\rho_1 = 1000$

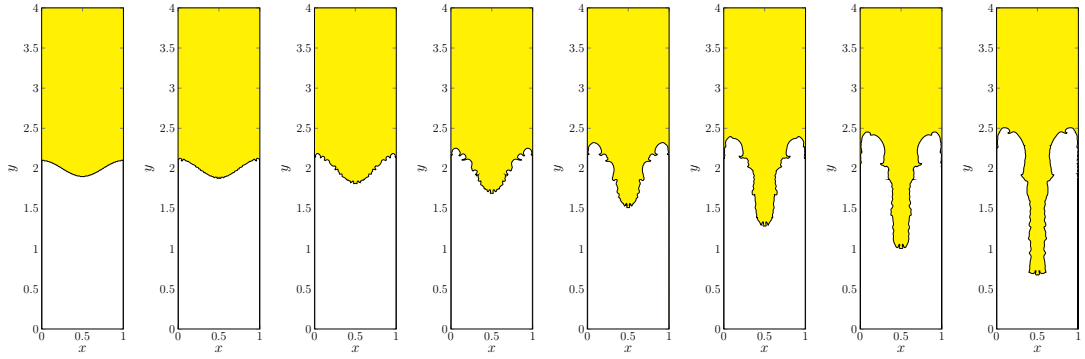

(c) $\rho_1 = 3000$

Figure 3.17: Snapshots of Rayleigh-Taylor simulations with different density ratios at $t = 0, 0.25, 0.5, 0.75, 1, 1.25, 1.5, 1.75$.

$T = 2.25$. These results compare well to the canonical experiment results in Martin and Moyce [65] and the results reported in [47] and [33].

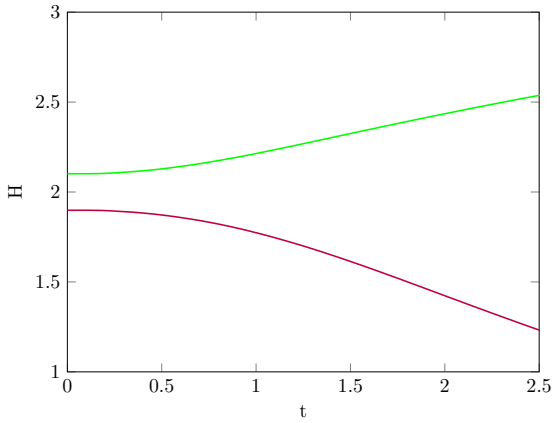

Figure 3.18: Tracking the maximum and minimum y of the phase interface in the Rayleigh-Taylor simulation with $\rho_1/\rho_0 = 3$.

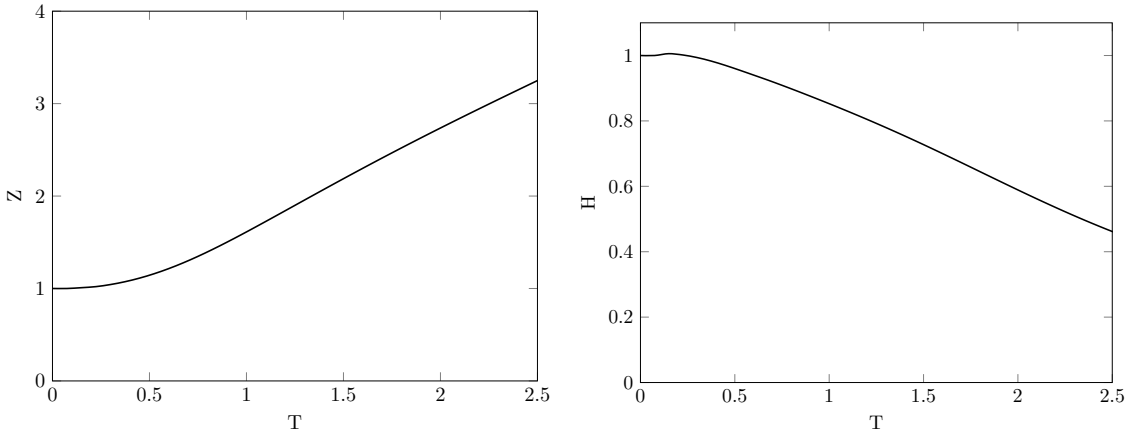

(a) The largest x location of fluid phase 1 over time. (b) The largest y location of fluid phase 1 over time.

Figure 3.19: Tracking the height and front of fluid phase 1 in the dam break scenario.

3.5 Conclusion

In this chapter we constructed a novel discretization of the Cahn-Hilliard equations that is able to guarantee that phase fractions remain bounded between 0 and 1. Maintaining phase fractions in the feasible range is essential for stability, since values outside this range may produce negative densities, especially with large density ratios. The method eliminates the need to perform a global post-processing step to correct the phase fraction.

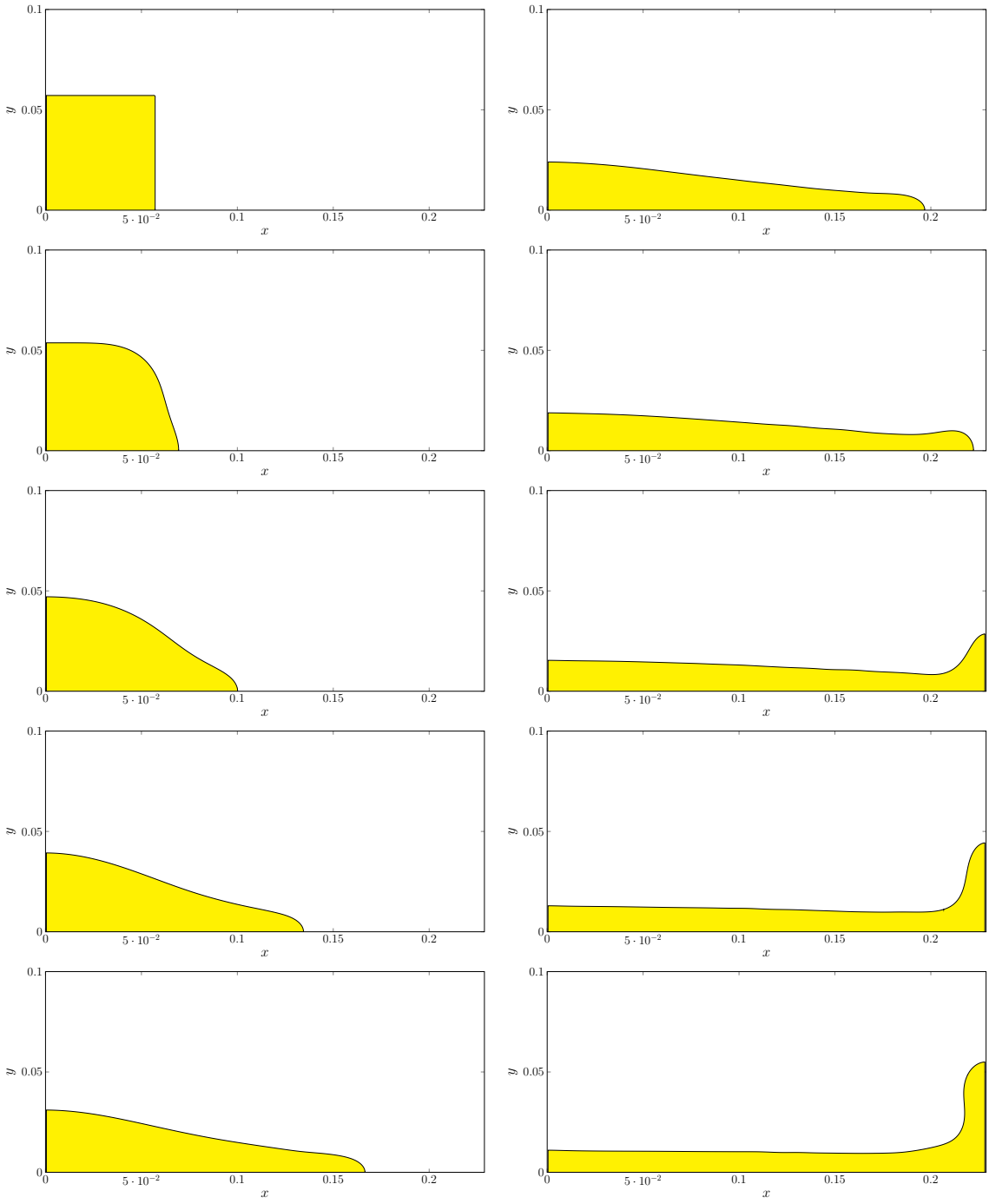

(a) $T = 0$ to $T = 2$ (b) $T = 2.5$ to $T = 4.5$

Figure 3.20: Snapshots of the dam break scenario from $T = 0$ to $T = 4.5$.

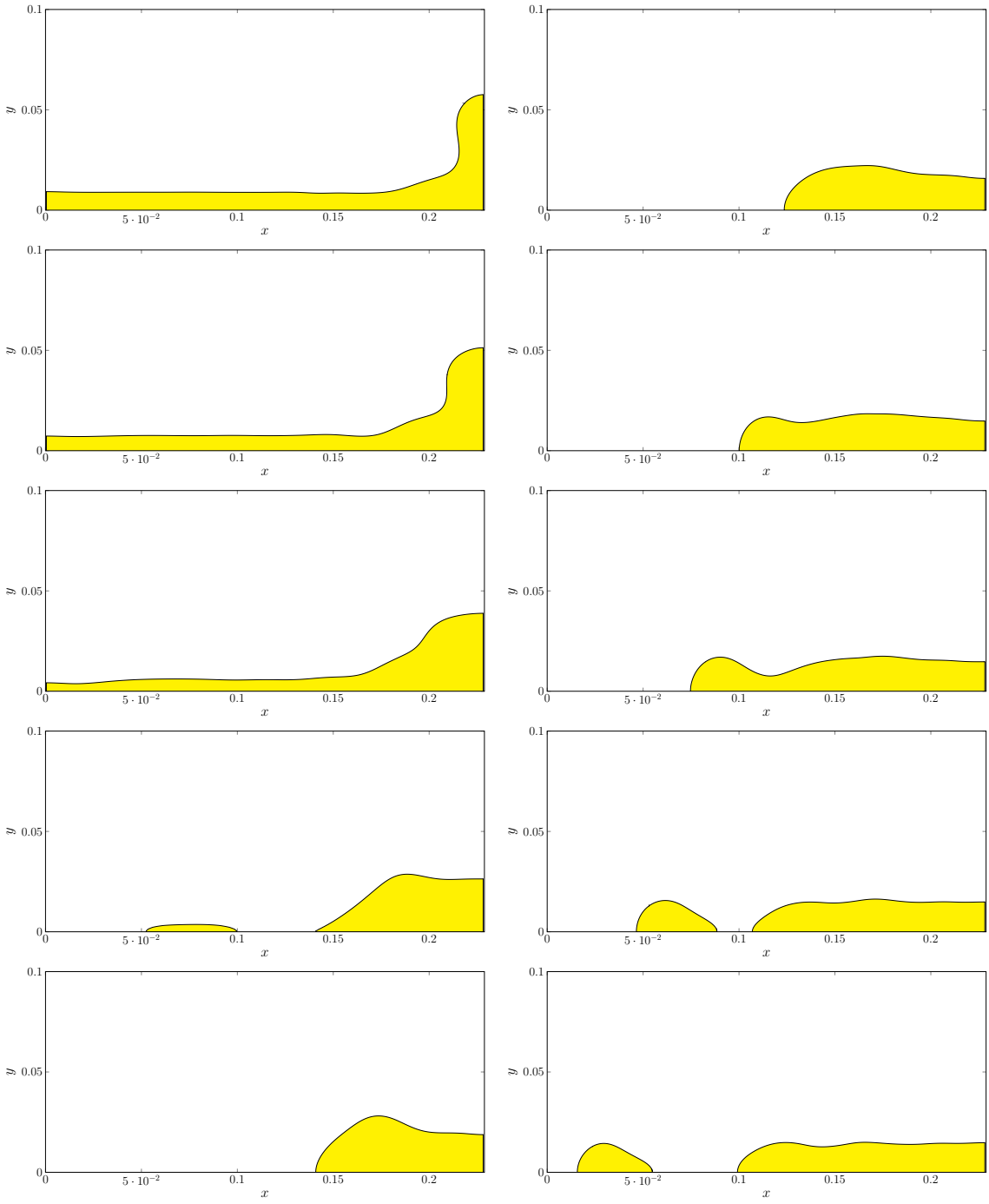

(a) $T = 5$ to $T = 7$ (b) $T = 7.5$ to $T = 9.5$

Figure 3.21: Snapshots of the dam break scenario from $T = 5$ to $T = 9.5$.

We constructed a formally 1.5 order accurate time integration scheme that uses a barrier potential to maintain bounds on the phase fraction. We present a potential function that allows the barrier formulation to be cast as a convex nonlinear optimization problem, which can be solved efficiently and robustly. We coupled our Cahn-Hilliard solver to the Navier-Stokes equations to simulate phase separation in a two-phase fluid flow in two dimensions. The resulting solver is mass-momentum consistent and works with large density ratios. We demonstrate second order accurate in γ and velocity and compare it with published results on a number of tests.

Since our method uses the same Navier-Stokes discretization and coupling as [33], we observe some of the same limitations, such as artifacts in the shearing test in Section 3.4.4. The method is sensitive to the sharpness of the interface, likely related to the lack of C^3 continuity in the potential F; unfortunately, the current formulation does not quite provide enough freedom to allow F to be C^3 everywhere. We have also observed that under some circumstances, the scheme suffers numerical difficulties or is not stable; this can occur when the parameters r or b are very small.

3.6 Acknowledgements

The work in this chapter was supported in part by National Science Foundation award NSF-2006570 as well as University of California award M23PL6076.

Chapter 4

Conclusions

In this work, we constructed two novel methods for the discretization of the coupled Cahn-Hilliard-Navier-Stokes equations in two dimensions.

The first method (Chapter 2) is a simple, conservative, and stable discretization of the Cahn-Hilliard equation. It is coupled to the Navier-Stokes equations to simulate two-phase fluid separation and flow. The scheme is consistent in mass and momentum and works well with large density ratios. This scheme is demonstrated to be second order accurate in the phase-field term γ, velocity, and pressure. We have compared it to published results from previous works in a variety of experiements.

In Chapter 2 we also introduce a novel discretization of a phase-field-based surface tension force that has finite effect around the phase interface and has a parameter that can be used to smoothly transition the force from a smoothed continuum surface force to a sharp interface force. In the latter case, it is shown that the applied surface tension is equivalent to using pressure jump conditions for a sharp interface method. This method

compares well against surface tension methods used in other Cahn-Hilliard-Navier-Stokes works.

This method has some limitations. Evolution of the phase-field term γ does not always maintain values in the range $[0, 1]$, which can lead to negative effective density values with large density ratios. While this bounds-violation is corrected using a post-processing redistribution scheme, the redistribution is global and not ideal. Our implementation also requires an additional Poisson solve to find the effective phase-field flux that does not always converge well. This limitiation is addressed in the second method in Chapter 3.

The second method (Chapter 3) is a second novel discretization of the Cahn-Hilliard equations that seeks to address one of the limitations of the first method. This discretization is able to guarantee that the phase-field concentration fraction term γ remains in the physically appropriate range $[0, 1]$. This guarantee eliminates the need for a separate post-processing step for γ. This discretization uses a potential function F with a barrier at 0 and 1 to maintain bounds on γ. We formulate this scheme as a convex nonlinear optimization problem. Like the first scheme, this method is also mass-momentum consistent and is formally 1.5 order accurate and observably second-order accurate in γ, velocity, and pressure.

However, there are some limitations to this second method. The piecewise potential function F from Chapter 3's method is not C^3 continuous at $\gamma = 0.5$, which may be the reason that the method shows some sensitivity to the interface width. This may be an area suited to further research. In some experiments we observed that there may be instability or numerical difficulties when the parameters r and b are particularly small. The inability

to support sufficiently small values for r may make this method not ideal for exceptionally large density ratios (such as those in excess of 10^6).

Both methods use the same Navier-Stokes discretization and are coupled to the Cahn-Hilliard equation in the same way. Therefore, they share some limitations of the momentum advection scheme. In both methods, we note that shearing flows with sharp phase-field transitions can lead to artifacts in the phase-field. These artifacts are observed to decrease under refinement. The method used for momentum advection, while consistent with the phase-field evolution, appears less robust than a classical WENO advection scheme.

Bibliography

[1] Helmut Abels and Mathias Wilke. Convergence to equilibrium for the cahn–hilliard equation with a logarithmic free energy. *Nonlinear Analysis: Theory, Methods & Applications*, 67(11):3176–3193, 2007.

[2] Rüyam Acar. Simulation of interface dynamics: a diffuse-interface model. *The Visual Computer*, 25(2):101–115, 2009.

[3] Daniel Acosta-Soba, Francisco Guillén-González, and J Rafael Rodriguez-Galván. An upwind dg scheme preserving the maximum principle for the convective cahn-hilliard model. *Numerical Algorithms*, 92(3):1589–1619, 2023.

[4] VE Badalassi and S Banerjee. Nano-structure computation with coupled momentum phase ordering kinetics models. *Nuclear engineering and design*, 235(10-12):1107–1115, 2005.

[5] Vittorio E Badalassi, Hector D Ceniceros, and Sanjoy Banerjee. Computation of multiphase systems with phase field models. *Journal of computational physics*, 190(2): 371–397, 2003.

[6] Rafael Bailo, José A Carrillo, Serafim Kalliadasis, and Sergio P Perez. Unconditional bound-preserving and energy-dissipating finite-volume schemes for the cahn-hilliard equation. *arXiv preprint arXiv:2105.05351*, 2021.

[7] John W Barrett and James F Blowey. An error bound for the finite element approximation of the cahn-hilliard equation with logarithmic free energy. *Numerische Mathematik*, 72:1–20, 1995.

[8] John W Barrett, James F Blowey, and Harald Garcke. Finite element approximation of the cahn–hilliard equation with degenerate mobility. *SIAM Journal on Numerical Analysis*, 37(1):286–318, 1999.

[9] James F Blowey and Charles M Elliott. The cahn–hilliard gradient theory for phase separation with non-smooth free energy part i: Mathematical analysis. *European Journal of Applied Mathematics*, 2(3):233–280, 1991.

[10] James F Blowey, MIM Copetti, and Charles M Elliott. Numerical analysis of a model for phase separation of a multicomponent alloy. *IMA Journal of Numerical Analysis*, 16(1):111–139, 1996.

[11] Jeremiah U Brackbill, Douglas B Kothe, and Charles Zemach. A continuum method for modeling surface tension. *Journal of computational physics*, 100(2):335–354, 1992.

[12] Markus Bussmann, Douglas B Kothe, and James M Sicilian. Modeling high density ratio incompressible interfacial flows. In *Fluids Engineering Division Summer Meeting*, volume 36150, pages 707–713, 2002.

[13] John W. Cahn and John E. Hilliard. Free energy of a nonuniform system. i. interfacial free energy. *The Journal of Chemical Physics*, 28(2):258–267, 1958. doi: 10.1063/1.1744102. URL https://doi.org/10.1063/1.1744102.

[14] Wenbin Chen, Cheng Wang, Xiaoming Wang, and Steven M Wise. Positivity-preserving, energy stable numerical schemes for the cahn-hilliard equation with logarithmic potential. *Journal of Computational Physics: X*, 3:100031, 2019.

[15] Kelong Cheng, Wenqiang Feng, Cheng Wang, and Steven M Wise. An energy stable fourth order finite difference scheme for the cahn–hilliard equation. *Journal of Computational and Applied Mathematics*, 362:574–595, 2019.

[16] Pao-Hsiung Chiu and Yan-Ting Lin. A conservative phase field method for solving incompressible two-phase flows. *Journal of Computational Physics*, 230(1):185–204, 2011.

[17] Alexandre Joel Chorin. Numerical solution of the navier-stokes equations. *Mathematics of computation*, 22(104):745–762, 1968.

[18] Maria Inês Martins Copetti and Charles M Elliott. Numerical analysis of the cahn-hilliard equation with a logarithmic free energy. *Numerische Mathematik*, 63:39–65, 1992.

[19] Bart J. Daly. Numerical Study of Two Fluid Rayleigh-Taylor Instability. *The Physics of Fluids*, 10(2):297–307, 02 1967. ISSN 0031-9171. doi: 10.1063/1.1762109. URL https://doi.org/10.1063/1.1762109.

[20] Arnaud Debussche and Lucia Dettori. On the cahn-hilliard equation with a logarithmic free energy. *Nonlinear Analysis: Theory, Methods & Applications*, 24(10):1491–1514, 1995.

[21] Hang Ding, Peter D.M. Spelt, and Chang Shu. Diffuse interface model for incompressible two-phase flows with large density ratios. *Journal of Computational Physics*, 226(2):2078–2095, 2007. ISSN 0021-9991. doi: https://doi.org/10.1016/j.jcp.2007.06.028. URL https://www.sciencedirect.com/science/article/pii/S0021999107002793.

[22] Lixiu Dong, Cheng Wang, Hui Zhang, and Zhengru Zhang. A positivity-preserving, energy stable and convergent numerical scheme for the cahn–hilliard equation with a flory–huggins–degennes energy. *Communications in Mathematical Sciences*, 17(4): 921–939, 2019.

[23] Suchuan Dong and Jie Shen. A time-stepping scheme involving constant coefficient matrices for phase-field simulations of two-phase incompressible flows with large density ratios. *Journal of Computational Physics*, 231(17):5788–5804, 2012.

[24] Suchuan Dong and Jie Shen. A time-stepping scheme involving constant coefficient matrices for phase-field simulations of two-phase incompressible flows with large density ratios. *Journal of Computational Physics*, 231(17):5788–5804, 2012.

[25] Charles M Elliott. The cahn-hilliard model for the kinetics of phase separation. In *Mathematical models for phase change problems*, pages 35–73. Springer, 1989.

[26] Charles M Elliott and Donald A French. A nonconforming finite-element method for the two-dimensional cahn–hilliard equation. *SIAM Journal on Numerical Analysis*, 26 (4):884–903, 1989.

[27] Charles M Elliott and Harald Garcke. On the cahn–hilliard equation with degenerate mobility. *Siam journal on mathematical analysis*, 27(2):404–423, 1996.

[28] David J Eyre. Unconditionally gradient stable time marching the cahn-hilliard equation. *MRS online proceedings library (OPL)*, 529:39, 1998.

[29] Xiaobing Feng and Andreas Prohl. Error analysis of a mixed finite element method for the cahn-hilliard equation. *Numerische Mathematik*, 99:47–84, 2004.

[30] Marianne M. Francois, Sharen J. Cummins, Edward D. Dendy, Douglas B. Kothe, James M. Sicilian, and Matthew W. Williams. A balanced-force algorithm for continuous and sharp interfacial surface tension models within a volume tracking framework. *Journal of Computational Physics*, 213(1):141–173, March 2006. ISSN 00219991. doi: 10.1016/j.jcp.2005.08.004. URL `https://linkinghub.elsevier.com/retrieve/pii/S0021999105003748`.

[31] Florian Frank, Andreas Rupp, and Dmitri Kuzmin. Bound-preserving flux limiting schemes for dg discretizations of conservation laws with applications to the cahn–hilliard equation. *Computer Methods in Applied Mechanics and Engineering*, 359: 112665, 2020.

[32] Daisuke Furihata. A stable and conservative finite difference scheme for the cahn-hilliard equation. *Numerische Mathematik*, 87(4):675–699, 2001.

[33] Jason Goulding, Mehrnaz Ayazi, Tamar Shinar, and Craig Schroeder. Simplified conservative discretization of the cahn-hilliard-navier-stokes equations. *Journal of Computational Physics*, ?:?, ? ISSN ? doi: ? URL ?

[34] László Gránásy and David W Oxtoby. Cahn–hilliard theory with triple-parabolic free energy. i. nucleation and growth of a stable crystalline phase. *The Journal of Chemical Physics*, 112(5):2399–2409, 2000.

[35] J.-L. Guermond and L. Quartapelle. A projection fem for variable density incompressible flows. *Journal of Computational Physics*, 165(1):167–188, 2000. ISSN 0021-9991. doi: https://doi.org/10.1006/jcph.2000.6609. URL `https://www.sciencedirect.com/science/article/pii/S0021999100966099`.

[36] Francisco Guillén-González and Giordano Tierra. On linear schemes for a cahn–hilliard diffuse interface model. *Journal of Computational Physics*, 234:140–171, 2013.

[37] Francisco Guillén-González and Giordano Tierra. Second order schemes and time-step adaptivity for allen–cahn and cahn–hilliard models. *Computers & Mathematics with Applications*, 68(8):821–846, 2014.

[38] Zhenlin Guo, Ping Lin, J Lowengrub, and Steven M Wise. Mass conservative and energy stable finite difference methods for the quasi-incompressible navier–stokes–cahn–hilliard system: Primitive variable and projection-type schemes. *Computer Methods in Applied Mechanics and Engineering*, 326:144–174, 2017.

[39] Morton E Gurtin, Debra Polignone, and Jorge Vinals. Two-phase binary fluids and immiscible fluids described by an order parameter. *Mathematical Models and Methods in Applied Sciences*, 6(06):815–831, 1996.

[40] F. Harlow and E. Welch. Numerical calculation of time dependent viscous flow of fluid with a free surface. *Phys Fluid*, 8(12):2182–2189, 1965.

[41] Qiaolin He, Roland Glowinski, and Xiao-Ping Wang. A least-squares/finite element method for the numerical solution of the navier–stokes-cahn–hilliard system modeling the motion of the contact line. *Journal of computational physics*, 230(12):4991–5009, 2011.

[42] Qunwu He and Nobuhide Kasagi. Phase-field simulation of small capillary-number two-phase flow in a microtube. *Fluid dynamics research*, 40(7-8):497, 2008.

[43] Yinnian He, Yunxian Liu, and Tao Tang. On large time-stepping methods for the cahn–hilliard equation. *Applied Numerical Mathematics*, 57(5-7):616–628, 2007.

[44] Pierre C Hohenberg and Bertrand I Halperin. Theory of dynamic critical phenomena. *Reviews of Modern Physics*, 49(3):435, 1977.

[45] Qiong-Ao Huang, Wei Jiang, Jerry Zhijian Yang, and Cheng Yuan. A structure-preserving, upwind-sav scheme for the degenerate cahn–hilliard equation with applications to simulating surface diffusion. *Journal of Scientific Computing*, 97(3):64, 2023.

[46] Ziyang Huang, Guang Lin, and Arezoo M Ardekani. Consistent and conservative scheme for incompressible two-phase flows using the conservative allen-cahn model. *Journal of Computational Physics*, 420:109718, 2020.

[47] Ziyang Huang, Guang Lin, and Arezoo M. Ardekani. Consistent, essentially conservative and balanced-force phase-field method to model incompressible two-phase flows. *Journal of Computational Physics*, 406:109192,

2020. ISSN 0021-9991. doi: https://doi.org/10.1016/j.jcp.2019.109192. URL https://www.sciencedirect.com/science/article/pii/S0021999119308976.

[48] Ziyang Huang, Guang Lin, and Arezoo M Ardekani. A consistent and conservative volume distribution algorithm and its applications to multiphase flows using phase-field models. *International Journal of Multiphase Flow*, 142:103727, 2021.

[49] David Jacqmin. Calculation of two-phase navier–stokes flows using phase-field modeling. *Journal of Computational Physics*, 155(1):96–127, 1999. ISSN 0021-9991. doi: https://doi.org/10.1006/jcph.1999.6332. URL https://www.sciencedirect.com/science/article/pii/S0021999199963325.

[50] Guang-Shan Jiang and Chi-Wang Shu. Efficient implementation of weighted eno schemes. *Journal of computational physics*, 126(1):202–228, 1996.

[51] Myungjoo Kang, Ronald P Fedkiw, and Xu-Dong Liu. A boundary condition capturing method for multiphase incompressible flow. *Journal of scientific computing*, 15:323–360, 2000.

[52] Junseok Kim. A continuous surface tension force formulation for diffuse-interface models. *Journal of computational physics*, 204(2):784–804, 2005.

[53] Junseok Kim. Phase field computations for ternary fluid flows. *Computer methods in applied mechanics and engineering*, 196(45-48):4779–4788, 2007.

[54] Junseok Kim. A generalized continuous surface tension force formulation for phase-field models for multi-component immiscible fluid flows. *Computer Methods in Applied Mechanics and Engineering*, 198(37-40):3105–3112, 2009.

[55] Junseok Kim. Phase-field models for multi-component fluid flows. *Communications in Computational Physics*, 12(3):613–661, 2012.

[56] Junseok Kim and John Lowengrub. Phase field modeling and simulation of three-phase flows. *Interfaces and free boundaries*, 7(4):435–466, 2005.

[57] Benjamin Lalanne, Lucia Rueda Villegas, Sébastien Tanguy, and Frédéric Risso. On the computation of viscous terms for incompressible two-phase flows with level set/ghost fluid method. *Journal of Computational Physics*, 301:289–307, 2015.

[58] Dongsun Lee, Joo-Youl Huh, Darae Jeong, Jaemin Shin, Ana Yun, and Junseok Kim. Physical, mathematical, and numerical derivations of the cahn–hilliard equation. *Computational Materials Science*, 81:216–225, 2014.

[59] Xiao Li, ZhongHua Qiao, and Hui Zhang. An unconditionally energy stable finite difference scheme for a stochastic cahn-hilliard equation. *Science China Mathematics*, 59:1815–1834, 2016.

[60] Yibao Li, Hyun Geun Lee, Binhu Xia, and Junseok Kim. A compact fourth-order finite difference scheme for the three-dimensional cahn–hilliard equation. *Computer Physics Communications*, 200:108–116, 2016.

[61] Yibao Li, Yongho Choi, and Junseok Kim. Computationally efficient adaptive time step method for the cahn–hilliard equation. *Computers & Mathematics with Applications*, 73(8):1855–1864, 2017.

[62] Chen Liu, Deep Ray, Christopher Thiele, Lu Lin, and Beatrice Riviere. A pressure-correction and bound-preserving discretization of the phase-field method for variable density two-phase flows. *Journal of Computational Physics*, 449:110769, 2022.

[63] Chun Liu and Jie Shen. A phase field model for the mixture of two incompressible fluids and its approximation by a fourier-spectral method. *Physica D: Nonlinear Phenomena*, 179(3-4):211–228, 2003.

[64] Haihu Liu and Yonghao Zhang. Phase-field modeling droplet dynamics with soluble surfactants. *Journal of Computational Physics*, 229(24):9166–9187, 2010.

[65] JC Martin and WJ Moyce. An experimental study of the collapse of fluid columns on a rigid horizontal plane, in a medium of lower, but comparable, density. 5. *Philosophical Transactions of the Royal Society of London Series A-Mathematical and Physical Sciences*, 244(882):325–334, 1952.

[66] Alain Miranville and Sergey Zelik. Robust exponential attractors for cahn-hilliard type equations with singular potentials. *Mathematical methods in the applied sciences*, 27 (5):545–582, 2004.

[67] Shahab Mirjalili, Christopher B Ivey, and Ali Mani. A conservative diffuse interface method for two-phase flows with provable boundedness properties. *Journal of Computational Physics*, 401:109006, 2020.

[68] Mark Owkes and Olivier Desjardins. A mass and momentum conserving unsplit semi-lagrangian framework for simulating multiphase flows. *Journal of Computational Physics*, 332:21–46, 2017.

[69] Mehdi Raessi and Heinz Pitsch. Consistent mass and momentum transport for simulating incompressible interfacial flows with large density ratios using the level set method. *Computers & Fluids*, 63:70–81, 2012.

[70] Rayleigh. Investigation of the Character of the Equilibrium of an Incompressible Heavy Fluid of Variable Density*. *Proceedings of the London Mathematical Society*, s1-14(1):170–177, 11 1882. ISSN 0024-6115. doi: 10.1112/plms/s1-14.1.170. URL `https://doi.org/10.1112/plms/s1-14.1.170`.

[71] Somnath Santra, Shubhadeep Mandal, and Suman Chakraborty. Phase-field modeling of multicomponent and multiphase flows in microfluidic systems: A review. *International Journal of Numerical Methods for Heat & Fluid Flow*, 31(10):3089–3131, 2020.

[72] Jie Shen and Xiaofeng Yang. Energy stable schemes for cahn-hilliard phase-field model of two-phase incompressible flows. *Chinese Annals of Mathematics, Series B*, 31(5): 743–758, 2010.

[73] Jie Shen and Xiaofeng Yang. Numerical approximations of allen-cahn and cahn-hilliard equations. *Discrete Contin. Dyn. Syst*, 28(4):1669–1691, 2010.

[74] Jie Shen and Xiaofeng Yang. A phase-field model and its numerical approximation for two-phase incompressible flows with different densities and viscosities. *SIAM Journal on Scientific Computing*, 32(3):1159–1179, 2010.

[75] Jie Shen and Xiaofeng Yang. Decoupled, energy stable schemes for phase-field models of two-phase incompressible flows. *SIAM Journal on Numerical Analysis*, 53(1):279–296, 2015.

[76] Knut Erik Teigen, Peng Song, John Lowengrub, and Axel Voigt. A diffuse-interface method for two-phase flows with soluble surfactants. *Journal of computational physics*, 230(2):375–393, 2011.

[77] Grétar Tryggvason. Numerical simulations of the rayleigh-taylor instability. *Journal of Computational Physics*, 75(2):253–282, 1988. ISSN 0021-9991. doi: https://doi.org/10.1016/0021-9991(88)90112-X. URL `https://www.sciencedirect.com/science/article/pii/002199918890112X`.

[78] Bao-Shan Wang, Peng Li, Zhen Gao, and Wai Sun Don. An improved fifth order alternative weno-z finite difference scheme for hyperbolic conservation laws. *Journal of Computational Physics*, 374:469–477, 2018.

[79] Garth N Wells, Ellen Kuhl, and Krishna Garikipati. A discontinuous galerkin method for the cahn–hilliard equation. *Journal of Computational Physics*, 218(2):860–877, 2006.

[80] Steven M Wise, John S Lowengrub, Hermann B Frieboes, and Vittorio Cristini. Three-dimensional multispecies nonlinear tumor growth—i: model and numerical method. *Journal of theoretical biology*, 253(3):524–543, 2008.

[81] Qing Xia, Junxiang Yang, and Yibao Li. On the conservative phase-field method with the n-component incompressible flows. *Physics of Fluids*, 35(1), 2023.

[82] Xiaofeng Yang and Jia Zhao. On linear and unconditionally energy stable algorithms for variable mobility cahn-hilliard type equation with logarithmic flory-huggins potential. *arXiv preprint arXiv:1701.07410*, 2017.

[83] Xiaofeng Yang, James J Feng, Chun Liu, and Jie Shen. Numerical simulations of jet pinching-off and drop formation using an energetic variational phase-field method. *Journal of Computational Physics*, 218(1):417–428, 2006.

[84] Pengtao Yue, James J Feng, Chun Liu, and Jie Shen. A diffuse-interface method for simulating two-phase flows of complex fluids. *Journal of Fluid Mechanics*, 515:293–317, 2004.

[85] Pengtao Yue, James J Feng, Chun Liu, and Jie Shen. Diffuse-interface simulations of drop coalescence and retraction in viscoelastic fluids. *Journal of Non-Newtonian Fluid Mechanics*, 129(3):163–176, 2005.

[86] Jun Zhang and Xiaofeng Yang. Non-iterative, unconditionally energy stable and large time-stepping method for the cahn-hilliard phase-field model with flory-huggins-de gennes free energy. *Advances in Computational Mathematics*, 46:1–27, 2020.

[87] Guangpu Zhu, Jisheng Kou, Shuyu Sun, Jun Yao, and Aifen Li. Numerical approximation of a phase-field surfactant model with fluid flow. *Journal of Scientific Computing*, 80:223–247, 2019.

[88] Jingzhi Zhu, Long-Qing Chen, Jie Shen, and Veena Tikare. Coarsening kinetics from a variable-mobility cahn-hilliard equation: Application of a semi-implicit fourier spectral method. *Physical Review E*, 60(4):3564, 1999.